Pushing the KIT 2 MW Coaxial-Cavity Short-Pulse Gyrotron Towards a DEMO Relevant Design

Zur Erlangung des akademischen Grades eines

DOKTORS DER INGENIEURWISSENSCHAFTEN (Dr.-Ing.)

von der KIT-Fakultät für Elektrotechnik und Informationstechnik des Karlsruher Instituts für Technologie (KIT)

genehmigte

DISSERTATION

von

M.Sc. Sebastian Ruess
geb. in Ulm

Tag der mündlichen Prüfung: 27.02.2020

Hauptreferent: Prof. Dr.-Ing. John Jelonnek
Korreferent: Prof. Dr. Minh-Quang Tran

Kurzfassung

Der globale Klimawandel und die daraus resultierende Erderwärmung zwingt zur Erschließung alternativer und klimaschonender Energiequellen. Eine umweltfreundliche und grundlastfähige Energieerzeugung soll in der Zukunft mit Fusionskraftwerken gelingen. Um die Umsetzbarkeit und Realisierung der Fusionstechnologie unter Beweis zu stellen, soll noch in der ersten Hälfte dieses Jahrhunderts ein DEMOnstrations-Fusionskraftwerk (DEMO) aufgebaut werden. Dieses Fusionskraftwerk soll eine elektrische Leistung von 500 MW generieren. Die nominelle thermische Leistung wird im Bereich 2-3 GW liegen. Um das Fusionsplasma auf die nominelle Plasmatemperatur zu erhitzen, ist eine Heizleistung von 150 MW notwendig. Die Elektron-Zyklotron-Resonanzheizung (ECRH) soll hierzu 50 MW beitragen und nimmt somit eine wichtige Schlüsselrolle ein. Die hierfür notwendige Millimeterwellen-Strahlung bei Frequenzen bis zu 240 GHz soll von Gyrotrons erzeugt werden. Das Karlsruher Institut für Technologie (KIT) entwickelte bereits erfolgreich Gyrotrons für die Fusionsexperimente Wendelstein 7-X (W7-X) und ITER mit geforderten Dauerstrichleistungen von 1 MW bei einer Betriebsfrequenz von 140 GHz und 170 GHz. Für DEMO werden demgegenüber Ausgangsleistungen im Multi-Megawatt Bereich gefordert. Experimente am KIT haben gezeigt, dass ein stabiler Betrieb im Multi-MW Leistungsbereich mit der koaxialen Gyrotrontechnologie erreicht wird. In der Vergangenheit wurde die koaxiale Gyrotrontechnologie jedoch lediglich bei kurzen Pulsen bis 4 ms getestet. Es ist zu zeigen, dass koaxiale Gyrotrons im Langpulsbetrieb mit Ausgangsleistungen im Multi-Megawattbereich betrieben werden können. Basierend auf dem bereits am KIT existierenden Kurzpuls-Gyrotron, wird in dieser Arbeit zum ersten Mal ein koaxiales Langpuls-Gyrotron entwickelt und gebaut, mit dem der thermisch und elektrisch eingeschwungene Zustand erreicht werden kann. Es wird angenommen, dass dieser eingeschwungene Zustand nach ca. 1s erreicht wird. Darum werden in dieser Arbeit die notwendigen Schlüsseltechnologien zur Kühlung von thermisch hochbelasteten Komponenten und die notwendige Verbindungstechnologie weiter entwickelt. Zudem werden

Vorschläge erarbeitet, um den Elektronenstrahlerzeuger für den Dauerstrichbetrieb zu optimieren.
Hierzu werden in der vorliegenden Arbeit zwei unterschiedliche Elektronenstrahlerzeuger-Konzepte verfolgt und hinsichtlich den DEMO relevanten Anforderungen optimiert. Im ersten Schritt wird die konventionelle Elektronenstrahlerzeuger-Technologie vorangetrieben. Zum ersten Mal wird ein bereits existierender Elektronenstrahlerzeuger mit Anti-Emissionsbeschichtung an den Emitterkanten getestet. Die Verwendung dieser Emitter-Tehnologie reduziert signifikant die Sensitivität bezüglich vorhandener Herstellungstoleranzen und thermischer Ausdehnung. Zudem wird die konventionelle Technologie numerisch optimiert und experimentell mit der Langpulsröhre getestet. Darüber hinaus, wird erstmalig gezeigt, dass dieser Elektronenstrahlerzeuger ebenfalls in einer DEMO relevanten Diodenkonfiguration die Designkriterien komplett erfüllt. Um die Betriebsfrequenz und Ausgangsleistung hinsichtlich eines DEMO relevanten Designs weiter zu erhöhen, ist ein neuer Elektronenstrahlerzeuger Ansatz notwendig. Die Hauptanforderungen an einen neuartigen Elektronenstrahlerzeuger sind: (i) Minimierung der Temperatur von thermisch belasteten Komponenten, um die thermische Ausdehnung während des nominellen Betriebs zu reduzieren und (ii) die Emitteroberfläche zu maximieren, um bei gegebenem Bohrlochdurchmesser des supraleitenden Magneten die Stromstärke und somit die Ausgangsleistung zu erhöhen. Diese Anforderungen können mit einem konventionellen Elektronenstrahlerzeuger nicht erfüllt werden, da das Design, bei gleichbleibenden Abmaßen, nicht die Möglichkeit eines größeren Emittereinbaus erlaubt. Durch die Verwendung eines inversen Elektronenstrahlerzeugers können diese Ziele jedoch erreicht werden. Hierbei wird die Kathode an der Außenseite positioniert was zu einer direkten und effizienten Kühlung führt. Des Weiteren werden Materialien mit hoher Wärmeleitfähigkeit verwendet, um die gespeicherte Wärmeenergie nach außen abzuleiten. Thermomechanische Simulationen zeigen, dass die maximale Temperatur durch diese Optimierungen signifikant reduziert wurde. Des Weiteren ermöglicht das inverse Design die Installation eines um 17 % größeren Emitters bei gleichbleibendem maximalen Durchmesser des Elektronenstrahlerzeugers. Aufgrund der größeren Emitteroberfläche kann ein größerer Strahlstrom emittiert und somit eine höhere Ausgangsleistung generiert werden.
Um in der Zukunft kostengünstige DEMO relevante Prototypen aufbauen zu können, wird ein weiterer Fokus auf kostenoptimierte Verbindungstechnologien gelegt. Intensive Untersuchungen zeigen, dass die Verwendung von Basis-Nickel Loten eine hervorragende Alternative zu den bereits bekannten

Gold und Silber Loten darstellt. Insbesondere die Auswertung von Schliffbildern hat ergeben, dass durch den optimierten Prozess die Toleranzen und die Leckraten verbessert wurden. Durch den optimierten Lötprozess ist es nun möglich, KIT-intern langpulsfähige Gyrotronkomponenten kostengünstig herzustellen.
Um die Pulslänge von 4 ms auf 150 ms zu erhöhen werden die modularen Komponenten des koaxialen Gyrotrons separat mit einer für KIT-Kurzpuls-Gyrotrons neuartigen Kühlmethode ausgestattet. Diese einzigartige Optimierung ermöglicht die Aufzeichnung der elektrischen Verluste jeder einzelnen Komponenten. Um jedoch das Ziel des Dauerstrichbetriebs zu ermöglichen wird ein optimiertes Minikanal-Kühlungsdesign für die Kavität entwickelt und an einem Modell experimentell getestet. Die maximale Temperatur im eingeschwungenen Zustand erreicht hierbei 210 °C. Um thermische Spannungen weiter zu reduzieren und die Lebensdauer eines Gyrotrons zu erhöhen, wird erstmalig die Verwendung einer Sprühkühlung in Gyrotrons untersucht. Experimentelle Tests und Auswertungen zeigen, dass die Wärmeleitfähigkeit der Sprühkühlung im Vergleich zur Minikanal-Kühlung um den Faktor 10 größer ist. Des Weiteren stellt die Sprühkühlung signifikante Vorteile in der Überwachung und Zuverlässigkeit sowie der mechanischen Implementierung dar.
Die erfolgreichen Tests des KIT-intern gefertigten koaxialen Gyrotrons bestätigen die Optimierungs- und Entwicklungsschritte der Schlüsselkomponenten erfolgreich. Hierbei wird eine maximale Ausgangsleistung von 2.2 MW bei einer Betriebsfrequenz von 169.89 GHz kalorimetrisch gemessen. Aufgrund des optimierten Herstellungsprozesses und der damit reduzierten Toleranzen, konnte im Vergleich zum Kurzpuls-Gyrotron die elektronische Effizienz um 4 % erhöht werden.

Abstract

Due to global climate change and the resulting global warming, there is a need to develop alternatives and climate-friendly energy sources. An environmentally friendly and base loadable energy production can be realized in the future with fusion power plants. In order to demonstrate the feasibility and implementation of fusion technology, a DEMOnstration fusion power plant (DEMO) should still be built in the first half of this century. This fusion power plant should generate an electrical power of 500 MW with an available thermal performance in the range of 2-3 GW. To heat the fusion plasma on the nominal plasma temperature, a heating power of 150 MW is required. The electron cyclotron resonance heating (ECRH) contributes 50 MW and plays an important key role. The necessary millimeter-wave radiation up to 240 GHz will be generated by gyrotrons. The Karlsruhe Institute of Technology (KIT) has already successfully developed gyrotrons for the fusion experiments Wendelstein 7-X (W7-X) and ITER with a continuous wave power of 1 MW at an operating frequency of 140 GHz and 170 GHz. In order to reduce the total number of gyrotrons required per plant and to enable cost-efficient operation, DEMO requires gyrotrons with an output power level in the multi-megawatt range. Short-pulse experiments have shown that a stable operation in the multi-MW power range can be achieved with the coaxial-cavity gyrotron technology. However, up to now, the coaxial gyrotron technology was tested up to a pulse length of 4 ms. Therefore, it has to be shown that coaxial gyrotrons can be operated in long-pulse mode with output powers in the multi-megawatt range. Based on the already existing short-pulse gyrotron, in this work, a long pulse gyrotron is developed and built for the first time, with which the thermally and electrically steady state operation can be achieved. It is assumed that this steady state is reached after about 1s. Therefore, this work will support the development of necessary key technologies for cooling of highly thermally loaded components and the necessary vacuum connection technologies. In addition, proposals are being developed to optimize the electron beam generator for continuous wave operation.

In the present work, two different electron gun concepts were pursued and optimized regarding DEMO relevant requirements. In the first step, the conventional triode electron gun technology was advanced. This was the first time that an existing electron gun with anti-emission coating at the emitter edges was tested in Europe. The use of this emitter technology significantly reduces the sensitivity to manufacturing tolerances and thermal expansion. In the present work, this MIG was numerically optimized and tested experimentally with the long-pulse tube. In addition, it is shown that this MIG can also be operated in a diode configuration. Therefore, an advanced anode shape was developed which satisfies the gun design criteria and promises the suppression of trapped electrons. In order to increase the operating frequency and output power in terms of a DEMO relevant design, an optimized MIG has been systematically developed. The main requirements of a novel electron gun are: (i) minimizing the temperature of thermally stressed components to avoid thermal expansion during nominal operation, and (ii) maximizing the emitter surface area for a given borehole diameter of the superconducting magnet, to increase the beam current and accordingly the output power. With a conventional MIG these requirements cannot be fulfilled, because the design, with the same dimensions, does not allow the possibility of a larger emitter assembly. However, these goals could be achieved by using the concept of an inverse MIG (iMIG). In the iMIG a 16.8 % larger gyrotron emitter ring can be installed without the necessity for a bigger bore hole in the superconducting magnet. Due to the increasing circumference the electron beam compression is increasing which leads to a thinner electron beam and an efficient gyrotron operation at higher operating frequencies. In addition, the larger emitter surface provides a higher beam current and allows the gyrotron to operate at higher RF-power levels. Furthermore, the iMIG design was simplified for an in-house manufacturing. The temperature of thermally loaded MIG components could be reduced by the factor of 5 compared to conventional MIGs. The significant temperature reduction is related to the use of an advanced construction and optimized material composition. In numerical simulation, an excellent electron beam quality has been achieved. In addition, the gun design criteria for the suppression of trapped electrons and the generation of Halo electrons were strictly considered during the development phase of the iMIG.
In order to build cost-effective DEMO-relevant prototypes in the future, another focus was on cost-optimized joining technologies placed. Intensive research has shown that the use of basis-nickel super alloy braze represents an excellent alternative to the already well-known gold and silver braze. In particular, the

evaluation of grinding-patterns has shown that the tolerances and leakage rates have been improved by the optimized process. Thanks to the optimized brazing process, it is now possible to inexpensively manufacture KIT internally long-pulse gyrotron components.
In order to increase the pulse length from 4 ms to 150 ms, the modular components of the coaxial gyrotron were separately equipped with a novel cooling method. This unique optimization allows to record the electrical losses of each component. However, to enable the goal of CW operation, an optimized minichannel cooling design has been developed for the cavity and successfully experimentally tested on a mockup. Numerical investigations has shown, that the maximum steady-state temperature of the cavity, equipped with a minichannel cooling, reaches 210 °C during nominal operation. A further significant reduction of the temperature can be achieved with the novel spray cooling system. Due to the phase change of the water from liquid to vapor, 10 times more energy can be dissipated compared to a usual minichannel-cooling system. Experimental tests and evaluations have shown the enormous potential of that cooling approach. Furthermore, the spray cooling system offers significant advantages in temperature monitoring and control.
Experimental tests of the KIT internally manufactured coaxial-cavity gyrotron have successfully confirmed the optimization and development steps of the key components. A maximum output power of 2.2 MW at an operating frequency of 169.89 GHz was measured. Due to the optimized manufacturing process and the reduced tolerances, the electronic efficiency could be increased by 4 % compared to the short-pulse gyrotron. Even more, in depressed operation an output power of 2.2 MW has been achieved with the advanced conventional Magnetron Injection Gun.

Contents

List of used symbols and variables

Symbols and variables

B	Magnetic flux density
B_C	Magnetic flux density at the cavity
B_E	Magnetic flux density at the emitter
b	Magnetic compression
c	Speed of light in vacuum
e	Elementary electron charge: $1.602 \cdot 10^{-19}$ C
$e\Phi$	Work function
E_E	Electric field strength at the emitter surface
f_{cyc}	Cyclotron frequency of the electrons
I_b	Electron beam current
J	Current density
k_z	Wavenumber
k_B	Boltzmann constant
m_e	Elementary electron mass: $9.109 \cdot 10^{-31}$ kg
P_{th}	Thermal power
P_{el}	Electrical power
R_b	Electron beam radius at the cavity

R_E	Emitter radius
R_i	Insert radius
R_R	Inner wall radius of the cavity
T_e	Electron temperature
$v_\perp$	Electron speed in transversal direction to tube axis
$v_\parallel$	Electron speed in parallel direction to tube axis
V_{acc}	Acceleration voltage
W_{kin}	Kinetic energy of electron
α	Pitch factor
$\Delta\alpha$	Pitch factor spread
$\beta_{\parallel,\perp}$	Normalized velocity in parallel or perpendicular direction
ΔR_B	Electron beam thickness
ΔV	Voltage depression
$\delta\beta_\perp$	Transversal velocity spread
$\delta\beta_\parallel$	Parallel velocity spread
φ_{EB}	Angle between emitter surface and magnetic field at the emitter position
γ	Relativistic factor
λ	Wavelength
Ω_c	Angular cyclotron frequency of the electrons
ω_{RF}	RF frequency
Al_2O_3	Alumina
BaO	Barium oxide
CaO	Calcium oxide

cMIG	Conventional magnetron injection gun
CVD Disc	Chemical vapor deposited diamond disc
CW	Continuous wave
D	Deuterium
DEMO	DEMOnstration power plant
EUDEMO	European DEMOnstration power plant
ECRH	Electron cyclotron resonance heating
He	Helium
KIT	Karlsruhe Institute of Technology
ICRH	Ion cyclotron resonance heating
iMIG	Inverse magnetron injection gun
n	Neutron
NBI	Neutral beam injection
OFHC	Oxygen free copper
Os	Osmium
Re	Rhenium
RF	Radio frequency
SCM	Superconducting magnet
T	Tritium
TE	Transversal electrical mode
W7-X	Wendelstein 7-X

1 Introduction

In this chapter an overview of the gyrotron as a high power source for fusion application is given. After reconsideration of existing challenges in fusion gyrotron developments, the currently available technologies are evaluated. Based on that, the scope and motivation of this work is described.

1.1 Towards DEMO: requirements for future fusion gyrotrons

More than 90 % of the world energy production is covered by fossil energy sources. The associated climate problem, limited fuel stocks and political instabilities makes alternative energy systems in the long-term necessary. Today, Europe's baseload generation of energy relies on nuclear fission and lignite [1]. In order to put the world on a path of reduced greenhouse gas emission and pollution related to radioactive waste, a sustainable research in thermonuclear fusion is of crucial importance. The goal of nuclear fusion is to obtain energy from fusion of nuclei, as it happens in the sun. Under terrestrial conditions deuterium and tritium fuse most readily. In this process a helium nucleus is produced, attended by a neutron and a large quantity of usable energy. The resulting helium atom is lighter than deuterium and tritium together, accordingly some mass has been lost and great amounts of energy have been gained. The equivalence between mass and energy is postulated by Einstein [2]:

$$E = m \cdot c^2 \tag{1.1}$$

This chemical process can be described by the reaction equation, which was for example published by Shultis et al. [3]:

$$ {}^{2}_{1}T + {}^{3}_{1}D \rightarrow {}^{4}_{2}He + 3.5\ \text{MeV} + n + 14.1\ \text{MeV} \tag{1.2} $$

The total energy gain of 17.6 MeV consists of the kinetic energy of the neutron (14.1 MeV) and the Helium nucleus (3.5 MeV). One gram of the combustible has the possibility to generate 90000 kWh in a fusion power plant, which corresponds to a combustion energy of 11 tons of coal. Deuterium can be extracted from water while Tritium will be breeded during the fusion reaction by the interaction between the fusion neutrons with blanket Lithium in the following reaction [1], where an alpha particle is released:

$$ {}^{6}Li + n \rightarrow \alpha_{rad} + {}^{2}_{1}T + 4.78\ \text{MeV} \tag{1.3} $$

In this connection it is not necessary to have 100 % enriched Li_6. Both nuclei (Deuterium and Tritium) are positively charged. Therefore, the Coulomb barrier has to be exceeded for a successful fusion reaction. A kinetic energy of 10 keV (150 Mio °C [1]) is required to pass that Coulomb force. In order to reach such a high plasma temperature, a powerful heating system is required. There exist exactly four heating methods which are used in today's fusion reactors.

- Ohmic Heating (Tokamak)
- Neutral Beam Injection (NBI)

and the RF-heating methods:

- Ion Cyclotron Resonance Heating (ICRH) (direct ion heating)
- Electron Cyclotron Resonance Heating (ECRH) (indirect ion heating)

The ECRH methods heats the electrons in the plasma due to the resonance effect with the electromagnetic wave. The energy exchange takes place at the

frequency of the cyclotron resonance of the electrons. This relation is for example published by Kartikeyan et al. [4].

$$\Omega_c = 2\pi f_{cyc} = \frac{eB}{m_e\gamma} \approx \frac{28\ \text{GHz} \cdot B}{\gamma} \tag{1.4}$$

The magnetic flux density B in Eq. (1.4) must be used in Tesla. During the indirect heating the accelerated electrons transfer the energy to the ions via collisions. ECRH is playing a superior role in plasma heating of future nuclear fusion devices. Firstly, it is because ECRH offers excellent localized coupling of the RF power to the fusion plasma, which is related to the resonance condition. Secondly, the ECRH has the highest input power density. For typical fusion reactors the resonance frequencies are in the range between 100 GHz and 300 GHz. The today's ECRH heating power is 10 MW for the stellarator Wendelstein 7-X [5]. The heating power in the first campaign for the tokamak ITER is 24 MW [6].
The fusion reactor, which shall follow ITER, is the DEMOnstration fusion power plant (DEMO). The goal of DEMO is the generation of 2-3 GW of thermal power P_{th} and 500 MW of electrical power P_{el} [7]. Another goal is the demonstration of the reliability and availability of the system as well as the verification of new constructions, technologies and the self-production (breeding) of tritium [8]. Based on the time frame of the fusion program, the commissioning of DEMO is planned around 2050 [9]. For the European DEMO (EU DEMO) design, an ECRH power of 50 MW is foreseen. Details of the ECRH system are discussed by Jelonnek et al. [10] and Franke et al. [11, 12].
The European Union 2018 DEMO baseline (EU-DEMO-2018 baseline published by Federici et al. [13]) design goals for a DEMO gyrotron together with today's technological constraints are listed below. These gyrotron relevant design goals are already published by Kalaria [14].

- A multi-frequency/multi-purpose operation at 170 GHz, 204 GHz and 236 GHz for plasma start-up, bulk heating and non-inductive current drive.
- A frequency step-tunability in steps of 2-3 GHz for plasma stabilization.
- An RF output power of minimum 2 MW to reduce the number of gyrotrons, which are required for a sufficient ECRH.

1.2 State of the art of fusion gyrotrons

Kartikeyan et al. is writing in [4] that the only known RF source which is capable to produce the required RF power level in the desired frequency range is the gyrotron. This vacuum tube is operating in the millimeter and sub-millimeter wavelengths range with an output power range from the kW level up to the multi-MW level. As an example, for Wendelstein 7-X (W7-X) in Greifswald, Germany, in total ten 1 MW 140 GHz gyrotrons [15–17] are successfully in operation. The gyrotrons are designed for a pulse length up to 1800 s. The transmission of the RF power to the vessel is realized by an efficient and reliable quasi-optical transmission system. Further details and measurement results can be found in Erckmann et al. [5]. For the fusion project ITER in Caderache (France), 24 gyrotrons with an RF output power of 1 MW each and a frequency of 170 GHz are successfully under experimental testing. A detailed actual status overview about ITER gyrotrons is given by Thumm et al. [17] and a detailed European status by Ioannidis et al. [18]. The requirements for these gyrotrons are a maximum pulse length of 3600 s with an RF output power of minimum 1 MW [19].

1.3 Scope of this work

Status of modular gyrotron development

At KIT, the activities in gyrotron R&D focus on a design that meets the requirements for a future DEMO power plant, which are presented by Federici et al. [20]. For future DEMO gyrotrons an RF output power of minimum 2 MW (CW) with operating frequencies up to 240 GHz is under consideration. Kern et al. [21] and Rzesnicki et al. [22] published that those output power levels can be handled in CW operation by the coaxial-cavity gyrotron technology. Compared to the hollow-cavity gyrotron technology as used for e.g. Wendelstein 7-X and ITER, the coaxial-cavity gyrotrons allow the operation at even higher order modes and therefore at higher output power levels. An operation at higher order modes is possible by the use of a coaxial-insert, which reduces the mode competition in the cavity. The mode competition is reduced due to the mode selectivity of the corrugated inner conductor (insert) [23].

Piosczyk et al. [24], Rzesnicki et al. [25] and Gantenbein et al. [26] have already shown the potential of the coaxial-cavity gyrotron in first experimental results obtained with the modular 170 GHz 2 MW short-pulse coaxial-cavity pre-prototype at pulse length of 0.6 ms and an output power of 2.3 MW. Nevertheless, the coaxial-cavity gyrotron technology has not been verified at longer-pulses above a few ms until today.

Objectives

The main objective of the present work is the verification of the coaxial-cavity technology at steady-state (thermal equilibrium) operation which will prove the long-pulse capabilities and requirements of a coaxial-cavity gyrotron. One of the main project requirements is to keep the modularity of the gyrotron, which opens the path of a cost-effective in-house manufacturing and the replacement of advanced components during the development. In order to reach the steady-state operation, first, an advanced Magnetron Injection Gun has to be developed. Second, a water cooling system has to be exhibited and implemented. Third, a vacuum tight joining procedure which is compatible to the KIT facility has to be developed.

The objective of an advanced Magnetron Injection Gun is the possibility employing larger emitters in order to increase the output power. A further motivation is a simple and feasible design with a unique cooling capability and a simplified conformance of the gun design criteria, which are defined by Pagonakis et al. [27].

Considering the mechanical and thermal limitations of a 2 MW long-pulse gyrotron, for the first time, a modular cooling approach for each component should be developed. Here, different advanced cooling mechanism should be thermomechanically and experimentally evaluated. The focus is on the development of innovative and unique cooling approaches with significantly higher cooling efficiencies and simplified handling compared to the currently used concepts.

In addition, advanced manufacturing processes and advanced brazing procedures should be developed for a KIT in-house compatible production. The focus should be spent to cost-efficient brazing, which represents a reliable alternative to the expensive gold and silver brazes. The influence of the process parameters should be investigated and optimized for a reliable and reproducible welding procedure.

2 The gyrotron: fundamentals of operation

The technological fundamentals of a gyrotron will be given in the following chapter. First, the working principles of the gyrotron key components are described. Second, a thorough introduction will be given of the generation of proper electron beams in fusion gyrotrons with the focus on different Magnetron Injection Guns and currently used emitter technologies.

2.1 The working principle of the gyrotron

The gyrotron is a fast-wave vacuum electron oscillator, which is operating in the millimeter and sub-millimeter wavelength range. Current gyrotron developments (see e.g. Idehara [28]) extend the frequency range into the THz-regime. In Fig. 2.1 a schematic drawing of a gyrotron with its components is shown. The main components of a gyrotron are: the magnetron injection gun (MIG), the beam tunnel, the cavity, the launcher, the mirror box, the diamond output window, in case of a coaxial-cavity gyrotron the insert, the collector and the cold superconducting magnet. A more detailed introduction and comprehensive overview is given in Gilmour [29] and Kartikeyan et al. [4].

Starting from the MIG a hollow electron beam is emitted from the heated emitter by temperature limited thermionic emission [4]. The electrons are accelerated between the cathode and anode by an applied voltage. Due to the externally applied magnetic field the electrons start to gyrate. Due to the two directions of motion the electrons move on a helix trajectory. Through the following beam tunnel the magnetic flux density $B_{\parallel}$ is increasing, which results in an increasing transverse velocity component $v_{\perp}$. Due to the energy conservation an energy transfer from the parallel motion to the perpendicular motion takes place. This transfer is necessary because the interaction in the cavity takes place with the transverse electric field component. In the cavity

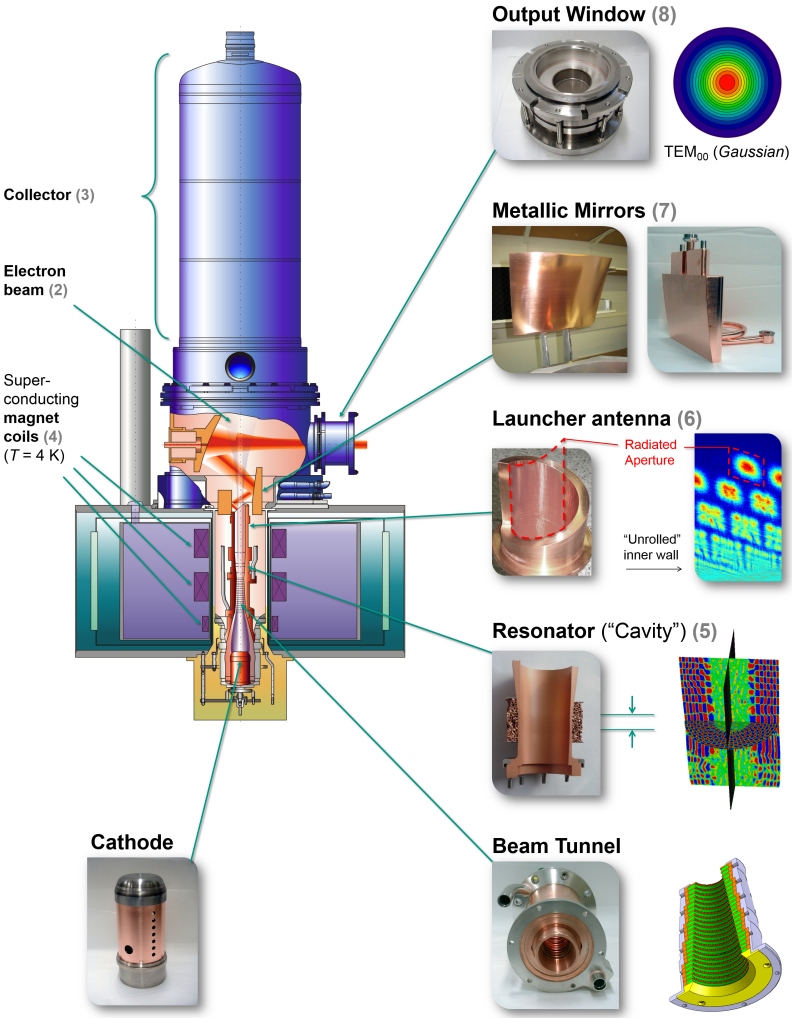

Figure 2.1: Sketch of a high power gyrotron with all the sub components.

the traveling electrons transfer a part of their transverse kinetic energy to the transverse electric mode which is close to its cutoff. Since the gyrotron interaction takes place between an electron beam with a fast RF wave the gyrotron is considered as a fast-wave device. This allows to design the cavity-structure as a multiple of the wavelength and leads to a much higher power handling capability. The generated electromagnetic wave in form of a higher order mode, e.g. $TE_{34,19}$ travels into the direction upwards to the quasi optical mode converter. The mode converter consists of a launcher and several focusing mirrors. In the quasi optical mode converter the TE mode is converted into a gaussian mode. More detailed investigations and fundamentals of the quasi optical mode converters are presented by Flamm [30] and Jin et al. [31] [32]. The gaussian mode exits the gyrotron through the chemical vapor deposited diamond disc (CVD disc). The electron beam travels towards the collector where a part of the residual energy is recovered from the electrons. Externally installed sweeping coils sweep the electron beam. This procedure lowers the maximum wall loading at the collector and increases the lifetime.

The energy exchange in the gyrotron

The trajectories of the electrons have been already discussed in the former section. The gyration behavior of the electrons is extensively described by Ginzburg [33] and can be described by using the cyclotron frequency, as shown in Eq. (1.4). The relativistic Lorentz factor γ can be formulated as (see e.g. Oak [34]):

$$\gamma = \frac{1}{\sqrt{1 - \frac{v}{c_0}}} = 1 + \frac{W_{kin}}{m_e c_0^2} \approx 1 + \frac{W_{kin}}{511\ keV} \tag{2.1}$$

with the kinetic energy W_{kin} in keV. If a synchronous RF field is superimposed on a static magnetic field $\omega = \Omega_c$ some electrons will be decelerated and transfer energy to the RF field, others against it are accelerated and gain energy, depending on the phase position of the RF field (see Jelonnek [35]), as shown in Fig. 2.2. Electrons, which release energy, become lighter and the cyclotron frequency is approaching the RF-frequency and remains longer in

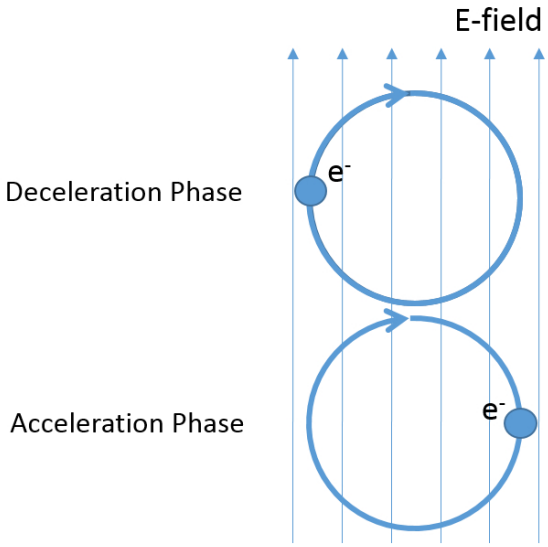

Figure 2.2: Phase focusing of electrons in an RF-field in the gyrotron cavity [35].

the resonance conditions. Electrons, which gain energy, increase the frequency difference and change faster the position relative to the phase of the field. These electrons are moving in a more favorable phase position [4]. If the change in the cyclotron frequency is large enough (due to the relativistic behavior), the electrons will accumulate in the decelerating field for a certain time were they release energy [35]. This process is called bunching [36]. If the bunched electrons remain too long in the RF-field, the electrons gain energy from the RF-field back. This effect is called overbunching, see e.g. Jory et al. [37]. The kinetic energy of the electrons during the interaction with the RF-field is shown in Fig. 2.3. The electrons cross the defined interaction region with the velocity $v_{\parallel}$. The interaction time τ when the electrons pass the cavity is limited. The time τ has to be selected that overbunching will be prevented. The electrons are moving relatively to the RF-field, therefore the frequency ω is shifted by a Doppler term [36]. The resonance condition is:

$$\omega - k_{\parallel} v_{\parallel} = \Omega_c \tag{2.2}$$

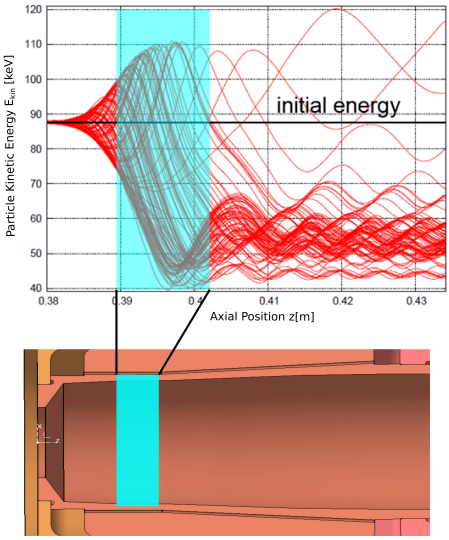

Figure 2.3: Energy level of electrons during the interaction with the RF-field [38].

Based on Eq. (2.2) it becomes clear, that the oscillation frequency of the RF-field have to be somewhat larger than the electron cyclotron frequency, so that a bunching can occur [35]. The dispersion hyperbola is defined as

$$\omega = c_0 \sqrt{k_\perp^2 + k_z^2} \tag{2.3}$$

of the single modes together with the beam lines can be entered into the so called Brillouin diagram, as done e.g. in Edgecombe [39] and Flamm [30]. Possible oscillation frequencies arise from the intersections and points of contact. In the Brillouin diagram, as shown in Fig. 2.4, possible operating points are highlighted. At point 1 $k_\parallel$ is small. Here the operating frequency in the waveguide is close to cut-off. This operating point marks a typical gyrotron interaction point. For $k_\parallel \ll 0$, a backward wave at the first harmonic is shown. The point 1 and 3 are forward waves at the first and second harmonic, respectively. The corresponding theories are precisely described in Jelonnek [35] and Kern [40].

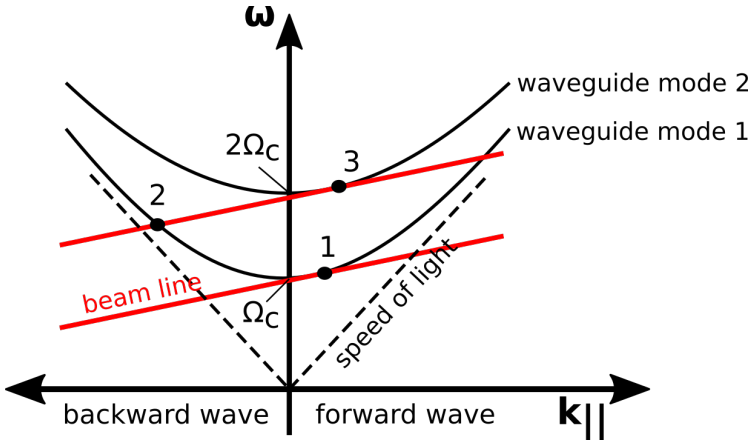

Figure 2.4: Dispersion diagram of three possible operating modes with the electron beam line (red) and the speed of light.

2.2 Fundamentals of coaxial-cavity gyrotrons

The main advantages of the coaxial insert are the better mode selectivity at first place [40]. In addition, the coaxial-cavity gyrotron offer reduced voltage depression in gyrotrons. Here, the voltage depression ΔV reduces the acceleration voltage V_{acc} by V_b [4, 36] and is strongly dependent on the cavity and insert geometry, according to

$$\Delta V = |V_{acc} - V_b| \approx -60V \cdot \frac{I_b/A}{\beta_\parallel} \ln\left(\frac{R_b}{R_r}\right) \frac{\ln\left(\frac{R_b}{R_i}\right)}{\ln\left(\frac{R_R}{R_i}\right)} \tag{2.4}$$

The radii of the insert and the cavity are denoted as R_i and R_R. The beam current as I_b and beam radius as R_b. The voltage depression has a significant influence to the resonance conditions and the pitch factor α. With increasing voltage depression the pitch factor is increasing and mirroring of the electron beam can be a problem, as stated in e.g. Beringer [36]. In addition, the velocity spread in axial direction will increase, which lowers the electron beam

quality. Therefore, the maximum achievable beam current can be derived for the limiting case $\beta_{\parallel} \rightarrow 0$ [4, 40]:

$$I_{lim} \approx 17070A \cdot \frac{\gamma \cdot \left(\frac{\beta_{\parallel}}{\sqrt{3}}\right)^3}{2\ln\left(\frac{R_R}{R_b}\right)\frac{\ln\left(\frac{R_b}{R_i}\right)}{\ln\left(\frac{R_R}{R_i}\right)}} \tag{2.5}$$

Based on the parameters of the KIT coaxial-cavity gyrotron, the dependency of the voltage depression and limiting current versus the radius of the insert R_i is presented in Fig. 2.5. The beam radius is R_b = 10.0 mm, the cavity radius R_R = 32.5 mm, the relativistic factor γ = 1.17, the beam current I_b = 75 A, and $\beta_{\parallel}$ = 0.32. For conventional gyrotrons without a coaxial insert $R_i \rightarrow 0$ the voltage depression ΔV is significantly higher compared to a coaxial cavity gyrotron, as shown in Fig. 2.5. Consequently, the limiting current is smaller in conventional gyrotron configurations. There is a limit for the voltage depression of a conventional gyrotron that is determined by the electron beam properties and gyrotron geometry.

However, in CW operation the electron beam tends to neutralize partly due to ions in the vacuum. In this condition, the voltage depression of a partly neutralized electron beam in a hollow cavity is of the same level compared to the depression voltage of a non-neutralized beam in a coaxial-cavity gyrotron, see Franck [41]. The partially neutralization effect was investigated by Schlaich et al. [42, 43] and Pagonakis et al. [44]. Here, a maximum value of about 60 - 70 % neutralization can be expected.

As a result, the coaxial cavity gyrotron is the only approach for the operation in the multi-MW class regime and above. Therefore, KIT is pushing the coaxial gyrotron technology towards a DEMO relevant design.

2.3 The generation of the electron beam

In the previous section the energy exchange in gyrotron cavities was briefly discussed. For an efficient interaction a well-defined electron beam of highest quality is necessary. Therefore, the relevant key components and parameters of a MIG will be discussed in the following sections.

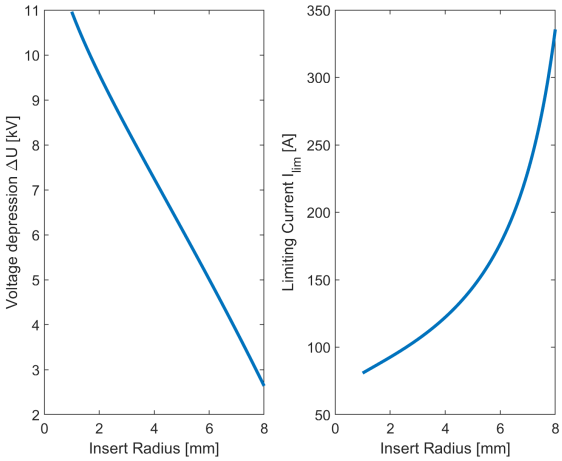

Figure 2.5: Voltage depression and limiting current versus the radius R_i (1 mm to 8 mm) of the coaxial insert in short-pulse operation.

2.3.1 The magnetron injection gun

In gyrotrons, Magnetron Injection Guns (MIG) are used for the generation of a helically shaped hollow electron beam. In Fig. 2.6 the axial cross-section of a MIG with coaxial insert is shown, including the main elements. The electrons leave the heated emitter by a thermionic emission. More details are presented in Zhang [45], Bretting [46] and Eichmeier [47]. The electrons are accelerated towards the anode due to a high electric field. The parallel and transverse velocity components ($v_\perp$ and $v_\parallel$) are related to the nearly radial electric field and nearly axial magnetic field in the emitter region [29]. The velocity ratio between the transverse and parallel velocity is called pitch factor α.

$$\alpha = \frac{v_\perp}{v_\parallel} \tag{2.6}$$

The electron beam should have a pitch factor as high as possible, so that a high RF output efficiency can be achieved, see e.g. Manuilov et al. [48]. The MIG forms a helical electron beam with a significant spread of the transverse

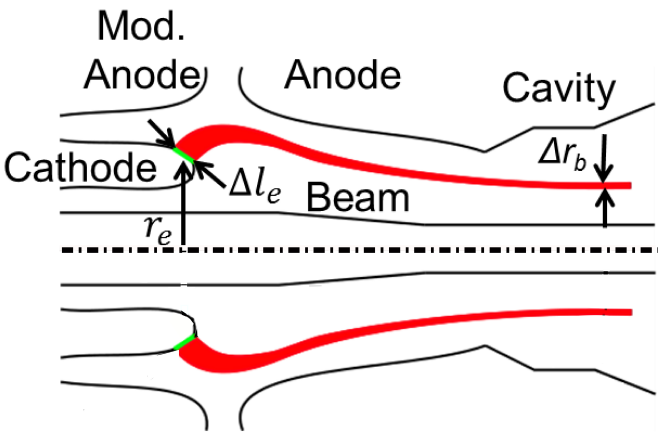

Figure 2.6: Cross section of a gyrotron in triode configuration.

and parallel electron velocities. A detailed introduction in electron beam generation and parameters is given in Tsimring [49] and Zapevalov et al. [50]. In a first approximation at the interaction region the normalized transverse velocity $\beta_\perp / c$ depends on the operating and geometrical parameters [4].

$$\beta_\perp \approx \frac{1}{\gamma \cdot c_0} \sqrt{b} \frac{E_E \cdot \cos(\varphi_{EB})}{B_E} = \frac{1}{\gamma \cdot c_0} \sqrt{\frac{B_c}{B_E^3}} \cdot E_E \cos(\varphi_{EB}) \tag{2.7}$$

Here, φ_{EB} describes the angle between the magnetic field direction and the emitter surface. It can be seen, that by variation of the magnetic field configuration in the emitter region, the pitch factor can slightly be tuned. The pitch factor is varying between different electron trajectories which causes a velocity spread in α. The transverse spread in α can be estimated by [14]:

$$\Delta\alpha = \left(1 + \alpha_0^2\right) \cdot \delta\beta_\perp \tag{2.8}$$

Here, $\delta\beta_\perp$ is the root-mean-square (rms) value of the normalized transverse velocity component $\beta_\perp = v_\perp/c$ and α_0 is the mean value of the velocity ratio. Possible reasons for an increased spread are [4]:

Related to the construction and misalignment:

- Inhomogeneous electric field distribution at the emitter surface.
- Slant angle of the emitter.
- Misalignment in the beam forming components (emitter, cathode, anode, body and magnet).

Related to emitter technology:

- Inhomogeneous emitter temperature distribution.
- Surface roughness of the emitter.

The magnetic flux density is increasing from the emitter position B_E towards the beam tunnel and cavity B_C. During the increase of the magnetic flux density the beam is compressed from the emitter radius R_E down to the average beam radius at the cavity R_C based on the adiabatic compression. Here, energy is transferred from the longitudinal to the transverse velocity component, which results in an increasing pitch factor α towards the cavity. The compression ratio b and its dependency is given as [4, 29]:

$$b = \frac{B_C}{B_E} = \left(\frac{R_E}{R_C}\right)^2 \tag{2.9}$$

In addition, the thickness of the electron beam is also reduced by the increasing magnetic flux density [14].

$$\Delta R_B = \frac{R_{B,max} - R_{B,min}}{\sqrt{b}} \tag{2.10}$$

The phenomenon of the beam compression is called adiabatic compression and can be derived from the Busch Theorem, see Groening et al. [51].
All the previously mentioned parameters have to be considered during the design and development of a MIG. The main MIG types which are used

in fusion gyrotrons and gyrotron prototypes are the conventional MIG, the conventional coaxial-cavity MIG and the inverse MIG. The actual differences as well as advantages and disadvantages are discussed below.

Conventional magnetron injection gun: diode type versus triode type

The conventional MIG can be classified into two types, the diode type MIG and triode type MIG. The diode configuration has the advantage of a simple and robust structure and a reliable operation. The triode configuration, implemented e.g. in Kumar et al. [52] and Kajiwara et al. [53] has an additional modulation anode (see Fig. 2.7). This additional anode provides the possibility to adjust the electric field at the emitter surface, without a change in the beam voltage. The variation of the modulation anode potential allows a better control of the beam parameters, especially of the pitch factor α. However, in triode configuration an additional power supply is required, which increases the maintenance and operational costs. Diode type MIGs are the most common implemented guns in European, Russian and USA high power fusion gyrotrons, which are being applied in W7-X and ITER gyrotrons.

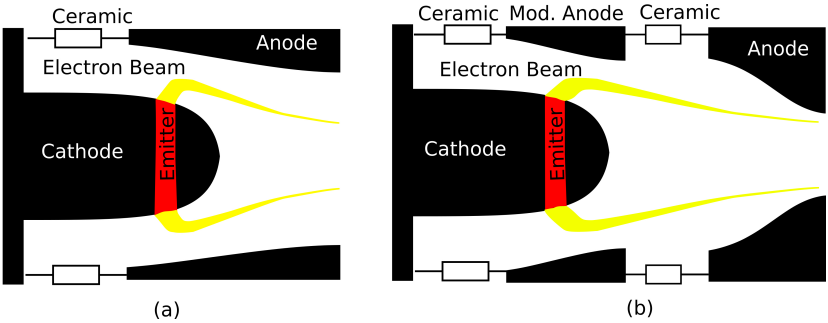

Figure 2.7: Configuration of a conventional diode type MIG (a) and triode type MIG (b).

Coaxial-cavity magnetron injection gun

The MIG configurations, as shown in Fig. 2.7, can be expanded by a coaxial-insert (Fig. 2.8). The differences and limitations of a diode and triode approach in a coaxial cavity gyrotron is presented in Rode et al. [54]. In this configuration an additional ceramic has to be installed to isolate the insert from the cathode. The insert has to be aligned after each reassembly. However, the performance of the coaxial-cavity MIG is independent of the insert.

Inverse magnetron injection gun

In addition to the conventional MIG an alternative approach is the inverse Magnetron Injection Gun, which was already investigated in Ruess et al. [55] and Lygin et al. [56] (as shown in Fig. 2.9). The inverse MIG, published in Lygin et al. [56], is using a similar geometrical structure compared to a conventional MIG, however, with the installation of an inverse emitter. The main difference to the conventional MIG is the emission towards the symmetry axis. The cathode in the present advanced inverse MIG configuration is placed at the outside and can be cooled directly by the isolation oil, which leads to a more optimum cooling mechanism and consequently to a lower temperature of the thermally loaded components. Furthermore, by keeping the same MIG diameter, the emitter in the inverse MIG can be significantly larger designed, due to the structural conditions of the outside positioned cathode. This main advantage of the inverse MIG offers the possibility for a higher beam current keeping the current density the same. Furthermore, by keeping the emitter

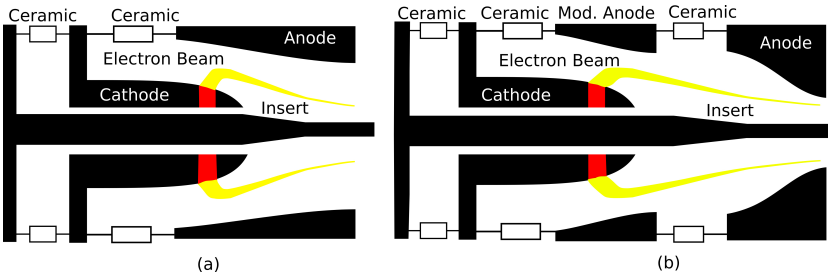

Figure 2.8: Diode type and triode type Magnetron Injection Gun in coaxial-cavity configuration.

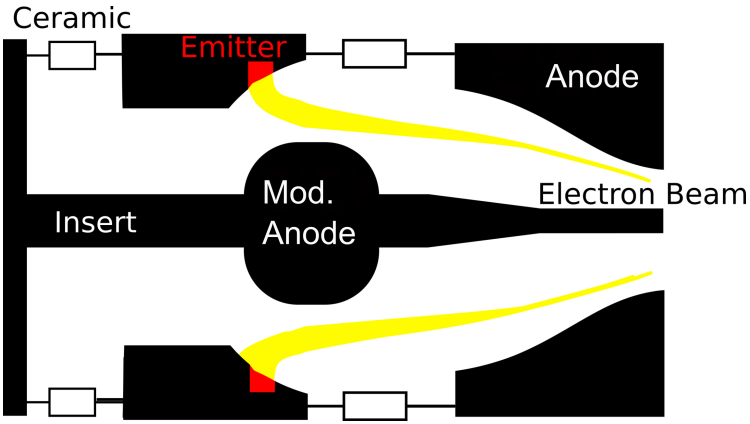

Figure 2.9: Schematic representation of the coaxial Inverse Magnetron Injection Gun.

radius constant the construction of an inverse MIG is more compact and a smaller and cost-efficient superconducting magnet can be used. Numerical investigations and thermomechanical simulations of an advanced inverse MIG will be presented in Section 3.2.

2.3.2 Emitter technologies

The emitter is usually made from a porous tungsten ring with an impregnation [46, 57] at the emitting surface. The pores of the tungsten bar are filled with a mixture of Al_20_3, BaO and CaO. The commonly used impregnation mixtures are B-type and S-type. The B-type impregnation consists of a mixture of 5 moles of BaO, 3 moles of CaO and 2 moles of Al_20_3 with a designation of 5:3:2 (work function of 2.13 eV) [29, 46]. The S-type emitter consists of a 4:1:1 (work function of 2.08 eV) designation. There are two types of emitter technology available off-the-shelf. The standard emitter technology (S- and B-type) and the M-type emitter. These M-type emitters are coated with Os, Os-Ru, Ir or Re [46]. Here, the coating layer, which is placed on top of the emitter surface, has a thickness of ~5000 Angstroms. The usual work function of a M-type emitter is 1.9 eV [46]. An additional emitter material is Lanthanum Hexaboride (LaB6), which is commonly used in Russian gyrotrons.

The work function is 2.6 eV. However, the vapor pressure is higher compared to dispenser emitters, which is related to the higher operating temperature of around 1400 °C.
For defined electron trajectories the emitter has to be operated in the temperature-limited regime [4]. In case of the space charge limited operation, an electron cloud is generated in front of the emitter, which reduces the electric field strength at the emitter surface. Eichmeier et al. is presenting in [57], that in temperature limited operation, the beam current is strongly dependent on the emitter temperature and the Schottky effect. With increasing temperature the emitter current is increasing which can be seen in the following Richardson-Dushman equation:

$$J = A_0 T^2 e^{-\frac{e\phi}{kT}} \ \mathrm{A/m^2} \tag{2.11}$$

However, in the same way the lifetime is significantly decreasing. This effect is related to the increasing evaporation rate of BaO with increasing temperature. The beam current density of today's dispenser cathodes is about 4 to 5 A/cm^2, see Gaertner [58]. The nominal operating temperature at the emitter surface is 1000 °C, with a lifetime of 10^4 hours (M-type) [58,59]. The current density can be doubled by increasing the emitter surface temperature to 1100 °C. Here, the expected loss in lifetime amounts 50 % [58].

2.3.3 Thermionic emitters for the generation of high current beams

Electron emission is already starting at temperatures larger than 0 K. Here, some electrons gain enough energy to overcome the work function and leave the emitter surface. As an example, Gilmour is writing in [29] that the average thermal energy of an electron at room temperature is 1/40 eV. However, the work function of a B-type emitter is 1.8 eV [45, 60]. Therefore, it becomes understandable, that the emitter temperature has to be significantly higher than room temperature in order to achieve the desired beam current. For the common used M-type emitters the nominal operation temperature is 1000 °C at the emitter surface and 1300 °C at the emitter filament.
The energy level of electrons in the emitter and vacuum area is shown in Fig. 2.10 [29]. At the emitter, the electron energy level shows a parabolic behavior, which is related to collisions with adjacent atoms. The top part of

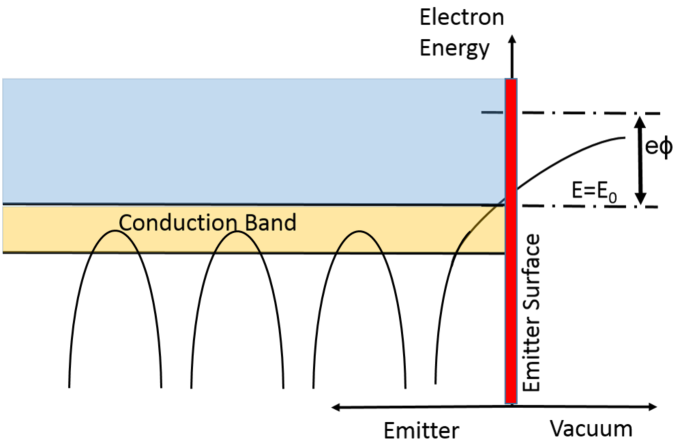

Figure 2.10: Energy level of electrons near the emitting surface [29].

the energy levels merge to the conduction band [29]. For emission, the electrons have to overcome the difference between the top-level of the conduction band and the vacuum level, which is known as the work function $e\Phi$. The usual temperature of common thermionic cathodes are between 600 °C and 2200 °C, as stated in Gilmour [29] and Becker [61]. At these operating temperatures, the work function is 20 times higher than the average thermal energy of the electrons. If a small amount of the available electrons in the emitter overcome the work function, it is already sufficient to achieve the required operating beam currents.

In the Richardson-Dushman equation, as shown in Eq. (2.11), the electron emission takes place by a thermionic emission. The effect of an electric field at the cathode has not been taken into account. In the experiment, it is found out, that an applied electric field increases the electron emission, which is known as the Schottky effect. The reason for an increasing electron emission is the reduction of the energy barrier, which an electron has to overcome to leave the emitter surface. That means, that the applied electric field reduces the work function by

$$\Delta\phi = e\phi - eU \tag{2.12}$$

U describes the voltage between anode and cathode. The modified Richardson-Dushman equation can be written as [29, 39]:

$$J = A_0 T^2 e^{-\frac{e(\phi - U)}{k_B T_e}} \tag{2.13}$$

The main emitting mechanisms in a thermionic cathode are summarized in Fig. 2.11. The current is space charge limited at low voltages. In this case, the electrons are in a none well-defined trajectory, which is related to the generation of a space charge cloud in front of the emitter surface and a reduction of the electric field [29]. Therefore, this kind of operation is not suitable for an efficient gyrotron operation [29]. With increasing voltage the emission goes into the temperature limited operation. The beam current can be mainly increased by increasing the emitter temperature, however with increasing voltage the beam current is slowly increasing due to the Schottky effect [29]. It has to be mentioned that the Schottky effect has only a small influence regarding an increasing beam current. With even higher voltages the field emission occurs. This kind of emission is related to extremely high electric field strength at the emitter surface, which results in a significant increase of the beam current [29].

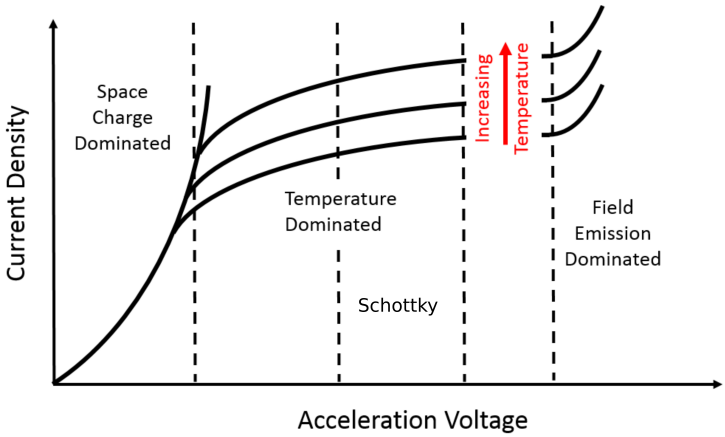

Figure 2.11: Summary of different emitting mechanism in thermionic cathodes [29].

3 Investigation of magnetron injection guns for future multi-megawatt long-pulse operation

The key component of the gyrotron is the Magnetron Injection Gun (MIG). The MIG forms the electrons into a helical beam with the beam properties required for an efficient interaction.
In order to reach the desired long-pulse operation in the multi-MW output power range, an advanced MIG has to be developed which satisfies the long-pulse relevant requirements. These are:

1. Larger emitter surface to increase the beam current for a given emission current density and lifetime.

2. Advanced cooling approach and material composition to lower the temperature and thermal expansion of thermally loaded components in order to guarantee a CW operation.

3. The advanced MIGs has to satisfy the gun design criteria, which are defined by Pagonakis et al. [62].

The Magnetron Injection Guns, which are presented in this chapter, are designed for the KIT coaxial-cavity 2 MW 170 GHz long-pulse gyrotron and simulated with the electron trajectory code ARIADNE, which is published in Pagonakis et al. [38]. For an efficient gyrotron interaction, an appropriate electron beam is required which has to fulfill the design criteria and requirements at the cavity center [62], which are listed in Tab. 3.1

Table 3.1: Appropriate electron beam parameters at the cavity center for the KIT coaxial-cavity 2 MW 170 GHz long-pulse gyrotron.

Beam Average Radius R_g $[mm]$	10.0
Beam Thickness Δr_b at 170 GHz [mm]	0.35
Pitch Factor α	1.2 - 1.4
Velocity Spread $\delta\beta_t$	minimized
Beam Energy V_b $[keV]$	90

3.1 Towards an optimized conventional magnetron injection gun design

A conventional MIG with coated emitter edges was already developed at KIT for the coaxial-cavity 2 MW 170 GHz gyrotron, see Pagonakis et al. [63]. The main advantage of the emitter coating is the reduced sensitivity regarding tolerances and misalignment. For scientific reasons, it was decided to built-up the conventional MIG in triode configuration. However, for an operation in a DEMO power plant the complexity should be minimized. Therefore, a conventional MIG with coated emitter edges in diode configuration will be systematically investigated.

3.1.1 Design and integration

The mechanical design of the conventional MIG can be seen in Fig. 3.1. The MIG is of triode type with a modulation anode on ground potential. Compared to the previously existing coaxial-cavity MIGs, the present design has anti-emission coated edges (green highlighted in Fig. 3.1) [65]. The significant advantage of the coated emitter edges is the reduction of the sensitivity regarding the manufacturing tolerances and radial thermal expansion of the emitter. The coating prevents the emission from the emitter edges, where a field enhancement and therefore the possibility of magnetically trapped electrons exist. Tolerance studies of the radial emitter position without an anti-emission have confirmed that even tolerances of some microns becomes critical. These fundamental numerical results are presented in Pagonakis et al. [65]. Here, the

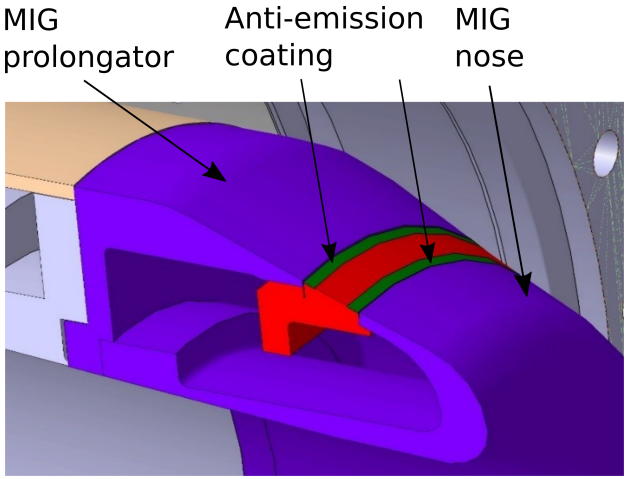

Figure 3.1: Advanced emitter with anti-emission coating (highlighted in green) for suppression of electron emission with high pitch factor from the edges [64].

electrons emitted from the emitter rims have a high pitch factor α, which is related to the field enhancement. Due to the magnetic compression the pitch factor α of these electrons is further increasing and mirroring can occur. A mathematical introduction is given in Sec. A.1. Some trapped electrons gain energy and have therefore enough energy to bombard the cathode and emit secondary electrons from the MIG prolongator and anode. At these regions, the electric field is enhanced which also leads to magnetically trapped electrons. As time progresses, the number of electrons will increase and forms a so-called beam halo. Therefore, possible secondary electrons emitted from the prolongator (as shown in Fig. 3.2 and Fig. 3.3 with an electron trajectory number > 118) have to be captured by the anode in order to suppress the trapping effect. In these figures, the electron trajectories are numbered in ascending order from the MIG nose to the MIG prolongator. Electrons with an electron trajectory number of 78 reach the maximum pitch factor of 2.35. This is related to the locally increasing electric field strength at the cathode nose. At the emitter position the pitch factor is approximately decreasing by 0.4, which is related to the by 70 µm embedded emitter.

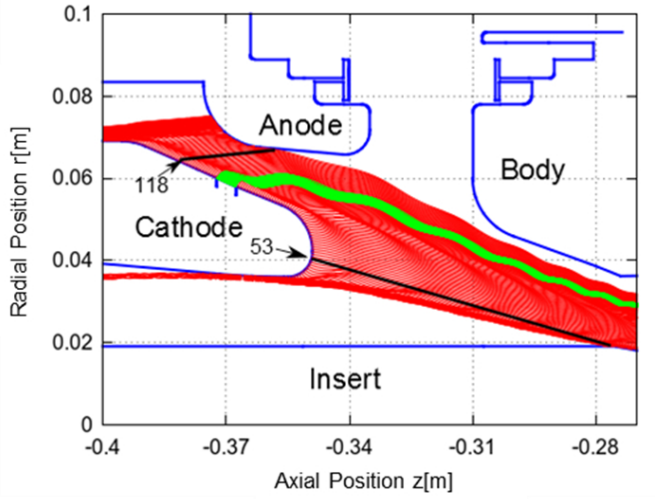

Figure 3.2: Physical design of the new conventional Magnetron Injection Gun operating in the long-pulse coaxial-cavity 2 MW 170 GHz gyrotron. The real electron beam is highlighted in green. Possible secondary electron trajectories are highlighted in red.

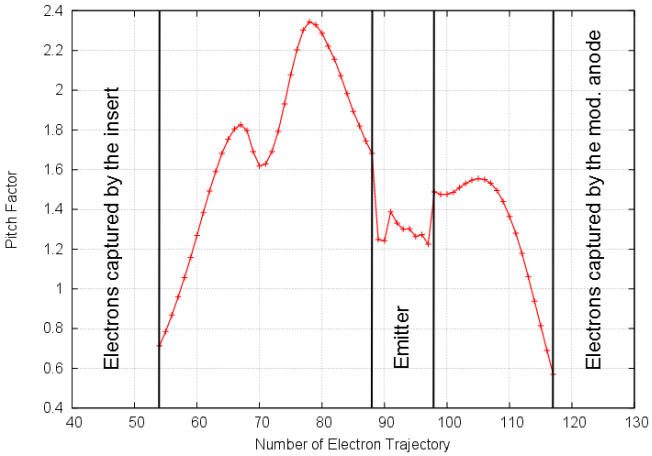

Figure 3.3: Pitch factor distribution (triode) of possible secondary electrons simulated in the cavity, which are emitted from the cathode surface.

3.1.2 Numerical investigations of a diode design

The already presented conventional MIG is of triode type. However, due to the increasing complexity during operation, it is not a promising solution for the operation in an industrial gyrotron. Therefore, a diode was developed for the very first time, which satisfies all the gun design criteria and is compatible to the conventional cathode with coated emitter for an operation at 170 GHz. The numerical analysis was performed with the in-house code ARIADNE. In Fig. 3.4 and Fig. 3.5 it can be seen that there are no trapped electrons between the MIG and cavity. A highlight is the very low maximum pitch factor of possible secondary electrons of 2.4, which is in the same level compared to the triode configuration. The maximum pitch factor is reached by electrons emitted from positions with a trajectory number of 10 (cathode nose front side), 24 (cathode nose outside) and 53 (cathode prolongator). This is additionally related the geometrical cathode curves and the corresponding electric field enhancement. In addition, the emitter is also embedded by 70 µm, which results in a lower pitch factor of the electrons emitted from the emitter position.

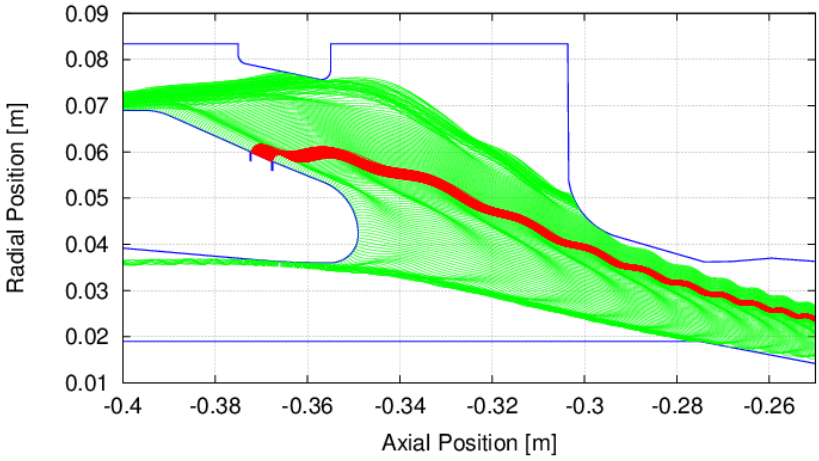

Figure 3.4: Advanced diode design, which is compatible to the cathode with coated emitter edges.

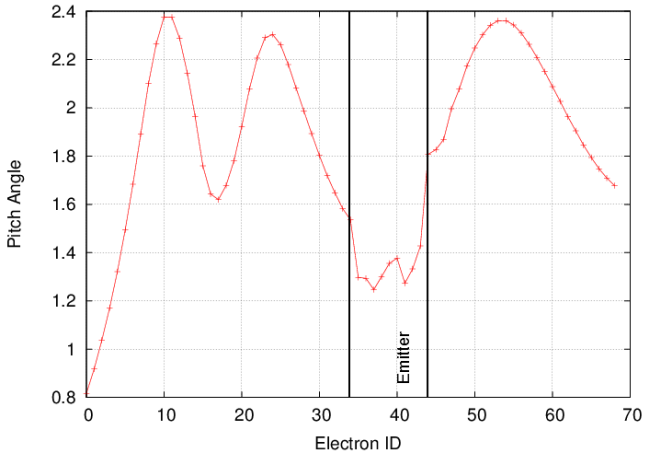

Figure 3.5: Pitch factor distribution of secondary electrons emitted from the cathode under consideration of a diode operation.

3.2 Design of a new compact inverse magnetron injection gun

In Section 3.1 an advanced conventional MIG with coated emitter edges has been presented. Based on the geometrical limitations, the emitter diameter cannot be increased by keeping the same outer MIG diameter. Even more, due to the conventional design, there is no optimization potential to reduce the thermal loading at the beamforming components. Therefore, in the following section, a completely new approach of an advanced and compact inverse MIG will be presented. This advanced and compact inverse MIG enables the implementation of a 16.8 % larger emitter compared to the currently used conventional MIG. In addition, with the inverse MIG approach and the optimized cooling capabilities the temperature of the beam forming components can be reduced from approximately 600°C down to 110°C.

Table 3.2: Simulated electron beam parameters in the cavity.

Guiding Center Radius R_g $[mm]$	10.0
Beam Thickness Δr_b $[mm]$	0.3
Pitch Factor α	1.3
Velocity Spread $\delta\beta_t$ [%]	2.4

3.2.1 Physical design

The fundamental principle of an inverse MIG for coaxial-cavity gyrotrons has been presented already in Advani et al. [66] and Lygin et al. [56]. The design proposed in the present work follows that basic principle. However, the proposed new inverse MIG design proposal is significantly more compact, which allows the installation of an emitter with a 6 mm larger diameter compared to conventional MIG implemented in the short-pulse coaxial-cavity pre-prototype. Furthermore, compared to the inverse MIG presented in [56, 66], the new inverse MIG design opens the path for a more efficient cooling of the beamforming components. In addition, it is matching the design of the EU 2 MW 170 GHz coaxial-cavity gyrotron, which is defined in e.g. Rzesnicki et al. [25]. The demanded beam parameters for this 2 MW gyrotron are presented in Tab. 3.3 [25]. A sketch of the proposed type of the inverse MIG is shown in Fig. 3.6.

The proposed design of an inverse MIG was optimized by using the self-consistent, electrostatic trajectory 3D code ARIADNE [38]. The optimization was realized for the cathode, body, insert and modulation anode to minimize the electron velocity spread of the electron beam and to provide the appropriate

Table 3.3: Nominal operating parameters of the KIT coaxial-cavity 2 MW 170 GHz long-pulse gyrotron.

Beam Voltage V_{beam} $[kV]$	90
Beam Current I_b $[A]$	75
Cavity Magnetic Field B_{cav} $[T]$	6.86

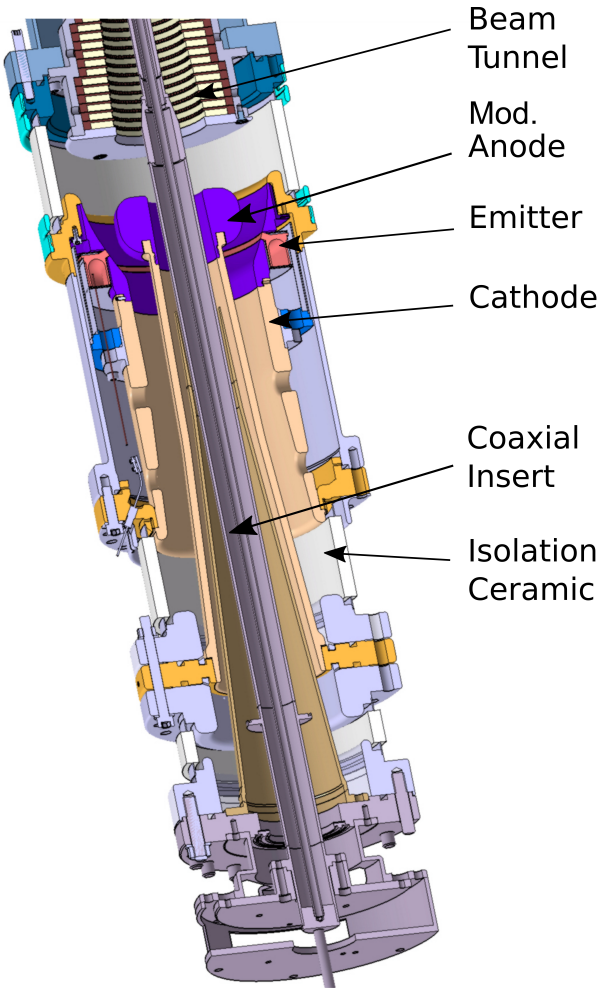

Figure 3.6: 3D Sketch of the designed inverse Magnetron Injection Gun.

electron pitch factor, beam thickness and beam radius at the cavity. In addition, the MIG was optimized to suppress the trapping mechanism and prevent the resultant beam Halo electrons. The structure of the proposed design including the magnetic field lines and the electron beam trajectories are shown in Fig. 3.7. Fundamental for the design of the inverse MIG is the emission of the electrons from the emitter inwards, towards the axis of the gyrotron.
As a main advantage the compact inverse MIG design allows the installation of a larger emitter area without to increase the outer diameter of the MIG. In the present inverse MIG design, the emitter radius is 62 mm with a horizontal thickness of 5 mm. The emitter has a tilt angle of 25 degrees regarding the axis of the tube. Compared to the conventional coaxial-cavity MIG the emitter surface of the inverse MIG is 16.8 % larger (comparison shown in Tab. 3.4), which is related to the compact approach and the consequent possibility to implement a larger emitter. Considering the usual current density of J_b = 4 A/cm^2, the current can be increased from 75 A (nominal conventional MIG) up to 87.6 A, with the same lifetime.
A step forward in the MIG history is the advanced concave shaped cathode, which reduces further the electric field and suppresses the generation of a beam halo. This fundamental idea has been realized for the first time in MIGs.
One of the main inverse MIG highlights is the direct cooling possibility of the outside positioned cathode. Here, the cooling efficiency can be significantly increased which results in a decreasing temperature and smaller thermal expansion of the beam-forming components. The improvements will be discussed in detail in Sec. 3.2.3.

Table 3.4: Comparison of the physical parameters between the compact inverse MIG and the conventional coaxial-cavity short-pulse MIG (conventional MIG)

Geometrical parameters of the emitter	inverse MIG	conventional MIG
Center radius [mm]	62.0	59.0
Horizontal thickness [mm]	5.0	4.5

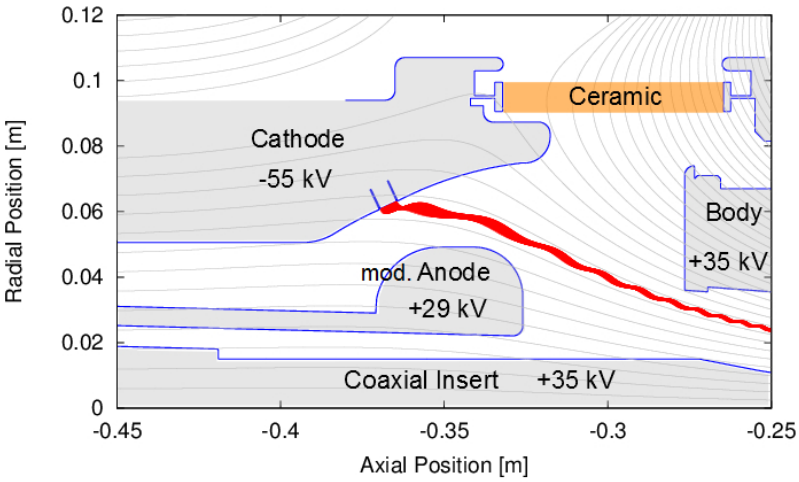

Figure 3.7: Geometrical shape of the electrodes with magnetic field lines and electron trajectories.

3.2.2 Suppression of trapped electrons

Trapped electrons and potential wells [67] in the gun region have a significant influence on the performance and stability of a gyrotron. With the new inverse MIG design trapped electrons can be much easier suppressed, which is related to the modulation anode and the concave cathode shape shown in Fig 3.8. Trapped electrons in the gyrotron can be caused by [62]:

1. Magnetically trapped electrons, which leads to the generation of a beam halo (already discussed in Section 3.1.1).
2. Potential wells, which leads to an accumulation of electrons or ions.

The generation and avoidance of the already mentioned effects will be discussed following.

Suppression of the beam halo

The electron beam halo is generated by magnetically trapped beam electrons between the MIG and the cavity. The main reason for magnetically trapped electrons is the secondary electron emission from the cathode which is caused by the emitter misalignment [27]. The following criteria prevent trapped electrons [55, 62]:

1. Magnetic field line does not cross the same equipotential line twice (magnetic potential well).
2. Secondary electrons emitted from the cathode surface are not magnetically trapped.
3. All electrons emitted from the cathode surface and passing through the cavity have a pitch factor smaller than α_{max}=2.63 (inverse MIG specific).

In order to suppress magnetically trapped electrons (item 2 and 3), all electrons from high electric field regions are gathered by the modulation anode and body (anode) as shown in Fig 3.8 and Ruess et al. [55]. Here, the modulation anode

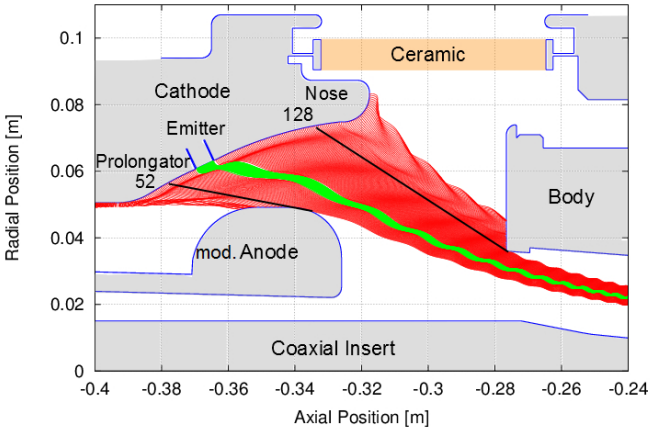

Figure 3.8: Trajectories of electrons emitted from the whole cathode structure (emitter electrons in green, possible secondary electrons in red) [55].

and body are located close to the main electron beam. Even more, the shape of the modulation anode and body reduces the electric field at the cathode prolongator and nose. A step forward in the MIG history is the advanced concave shaped cathode, which reduces further the electric field and suppresses the generation of a beam halo. This fundamental idea has been realized for the first time in MIGs. Due to the concave shape of the cathode the pitch factor of those secondary electrons (Fig. 3.9) at the cavity is smaller than $\alpha < 1.4$. In this case, the electrons emitted by the emitter have the highest pitch factor. This is a huge advantage in operation and was published in Ruess et al. [55] for the first time. Therefore, the inverse MIG satisfies the gun design criteria for the suppression of the trapped electrons [62].
The trajectories of possible electrons (main beam electrons and secondary electrons) emitted from the cathode surface are shown in Fig. 3.8 (emitter electrons in green, possible secondary electrons in red). The body and modulation anode were designed so that possible secondary electrons emitted from high electric field cathode regions are absorbed by them. Possible secondary electrons with an electron ID ≥ 128 in Fig. 3.8 are guided by the magnetic field lines towards the body, while electrons emitted from the cathode prolongator with an electron ID ≤ 52 are gathered by the modulation anode [55]. Here, secondary electrons which are emitted from the cathode surface close to the emitter ring

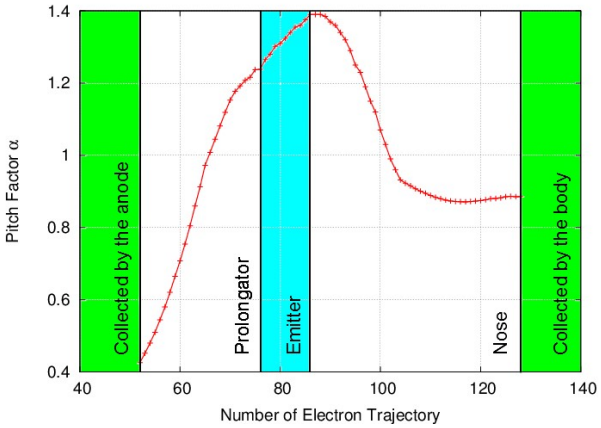

Figure 3.9: Pitch factor of the cathode electrons, simulated in the cavity center [55].

can pass the modulation anode and body towards the cavity and collector. The maximum permissible pitch factor which guarantees no magnetically trapped electrons is for the present inverse MIG design α_{max} = 2.63. The calculation of the maximum pitch factor is based on the equation presented in [62] and the assumption of an acceleration voltage U_{acc} = 90 kV, magnetic compression of b = 38.4 and an initial transverse kinetic energy of $E_{0,kin}$ = 10 eV.

Investigation of potential wells

In addition to the magnetically trapped electrons, electrons can also be trapped in a potential well. This effect is also described in Pagonakis et al. [62]. The simulation of the present inverse MIG has shown a potential well in the region close to the modulation anode with a depth of 10 kV, as shown in Fig. 3.10. This potential well can be avoided by reshaping the modulation anode in a way that the equipotential lines are parallel to the magnetic field lines, as it is shown in Fig. 3.11. By the optimized modulation anode shape the potential well can be significantly reduced to 60 V. However, by decreasing the depth of the potential well, the beam quality is decreasing significantly due to the modified modulation anode shape [55].

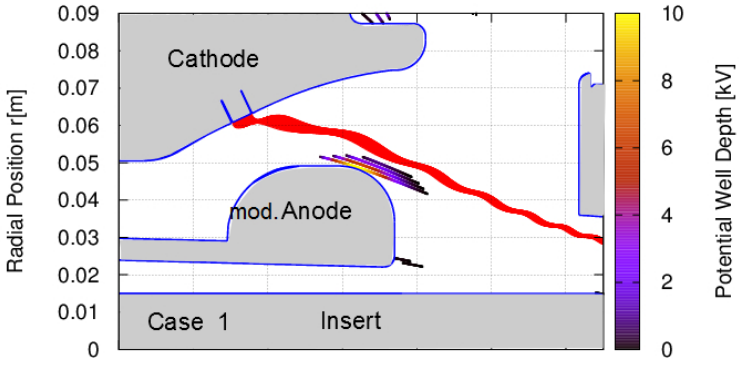

Figure 3.10: Investigation of potential wells in the inverse MIG with the nominal modulation anode design [55].

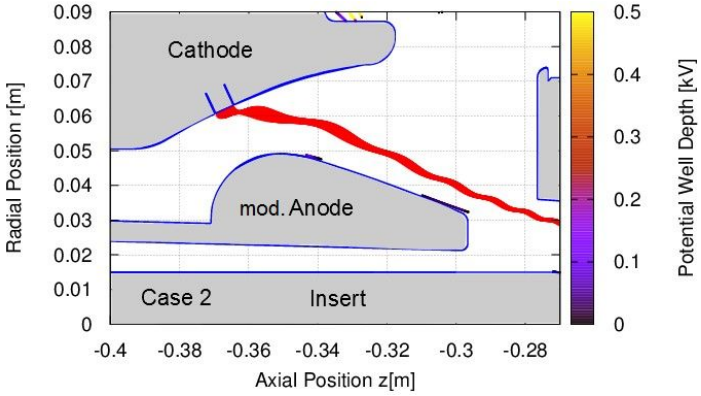

Figure 3.11: Inverse MIG with a modified modulation anode, which suppresses the potential well [55].

Operational margin

The beam parameters of the inverse MIG were optimized for a purely axial magnetic field at the emitter. However, modern MIGs are operating over a wide magnetic field angle margin at the emitter, which can be adjusted by the gun coils. Using this possibility the beam parameters α and $\delta\beta_t$ can be varied. The operational range of the inverse MIG is between -4 and +4 degree in order to satisfy the limitations of the gun coil currents. For all simulated magnetic field conditions at the emitter, the beam radius in the cavity center remains at 10 mm. In the nominal case (0 degree) the pitch factor is 1.3 with a spread $\delta\beta_t$ of 2.4 % [55], as shown in Fig. 3.12. The pitch factor is increasing with increasing magnetic field angle up to a pitch factor of 1.35 at +4 deg [55]. The pitch factor variation is mainly influenced by the **E** x **B** variation [55]. The global minimum of the spread $\delta\beta_t$ is 1.5 % at an emitter angle of -3 deg. With decreasing spread $\delta\beta_t$ the electron beam quality is improved.

The full operational map for an electron beam radius in the cavity center between 9.8 mm and 11 mm is shown in Fig. 3.13. The pitch factor dependency regarding the magnetic field angle at the emitter is getting smaller with increasing beam radius in the cavity. This is mainly related to the shape of the beam-forming components and the distance between the electron beam and the MIG components. It can be seen, that there are many possible op-

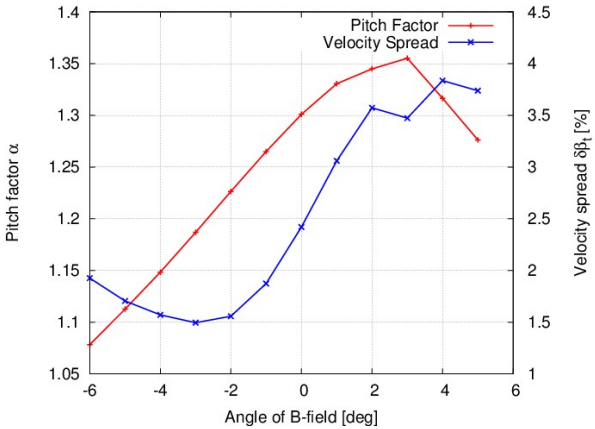

Figure 3.12: Pitch factor and velocity spread in case of a varying magnetic field line angle at the emitter region [55].

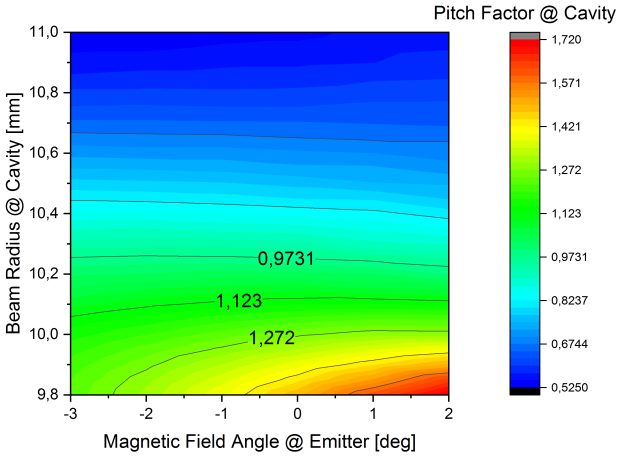

Figure 3.13: Map of the pitch factor distribution for different beam radius and magnetic field configurations.

erating points considering possible pitch factors between 1.2 and 1.4. This advantage is mainly related to the triode configuration and the flexibility of the superconducting coils. Furthermore, with the magnetic field angle the laminarity of the electron beam can be adjusted. In Fig. 3.14, the shape of the electron beam close to the emitter ring for a magnetic field angle smaller than 0 degree, equal 0 degree (nominal case) and larger 0 degree are plotted [55]. For negative beam angles the beam is of laminar type because the trajectories are not intersecting. In the nominal case quasi-laminar, while for > 0 degree the beam is non-laminar since the electron trajectories are intersecting each other [55]. It has to be mentioned that only the first 3 gyrations of the electron trajectories are investigated for the definition of the laminarity.

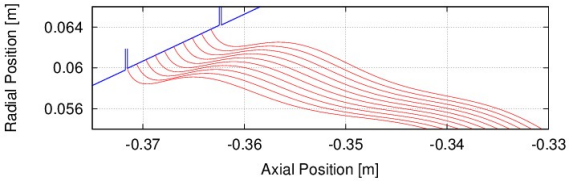

(a) Laminar Beam

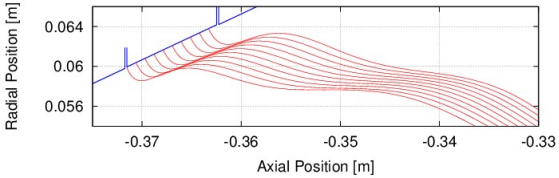

(b) Quasi-Laminar Beam

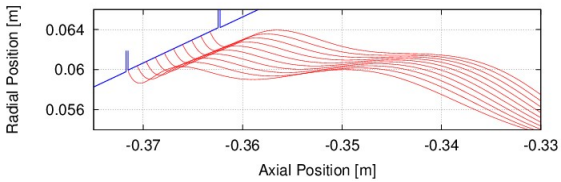

(c) Non-Laminar Beam

Figure 3.14: Beam trajectories at the emitter for different magnetic field configurations [55].

In addition, it has to be checked if in the operational magnetic field range possible trapped electrons can be excited. The pitch factor of possible secondary electrons for different magnetic field angles is shown in Fig. 3.15. In the nominal case (0 degree) the electrons which are emitted from the emitter indicate the highest pitch factor. However, operation at magnetic field angles of -6 deg, -3 and 5 deg have its maximum of the pitch factor distribution at the emitter neighboring regions. These electrons reach a pitch factor up to 2.2. However, all the sample electrons have a pitch factor which is smaller than the maximum safe pitch factor of $\alpha = 2.63$ [55] according to Pagonakis et al. [27]. The calculation of this maximum pitch factor is based on the assumption of an acceleration voltage $U_a = 90$ kV, magnetic compression of $b = 38.4$ and an initial transverse kinetic energy of $E_{0\varphi} = 10$ eV. Therefore, the inverse MIG satisfies the gun design criteria for suppression of the beam halo over the overall magnetic field margin [55].

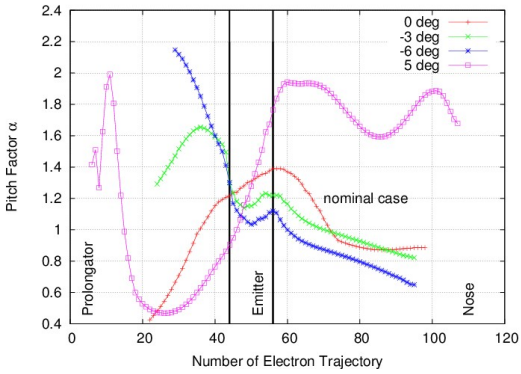

Figure 3.15: Pitch factor distribution of the cathode sample electrons for different magnetic field configurations from the cathode nose, emitter and prolongator [55].

3.2.3 Thermomechanical considerations

For an efficient gyrotron interaction the electron velocity spreads have to be minimized. A significant contribution to the misalignment is the thermal expansion of thermally loaded MIG components. Therefore, an advanced cooling

approach was developed for the inverse MIG, which leads to a 5 times lower temperature of the beamforming components compared to conventional MIGs. To compensate and to reduce the thermal expansion, advanced material compositions were simulated by the COMSOL program [68]. The final material composition can be seen in Fig. 3.16. The emitter is embedded in the cathode nose and prolongator. These components, as well as the modulation anode, are made of molybdenum. Molybdenum has a high work function of 4.16 eV, which avoid the unwanted electron emission from these regions. In addition, molybdenum has a high thermal conductivity of 138 W/mK with a small thermal expansion coefficient of $5.2\text{x}10^{-6}$ 1/K. To prevent a heat accumulation in the molybdenum components the connection parts are made of Copper Chrome Zirconium (CuCrZr). Therefore, the thermal heat can be efficiently transported to the isolation oil and the expansion of those components is minimal. For the inverse MIG it was decided to use CuCrZr instead of Copper. Usually, in all former MIG's oxygen free copper (OFHC) was the most preferable material instead of a copper alloy. CuCrZr exhibits an excellent heat conductivity of

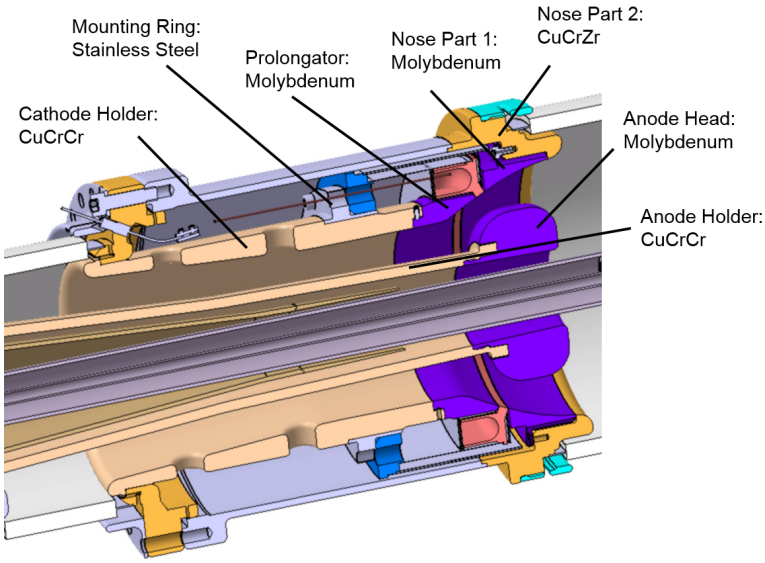

Figure 3.16: Material composition of the inverse MIG, optimized for lowest heat loading.

394 W/(mK) and a tensile strength of 200 MPa. The advantage is that the tensile strength is by a factor of 2 higher compared to OFHC. Simultaneously, it keeps a similar heat conductivity compared to OFHC. In addition, CuCrCr is much easier to machine at the lathe [55].
The emitter unit is fixed on a mounting ring made of stainless steel. Due to the low thermal conductivity of stainless steel, the heat of the emitter is accumulated in the emitter, which results in a lower heating power of the emitter.
Based on the material composition, the temperature and the resulting displacement and expansion of the inverse MIG design could be significantly reduced and verified in the simulations. The assumptions of the simulation are a cooling oil flow of 30 l/min between the inverse MIG and the inner wall of the superconducting magnet with an inlet temperature of 25 °C. The simulated temperatures (as shown in Fig. 3.17) and resulting thermal expansion of the critical gun regions (marked with P1-P3 in Fig. 3.18) are presented in Tab. 3.5 and Tab. 3.6. It can be seen that the regions close to the emitter have a maximum temperature of 126 °C, which corresponds to a thermal expansion of 162 µm in z-direction and 14 µm in r-direction [69]. The modulation anode of the inverse MIG is located directly opposite of the emitter and is heated up by thermal radiation. The simulated modulation anode temperature is $T = 41.6\,^{\circ}\mathrm{C}$ with a radial expansion of $\delta r = 3$ µm, see Ruess et al. [69]. The reason for the small thermal expansion is the use of materials with a high thermal conductivity (CuCrZr) and low thermal expansion coefficient (Molybdenum) and therefore the prevention of heat accumulation. In addition, the heat loading can be directly guided to the isolation oil, which is related to the fact that the cathode is positioned at the outside. Therefore, the proposed new inverse MIG has a significantly lower temperature and thermal expansion of the beam-forming components.

Table 3.5: Thermal expansion of the cathode nose, cathode prolongator and modulation anode at an emitter temperature of 1000 °C [69].

Component	Expansion Δr [μm]	Expansion Δz [μm]
Cathode Nose (P1)	17	-5
Cathode Prolongator (P2)	14	126
Modulation Anode (P3)	3	0.6

Table 3.6: Temperature of the main components [69].

Component	Temperature [°C]
Emitter	1000
Modulation Anode	41.6
Cathode Prolongator	110.9

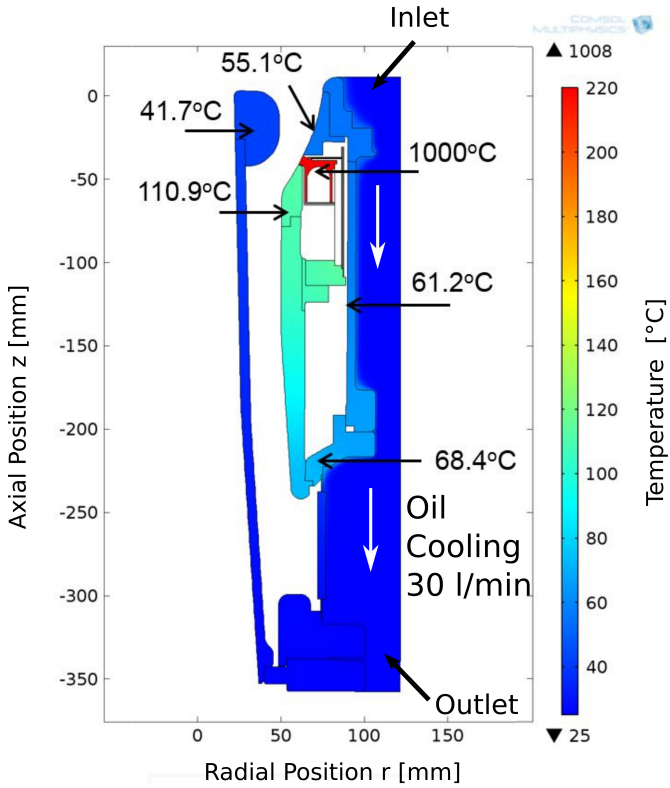

Figure 3.17: Thermomechanical simulation of the new Inverse Magnetron Injection Gun [69].

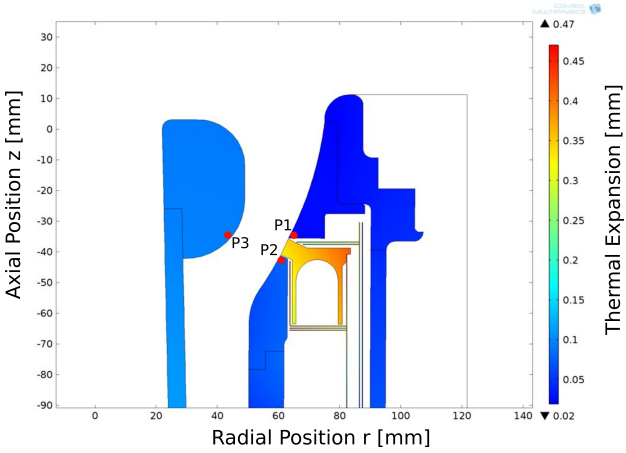

Figure 3.18: Displacement of the inverse MIG in the emitter region [69].

3.2.4 Technical design and tolerance analysis

The alignment and coaxiality of the modulation anode, the position in the borehole as well as the temperature distribution of the emitter has a significant influence on the position, the homogeneity and the nominal operation parameters of the electron beam, and therefore on the generated output power and efficiency. Following, the influence and suppression of the mechanical tolerances will be discussed and benchmarked by the help of the simulation tool ARIADNE [38]. For the first time, the maximum mechanical tolerances of the inverse MIG were investigated by a quasi 3D investigation approach.

Modulation anode alignment

The necessity for a high-quality electron beam is an azimuthal homogeneous electric field distribution at the emitter surface. Therefore, an aligned modulation anode is required in the MIG. An important design parameter for the inverse MIG implementation is the maximum allowable misalignment of the modulation anode in order to satisfy the gun design criteria. The maximum allowable misalignment of the modulation anode was estimated by the perfor-

mance of MIG simulations with the help of the in-house electron beam optics code ARIADNE [38]. In the following described investigations, the cathode and insert are assumed to be perfectly aligned in axial and radial direction. Only the modulation anode is shifted in radial direction. Considered is the axial position from -0.45 m to -0.32 m.
During the simulation there was no full 3D beam optics code available to simulate radial misalignment of the modulation anode. Therefore, a transformation of a 2D into 3D model was performed in Ruess et al. [70] (as shown in Fig. 3.19) for the very first time. For better clarity the insert was removed in the 3D model as shown in Fig. 3.19. For the transformation, the following analytical approach was performed: $d(\varphi)$ describes the distance between the cathode and the anode as a function of the azimuthal position φ [70], while Δx describes the misalignment of the modulation anode, as shown in Fig. 3.19. The radial misalignment Δx was shifted in a range of 0 to 500 µm [70]. For each misalignment Δx the corresponding pitch factor of 500 electrons was calculated in 2D. The distance $d(\varphi)$, as shown in Fig. 3.19, is a function of the azimuthal position φ and is defined as [70]:

$$d(\varphi) \approx \Delta r + \Delta x \cdot \cos\varphi \tag{3.1}$$

under the assumption of $\Delta x \ll \Delta r$, where Δr represents the difference between the emitter and modulation anode radius. The full 3D beam parameters can be calculated by the integration over the previously calculated pitch factor [70]:

$$F(\alpha) = \int_0^{2\pi} \alpha(d(\varphi))\, d\varphi \tag{3.2}$$

Based on the calculated distribution, the average pitch factor and spread of the 3D simulation can be derived [70]. The pitch factor distribution of a full 3D simulation is shown in Fig. 3.20 for a modulation anode misalignment of Δx = 300 µm. In the histogram Fig. 3.21(a) the pitch factor distribution for Δx = 0 µm (nominal case) is shown. The pitch factor distribution extends from 1.18 to 1.48 [70]. The distribution is significantly increasing with increasing modulation anode misalignment Δx. For a modulation anode misalignment of Δx = 300 µm (Fig. 3.21(b)) and Δx = 500 µm (Fig. 3.21(c)) the lower limit is decreasing to 1.1 and 1.05, respectively. The upper limit is increasing to 1.68 and 1.82, respectively [70]. The average pitch factor is nearly independent to the misalignment. It can be seen from Fig. 3.21(d) that the average pitch factor

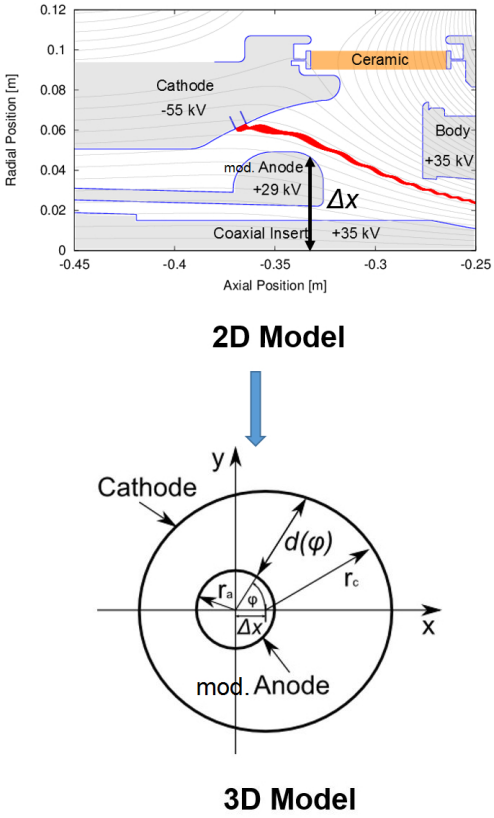

Figure 3.19: Transformation approach of the 2D into 3D model [70].

remains constant. However, the pitch factor spread is increasing from 6 % up to 10 % for a misalignment of $\Delta x = 500$ µm [70]. Based on that simulation results the maximum modulation anode deviation should be less than $\Delta x = 300$ µm in order to keep the α spread at low level and avoid the possibility of magnetically trapped electrons. The presented tolerance analysis was considered during the designing and manufacturing phase. Under the consideration of a high quality electron beam the pitch factor spread should not exceed 8 %. Therefore, it is recommended to keep the modulation anode misalignment below 300 µm.

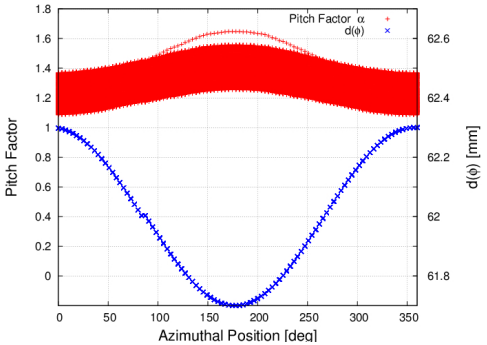

Figure 3.20: Pitch factor distribution and modulation anode misalignment versus the azimuthal position [70].

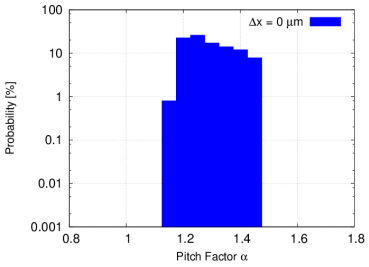

(a) Mod. anode misalignment of Δx = 0 µm

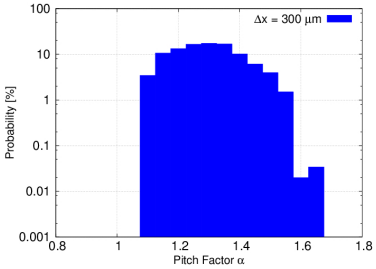

(b) Mod. anode misalignment of Δx = 300 µm

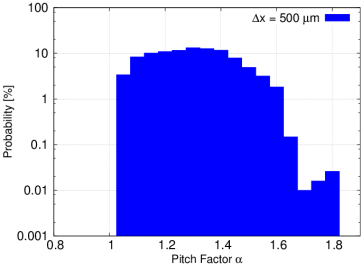

(c) Mod. anode misalignment of Δx = 500 µm

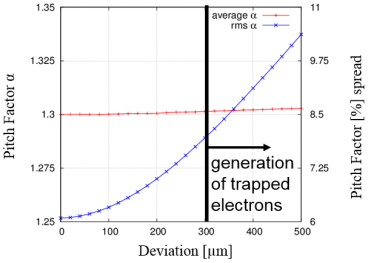

(d) Summary of all simulated modulation anode misalignments

Figure 3.21: Modulation anode misalignment of (a) 0 µm, (b) 300 µm, (c) 500 µm, and (d) average pitch factor and spread of the full simulation range [70].

Thermal emitter expansion

The uncertainty of the radial emitter expansion contributes also to the electron beam quality. Therefore, the radial emitter deviation in the range of ± 150 µm were investigated [70]. The definition of the sign is shown in Fig. 3.22. A radial emitter deviation causes [65]:

1. A deviation of the mean pitch factor.
2. An increasing pitch factor of electrons emitted from the rims of the emitter.

In the nominal case the emitter is -70 µm embedded in the cathode. In this case the average pitch factor is 1.3 with a global minimum spread of $\Delta\alpha$ = 6.5 %, as shown in Fig. 3.23. With a negative radial misalignment of Δd_e = -150 µm the average pitch factor is decreasing to a value of α = 1.08. For a misalignment of Δd_e = + 150 µm the pitch factor α is increasing to α = 1.58 with a spread of $\Delta\alpha$ = 15.5 %. It can be seen, that pitch factor is linearly increasing to positive misalignment, which is related to the increasing electric field.

In particular, the investigation of each emitted electron from the emitter is shown in Fig. 3.24. For a misalignment of Δd_e = +105 µm the electrons

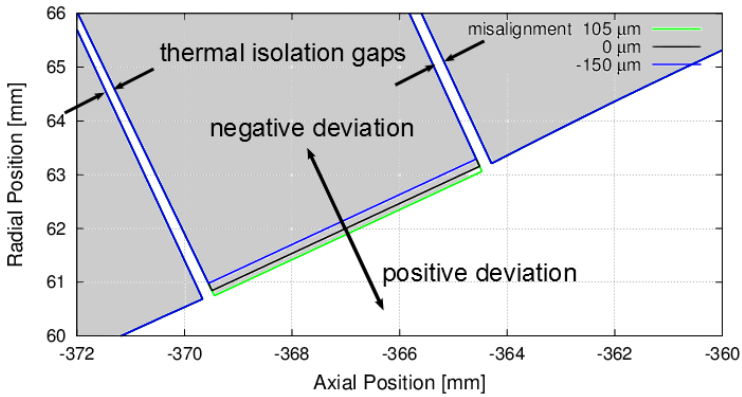

Figure 3.22: Definition of the emitter deviation and representation of the thermal isolation gap [70].

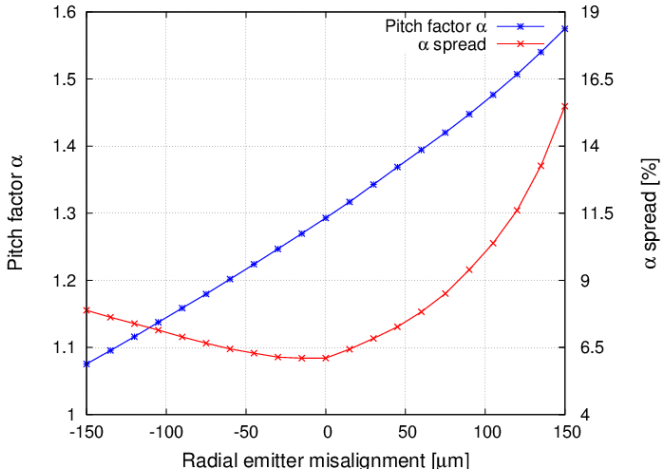

Figure 3.23: Pitch factor and spread for different radial emitter deviations [70].

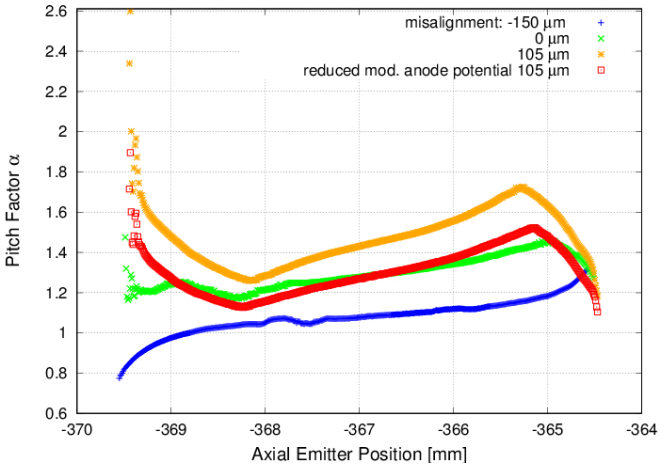

Figure 3.24: Pitch factor in the cavity as a function of the emitting point along the emitter surface for different radial misalignments.

reach a pitch factor of α = 2.6, which have the possibility to be magnetically trapped [70]. These electrons are emitted from the rear edges of the emitter. For negative deviations the pitch factor of the electrons emitted from the edges is decreasing. This effect is related to the strong variation of the electric field at the emitter rear edge. Due to the fact, that the inverse MIG is of triode type, the edge effect [65] can be reduced by changing the potential of the modulation anode. Assuming a mean pitch factor of 1.3 and a radial emitter deviation of 105 µm, the modulation anode potential has to be reduced from 29 kV (nominal case) to 26.5 kV [70]. The maximum pitch factor of the electrons emitted from the emitter rear part can be reduced from 2.6 to 1.9 [70].
It can be summarized, that due to the triode configuration in the present inverse MIG design, a deviation of the emitter can be much easier compensated compared to conventional MIGs used in today's fusion gyrotrons. In addition, an effective reduction of the emitter sensitivity regarding radial deviation can be achieved by the implementation of an anti-emission coating of the emitter edges.

Temperature homogeneity at the emitter surface

An inhomogeneous electron beam depends mainly on the homogeneity of

1. The surface roughness.
2. The BaO-layer thickness.
3. The electric field distribution.
4. The temperature distribution of the emitter.

These inhomogeneities increase the velocity spread and non-uniformity of the hollow electron beam. Quantitatively the electron beam quality can be analyzed by measuring the Current-Voltage characteristics, see Zhang [45]. Here, the transition between the space charge limited and temperature limited region gives an insight regarding the electron beam homogeneity. The main contribution to an inhomogeneous electron beam is a non-uniform temperature distribution [70].
The measurement of the inverse emitter at nominal operating surface temper-

ature (1000 °C) shows a temperature distribution of ± 7 °C. The temperature deviation is 46 % less compared to currently used MIGs in fusion gyrotrons, which was already presented in Ruess et al. [71]. The small deviation is related to the advanced potting of the emitter, which is exclusively implemented in emitters delivered from the manufacturer Ceradyne. Considering the temperature inhomogeneity of ± 7 °C the pitch factor spread is increasing from $\Delta\alpha$ = 6.5 % up to $\Delta\alpha$ = 6.7 % [70]. In Fig. 3.25 it can be seen that the average pitch factor remains constant with increasing temperature deviation, while the spread is increasing up to 10 % for a temperature deviation of $\Delta T = \pm 27$ K [70]. The investigations in Fig. 3.26 show the dependency between kinetic energy and the azimuthal temperature deviation. The kinetic energy of the simulated electrons is plotted for a deviation of $\Delta T_e = 0$ °C (red colored) and $\Delta T_e = \pm 7$ °C (nominal case, blue colored). At regions with higher emitter temperature, more electrons will be emitted, which results in an increasing space charge cloud [70]. Here the resultant electric field is decreasing. Consequently, the kinetic energy is lower in regions of high space charge and vice versa. As a result, the maximum decelerating voltage of the depressed collector has to be reduced to the energy of the slowest electron, which reduces the overall gyrotron efficiency [70].

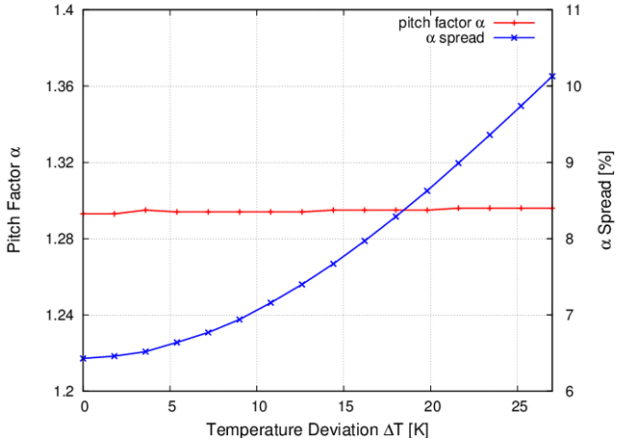

Figure 3.25: Pitch factor and spread for different temperature deviations of the emitter [70].

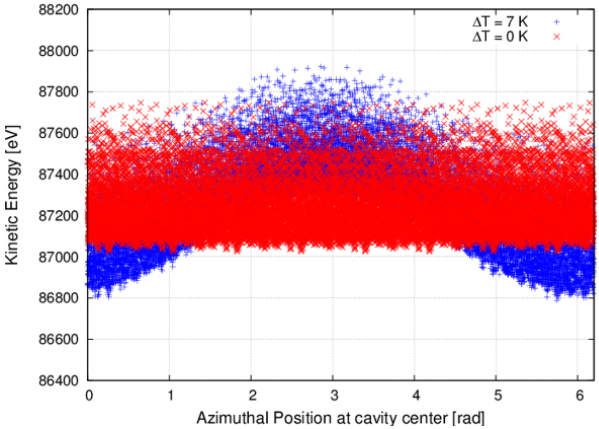

Figure 3.26: Kinetic energy as a function of the azimuthal position in the cavity center for a temperature deviation of 7 K (blue points) and 0 K (red points) [70].

3.2.5 Design for manufacturing

Compared to the W7-X and ITER gyrotron MIGs, where the ceramics are on the face side brazed, the inverse MIG is using, for the first time, the improved peripheral brazing (see Fig. 3.27). Experimental investigations have shown that tolerances in the braze point at the ceramics add a significant offset. The advantages of the peripheral brazing are a much simpler alignment of the flanges and a better absorption of torsion forces during the post-processing. As a result, the post processing after the brazing and welding of the MIG is much easier and, in addition, the risk of damages at the ceramic during the post processing is significantly reduced. However, the electric field at the edge of the flange is increasing. Therefore, corona rings, as shown in Fig. 3.6 and Fig. 3.16, are implemented which reduces the electric field significantly. The remaining electric field at the corona ring is 42 kV/cm.

The designed inverse MIG is a complete modular electron gun. The advantage is that in the present gun different material compositions as well as different types of future high current density emitters for DEMO gyrotrons can be tested. The inverse MIG consists of 5 assemblies, as shown in Fig. 3.28. Each assembly is one unit and was finally post processed after the brazing and welding procedure. As a result, all components have a satisfactory concentricity and all

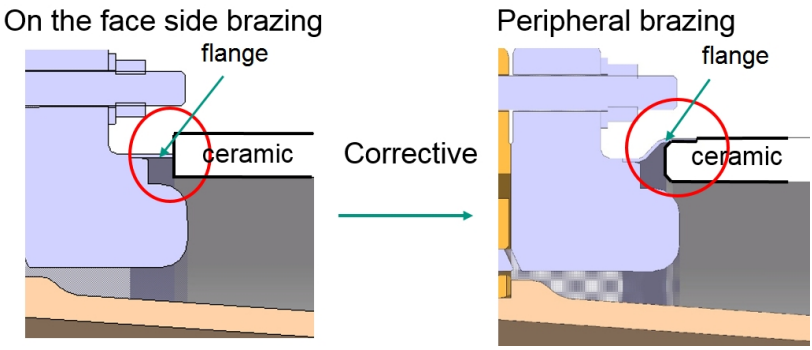

Figure 3.27: Optimized design of the ceramic flanges.

the deviations are within the requirements. In addition, this modular approach offers the possibility for an in-house and cost-efficient manufacturing process.

3.2.6 Evaluation of the emitter temperature homogeneity

The first thermal test of the inverse emitter (Fig. 3.29) has shown an excellent performance. The temperature deviation at a nominal temperature of 1000 °C is ± 7 °C, which is smaller compared to the currently used conventional emitters (± 15 °C). The small temperature deviation is related to the improved 4 layer potting procedure. At nominal operation, the filament current is 24 A with a corresponding heating power of 990 W. The emitter temperature inhomogeneity has a significant influence on the electron beam quality and consequently on the gyrotron efficiency. The temperature distribution of the emitter can be measured by the help of an infrared camera. For the measurement, the cathode can be used as a vacuum chamber as shown in Fig. 3.30. On the top, the cathode is closed by a ZnS window, while at the bottom, the cathode is closed with a flange and an intake socket for vacuum pumping. This measurement can be used as a calibration of the filament current versus the emitter temperature.

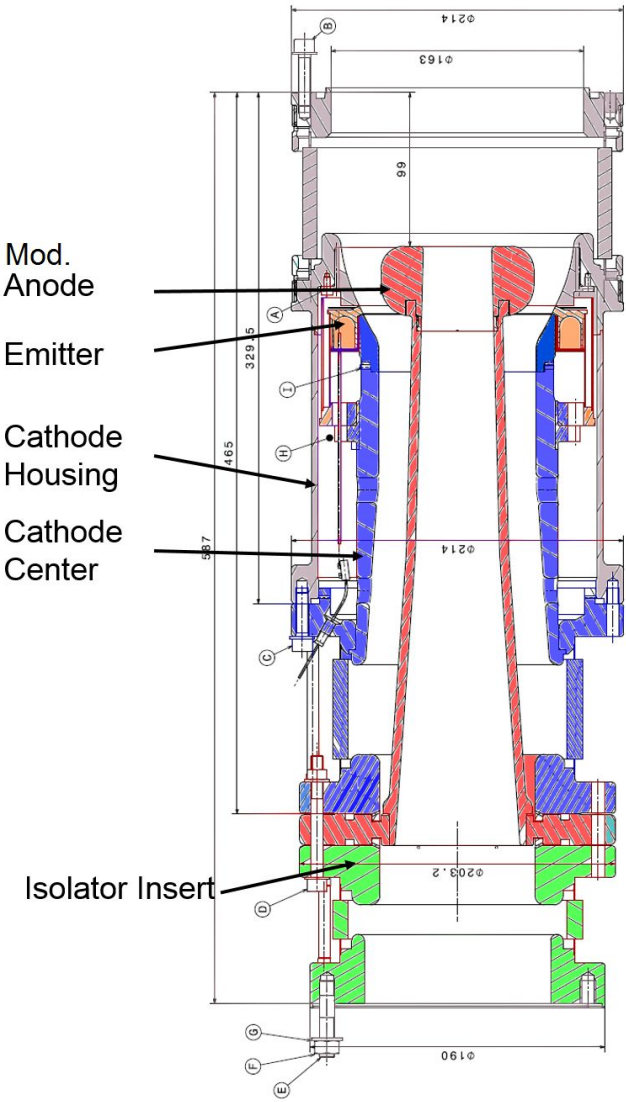

Figure 3.28: Sub-assemblies of the Inverse Magnetron Injection Gun approach.

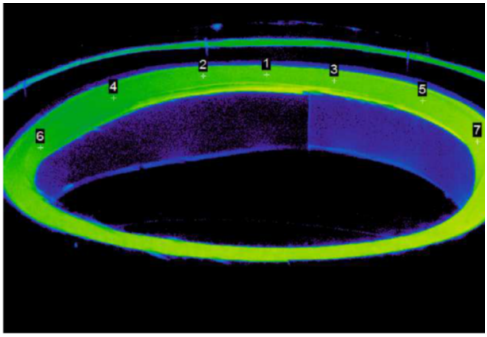

Figure 3.29: Temperature distribution of the emitter, measured with an infrared camera.

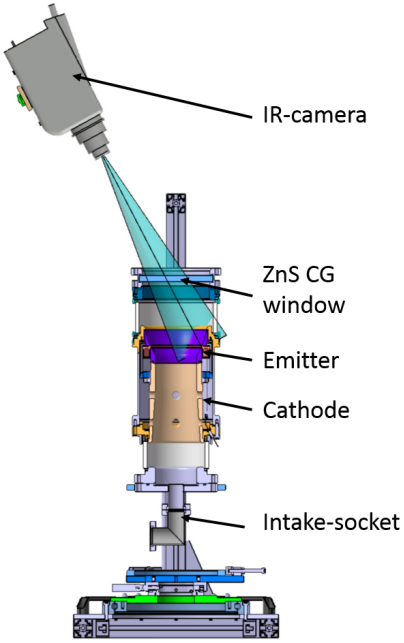

Figure 3.30: Cross-section of the thermal test stand for the evaluation of the temperature distribution of the emitter.

3.3 Towards ultra-compact inverse magnetron injection gun

A significant cost factor in European gyrotron set-ups is the large diameter of the MIGs and the associated high costs of the superconducting magnets. Therefore, in the following section, an inverse MIG with a 25 % smaller outer diameter will be presented. For this investigation the boundary conditions are:

1. Average pitch factor α of 1.3.
2. Real magnetic field configuration and coil current of the KIT superconducting magnet.
3. Current density <5.5 A/cm^2, which is the limit for a reasonable emitter life-time.

The starting point is the inverse MIG designed for the KIT 2 MW 170 GHz coaxial-cavity gyrotron. In this design the emitter radius is 62 mm with an electron beam radius in the cavity of 10.0 mm. Here, the maximum electric field strength is 75 kV/cm (as shown in Fig. 3.31), which is below the limitation

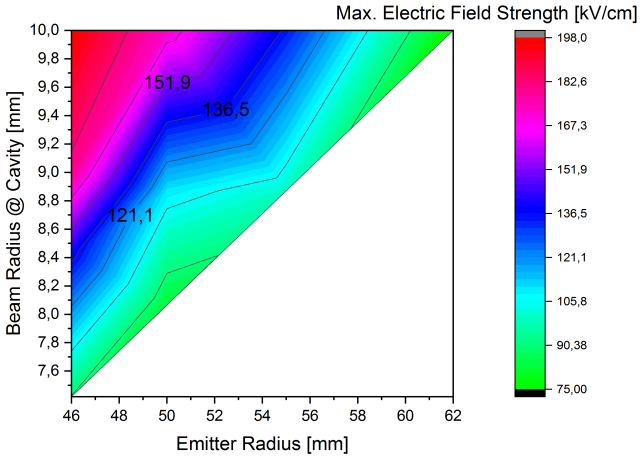

Figure 3.31: Systematic analysis of the beam radius versus the emitter radius with respect to the maximum electric field strength in the Magnetron Injection region.

of <100 kV/cm. By keeping the beam radius in the cavity constant and reducing the emitter radius, the magnetic compression is decreasing which is resulting in a lower pitch factor. In order to satisfy the requirement of an average pitch factor of 1.3 the tangential electron velocity component and therefore the electric field at the emitter has to be increased. Under consideration of the maximum electric field strength, the minimum emitter radius is 57 mm, if the nominal cavity beam radius of 10.0 mm for the $TE_{34,19}$ mode will be kept. The systematic investigation results in Fig. 3.31 show clearly, if the emitter, hence the gyrotron, is getting significantly smaller in diameter, the beam radius in the cavity has to be reduced under the consideration of the maximum electric field strength limitation. The systematic simulation show, that a very promising and compact design can be achieved with an emitter radius of 46 mm. The corresponding beam radius in the cavity is 7.42 mm. Due to the reduction of the emitter radius the current density is increasing up to 5.3 A/cm^2, which can be handled with the current emitter technology. However, an operation with the current $TE_{34,19}$ mode is not possible anymore. Therefore, a numerical study of very-high order volume modes compatible for the ultra-compact inverse MIG have to be done. These investigations, presented in Fig. 3.32 and published in Ruess et al. [72], have shown that a very promising mode is the $TE_{25,22}$. The eigenvalue of the $TE_{25,22}$ is 102.45, which is close to the eigenvalue of the $TE_{34,19}$. The outer radius of the cavity for an operation at 170 GHz is 28.40 mm with a maximum wall loading of 2.0 kW/cm^2, presented in Fig. 3.33. The corresponding insert radius for an efficient suppression of unwanted neighboring modes is 5.65 mm. This radius is the best trade of between mode purity and cooling capabilities. The wall loading, as shown in Fig. 3.33, of the insert is 0.11 kW/cm^2. Thermomechanical simulations have shown that during CW operation the maximum insert surface temperature reaches 83 °C with a water flow rate of 5.89 m/s [73]. The soft excitation point of the $TE_{25,22}$ can be excited at a beam voltage of 90 kV and a beam current of 75 A, as shown in Fig. 3.32. The calculated maximum output power is 2.5 MW with an electronic efficiency of 37 %, which is similar to the conditions of the $TE_{34,19}$.

With the combination of the ultra-compact inverse MIG and the new developed $TE_{25,22}$ operational mode the gyrotron diameter in the borehole can be reduced by 25 %. As a result, the bore hole diameter of the superconducting magnet can be also reduced from currently 246 mm by 25 %, which leads to a significant cost reduction.

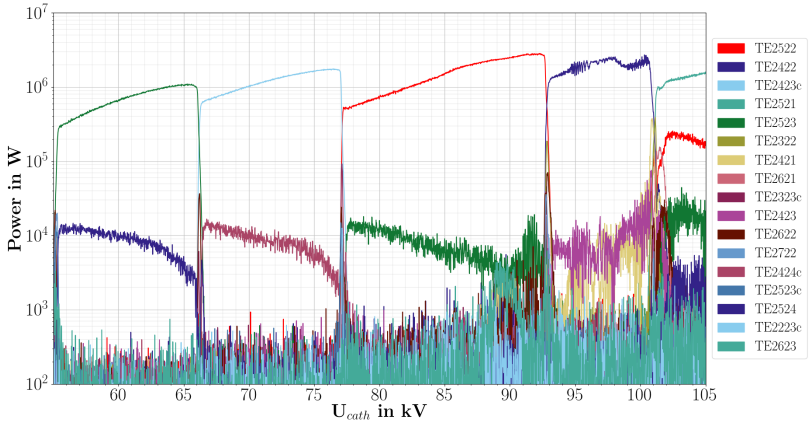

Figure 3.32: Adiabatic start-up scenario at 6.86 T and a beam current of 75 A.

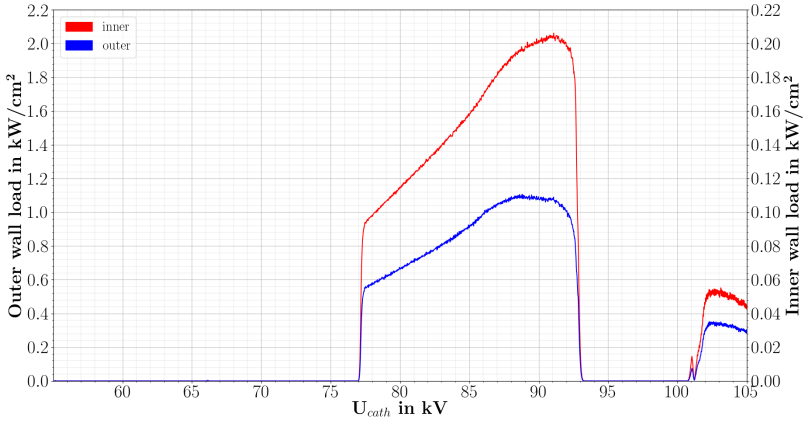

Figure 3.33: Wall loading of the outer wall (red) and of the insert (blue).

3.4 Summary

Reaching the long-pulse operation regime an advanced Magnetron Injection Gun is required. Therefore, a conventional coaxial-cavity MIG with coated emitter rims in triode configuration was presented. Due to the complex operation of a triode, a diode for industrial applications was developed in this chapter. The development of a novel diode structure makes it possible for the first time to comply with all gun design criteria.
However, if a higher output power or longer lifetime is required, the implementation of a larger emitter is necessary. This requirement can not be met with the conventional MIG approach. Therefore, in frame of this work, an advanced compact inverse MIG was developed. The compact approach allows the installation of a 16.8 % larger emitter. In addition, due to the outside positioned cathode and the use of advanced materials, a significantly better cooling efficiency could be achieved which leads to a 5 times lower cathode-temperature compared to conventional MIGs. Furthermore, the simulations carried out for the first time, have strengthened the thermo-mechanical understanding. In addition, with the concave shaped cathode the suppression of magnetically trapped electrons can be much easier realized. For the first time, the maximum tolerances of the inverse MIG components are numerically investigated by an advanced transformation, which considers the full 3D geometry. In addition, fundamental manufacturing techniques and welding procedures were improved for the in-house manufacturing of the inverse MIG. Based on the gained manufacturing know-how, it is now possible to built-up cost-efficient MIG prototypes for the DEMO project in-house.

4 Advanced joining technologies for long-pulse operation

Mandatory for a successful DEMO gyrotron development is the manufacturing and testing of prototypes. However, this is only possible if the prototypes can be inexpensively manufactured in-house. A significant cost driver is the brazing and welding of vacuum-compatible components. Therefore, in this chapter, a suitable soldering and welding procedure will be presented. The goal is to develop a process that is vacuum compatible, cost effective and compatible with the KIT internal facilities. In order to satisfy the vacuum condition, a vacuum leakage rate of $< 5x10^{-9}$ mbar l/s is required, see Dammertz [74]. In addition, the new brazing technology has to withstand bake-out temperatures up to 500 °C. It depends on the vacuum tightness, the temperature stability, the mechanical strength and the corrosion resistance of the connection joints. Therefore, it is necessary to select a suitable bonding method for the respective application.

4.1 Preliminary investigations

During the welding procedure the materials at the joint are locally heated up above the melting point of the particular material. Due to the thermal conductivity of the materials, the component itself is heated up. This creates the risk, that the temperature in pre-brazed connections is reaching the maximum allowable temperature. Such a case exists, for example, when the isolation ceramic is welded to the flange, as shown in Fig. 3.27. Here, the thin connecting flange is first brazed to the ceramic and then welded to the main flange, as shown in Fig. 4.1. Therefore, the welding procedure was simulated with the multi-physics simulation tool COMSOL. The simulation results show, that with an acceleration voltage of 60 kV and an electron beam current of 5 mA and 16 mA (nominal welding parameters) the maximum temperature at the brazed joint

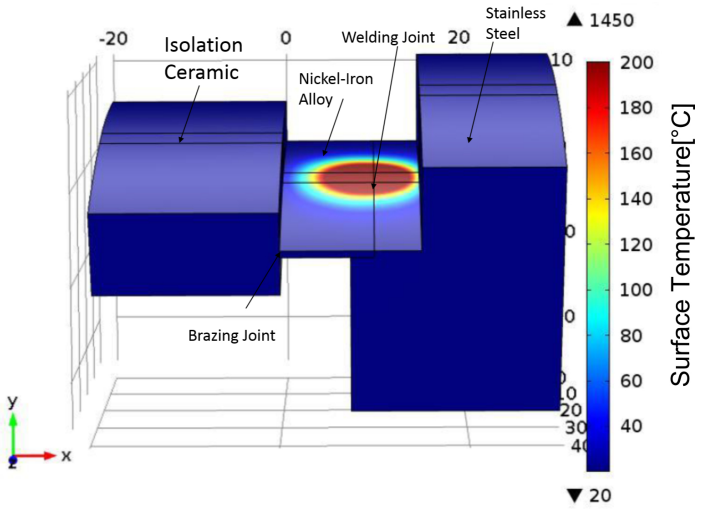

Figure 4.1: Temperature distribution during the electron beam welding process of nickel-iron alloy and stainless steel.

is smaller than 60 °C. However, the welding point is heated up above the melting temperature of the materials, as shown in Fig. 4.1 and Fig. 4.2. The high temperature gradient is related to the small thermal conductivity of the nickel-iron alloy, which is a well suitable material for such applications. The reason for the higher beam current for a successful welding of the nickel alloy with CuCrZr can be seen when comparing Fig. 4.1 with Fig. 4.2. In Fig. 4.2 the CuCrZr flange achieves a temperature of 160 °C, while the stainless steel flange, as shown in Fig. 4.1, remains at ambient temperature. Because of the heat loss at the welding joint, the current has to be increased up to 16 mA. Here, the increasing beam current and high penetrating energy causes a growth of the CuCrZr grains. The larger grains are a considerable threat for vacuum leaks. In this work, the issue could be solved using of forged CuCrZr with originally smaller grains. It has to be figured out, that the significant knowledge gain in the electron beam welding procedure and selection of suitable materials opens the path for a cost-efficient and in-house manufacturing of key components for the gyrotron.

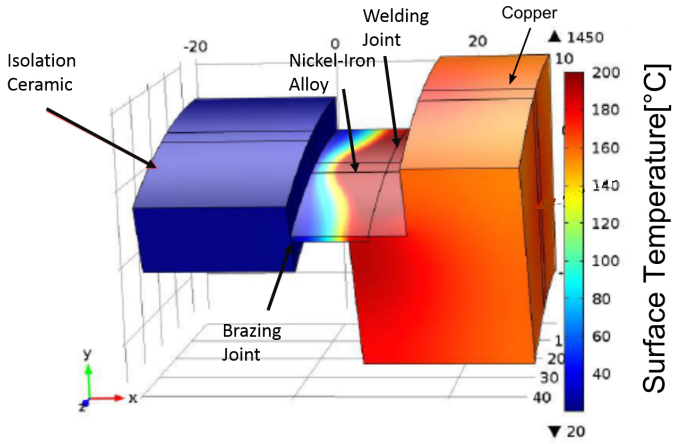

Figure 4.2: Temperature distribution during the electron beam welding process of nickel-iron alloy and copper.

4.2 Electron beam welding techniques

Electron beam welding (EBW) is a suitable method for vacuum tube applications because the heat input and therefore the heat expansion of the component is very low, as stated in Schultz [75]. The kinetic energy of an electron beam is transformed into heat during contact with the material. Dithley proposes in [76], that the electrons should be focused to a beam with a diameter at the incidence of 0.1 to 0.3 mm with a power density of 10^7 W/mm^2. For best possible results the electron beam welding process should be conducted in vacuum [77]. The main advantages of the described procedure are [75]:

- small heat input,
- almost complete absorption of the beam energy,
- small deformation of the component,
- copper or copper alloy and stainless steel connections weldable.

Because of the listed advantages the EBW process was used for the Inverse Magnetron Injection Gun, mainly for the connections between the flanges and the thin connection flanges of the ceramic which consists of a nickel-iron low expansion alloy and the connection between copper and stainless steel.
To get the correct electron beam parameters for a successful welding, tests have to be made in advance. Here, the welding beam current, acceleration voltage, welding speed and penetration depth are investigated. The most promising welding parameters for the different material compositions are listed in Tab. 4.1. The optimized parameters for a connection between nickel-alloy (material designation number: 1.3917) and stainless steel (1.4571) are a beam voltage of 60 keV, a beam current of 5 mA and a welding speed of 10 mm/s. For a reliable connection between nickel-alloy (1.3917) and CuCrZr the beam current has to be increased from 5 mA up to 16 mA, which is related to the higher heat transfer coefficient of CuCrZr compared to stainless steel.

Fig. 4.3 shows the grinding pattern and welded joints of the samples. It can be seen that in both material configurations the two materials are merged in the area of the melting bath, as shown in Fig. 4.3 (top row). Even more, the weld in Fig. 4.3 (bottom row) looks very homogeneous with and excellent seam surface.

4.3 High temperature vacuum brazing

In addition to the welding process the brazing offers an excellent joining technology. For components with high requirements regarding strength and operation temperature, the high temperature vacuum brazing is a well-suited process. By definition, the high temperature vacuum brazing takes place above

Table 4.1: Welding parameters for the connection between 1.3917 (nickel alloy) and 1.4571 (stainless steel) as well as 1.3917 and CuCrZr.

Connection	Beam Voltage [keV]	Beam Current [mA]	Welding Speed [mm/s]
Nickel Alloy - Stain. Steel	60	5	10
Nickel Alloy - CuCrZr	60	16	10

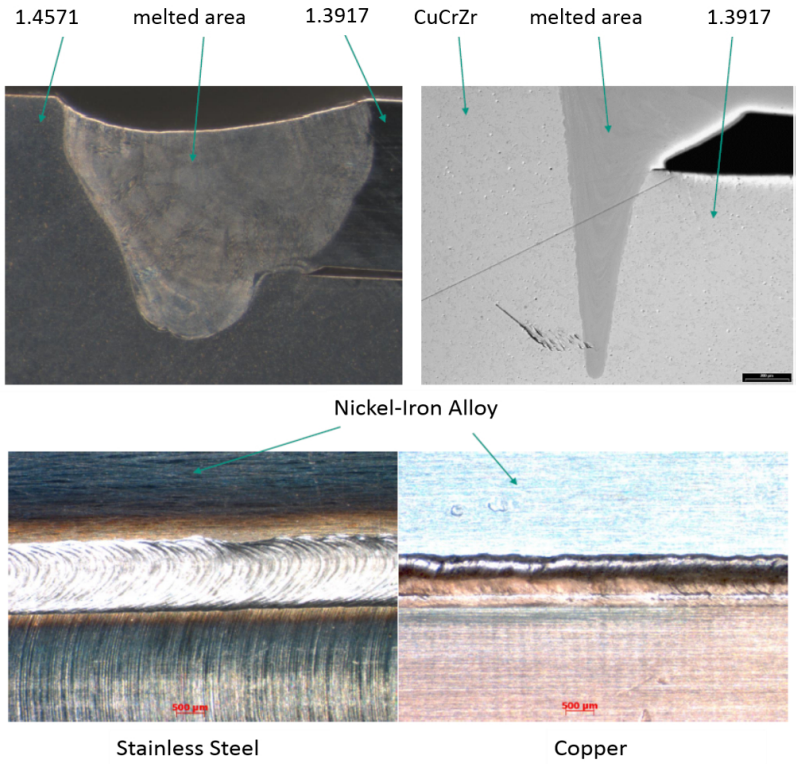

Figure 4.3: Grinding pattern of electron beam welded connections. Left side: Connection of copper and nickel-iron alloy. Right side: Connection of Stainless steel with nickel-iron.

900 °C. During the brazing process the vacuum acts as a soldering flux and in parallel as a protection atmosphere to prevent oxidation of the components. A further advantage of the high temperature vacuum brazing is that components with several soldering joints can be brazed in parallel and with the same quality, even with different material compositions. A detailed overview in brazing technologies is given in Kowalewski et al. [78].

Further advantages are [78]:

- Homogeneous heat input up to the brazing temperature and therefore less deformation.
- Less tension in the component because all joints will be brazed simultaneously.
- Brazing of inaccessible joints.

Requirements for Brazing Joints

The main quality characteristics of brazing joints are homogeneous molten mass, no inclusion of residual gases and a leakage rate $< 5x10^{-9}$ mbar l/s. To achieve the desired requirements the following main conditions have to be fulfilled [78]:

- The parts must be protected from atmosphere during the heating process to prevent oxidation,
- the gap clearance of the parts must be designed to assure capillary attraction,
- the pressure in the brazing furnace has to be $\leq 10^{-5}$ mbar.

Construction to achieve optimum brazing conditions

Braze joint clearance has a significant effect on mechanical properties of the brazing joint [79]. The clearance is the distance between the surfaces of the joint at brazing temperature. For brazing with silver, gold, copper and nickel the clearance should be between 10 µm to 100 µm at the brazing temperature [78]. In the present work it was found out, that a clearance width of 50 µm is the best compromise between the mechanical strength and manageability in the assembly of the press fits. For < 50 µm the components cannot be assembled with the available tools and a homogeneous clearance cannot be guaranteed. The grinding pattern of the brazing probes can be seen in Fig. 4.4. With different metals, the one with the highest expansion coefficient may tend to increase or

decrease the clearance depending on relative positions and configurations of the joint. To solve the mentioned problem stainless-steel and copper as well as Glidcop were used, which offer a similar thermal expansion coefficient and therefore homogeneous clearance and stresses over the complete temperature profile. When cooling down from the brazing temperature, stresses and strains could be avoided in the selected material composition. Therefore, after the brazing process the filled clearance is in the range between 48 and 51 µm (see Fig. 4.5), which shows the excellent and precise manufacturing process.

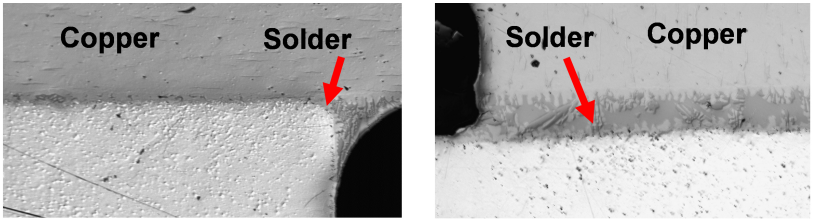

Figure 4.4: Grinding patterns of brazed joints.

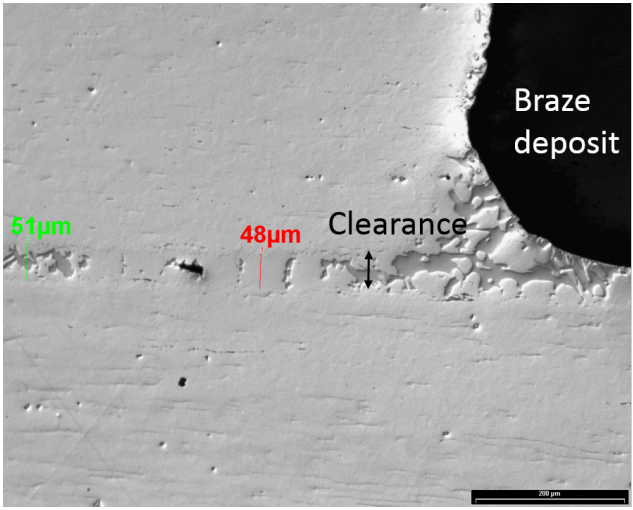

Figure 4.5: Grinding pattern of the brazed joint with the measurement of the clearance.

The most appropriate surface roughness for brazing is difficult to define. Surface roughness adds surface area to the joint, which provides countless extra capillary paths [78]. However, if the surface roughness is too high and a metal-to-metal press contact exists, the capillary forces are also shut off. This effect can be seen in the grinding pattern shown in Fig. 4.6. Here, the braze cannot penetrate into the clearance. Based on experiments, the best surface roughness for a stable and reliable brazing connection is Ra = 0.4.

4.3.1 Brazing procedure for the gyrotron components

For the very first time at KIT, gyrotron components were brazed with a nickel-base super alloy braze (Braze Tec D 897.1 [80]) instead of a silver or gold/copper braze, as it is used in industrial vacuum tubes. That braze offers the possibility of an easy handling without the necessity of a component assembly under vacuum conditions or the use of soldering flux for the reduction of oxide layers. In addition, the nickel-base super alloy braze is 98.8 %

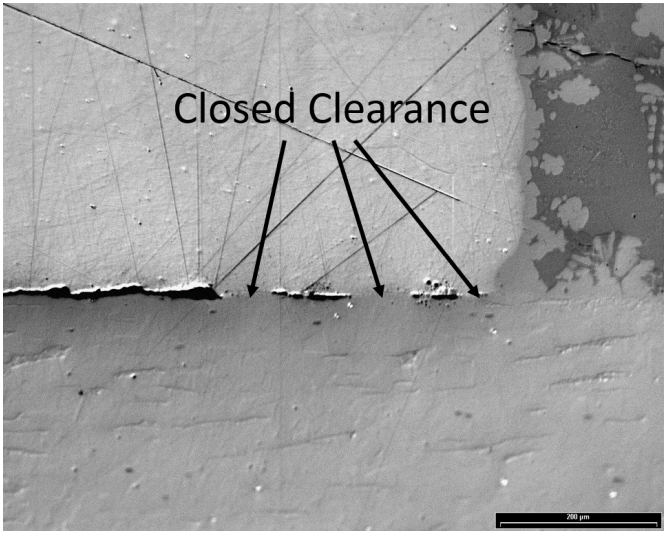

Figure 4.6: Grinding pattern of a brazing probe with a cutted clearance.

cheaper compared to a gold/copper braze, which had been used. The following brazing procedure, as shown in Fig. 4.7, was developed and optimized for the nickel-braze-super alloy braze. As a basis for the long-pulse components, the procedure described in [78] was used as a starting point:

Initial pump down: For copper and stainless steel a vacuum pressure of $\leq 10^{-6}$ mbar is sufficient.

Initial heating ramp: The initial ramp should be about 6 °C/minute. Faster rates are not recommended because thermal distortion could happen. In addition, with large components excessive outgassing will occur. During the initial heating ramp, roughly at 80 °C [78], the phosphor (P) of the nickel-base super alloy is outgassing and removes the oxide layer of the stainless-steel and copper surfaces in the furnace [78]. This is one of the major advantages of the nickel-base super alloy braze compared to the conventional brazes used for vacuum components.

Burn-Off: A burn off is recommended using a nickel-base super alloy braze. Here the outgassing phosphor, oxygen and other impurities can be pumped out.

Stabilizing Soak: Temperature shall be about 800 °C, however below melting temperature of the brazing mass. The temperature should be kept constant for

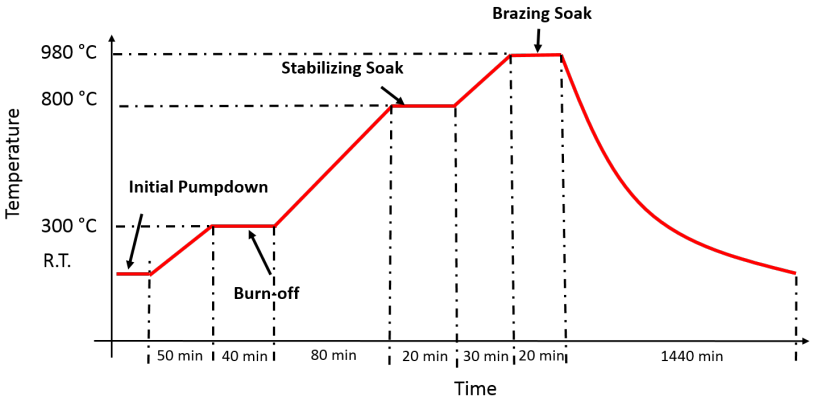

Figure 4.7: Braze cycle of the nickel-base super alloy brazing solder, which is used for the long-pulse coaxial gyrotron.

a duration of 15 min to 30 min. The main reasons for the stabilizing soak are [78]:

- It allows to equalize the temperature in the components. Therefore, all parts in the brazing furnace will reach brazing temperature at approximately the same time.
- It ensures a low enough vacuum pressure before ramping up to brazing temperature.

Heating Ramp to Brazing Temperature: The rate has to be fast enough to avoid liquidation of the brazing and erosion of the gyrotron components. For the long-pulse components the heating ramp was 6 °C/minute [78] because the oven cannot drive a faster heating ramp.

Brazing Temperature: It is preferable to use the lowest brazing temperature within the required brazing range. For the used nickel-based supper alloy brazing the brazing temperature is 980 °C, which is well below the melting temperature of copper (1085 °C) [81].

Brazing Soak: The time at brazing temperature should be long enough in order to guarantee that all parts within the component reach the required brazing temperature. In the present work the optimum brazing temperature is 980 °C for a duration of 10 min [78].

Cooling From Brazing Temperature: To avoid stresses, it is recommended that the components are vacuum cooled from brazing temperature. In case of hardening the furnace can the flooded by nitrogen. In case of the gyrotron components the temperature was slowly reduced which is related to the procedure of the used vacuum oven at KIT.

4.3.2 Investigation of material properties after brazing

The temperature of the performed brazing is 980 °C which is close to the melting temperature of copper. At the brazing temperature of 980 °C the grains in the copper increase their size significantly and the yield strengths are decreasing. Therefore, the risk of a deformation of the pre-prototype copper components, cavity and launcher, exist and the yield strength after the brazing

procedure has to be investigated. The components which are connected below the cavity are the beam tunnel and the MIG. The total weight of both components is ~ 60 kg. Therefore, the yield strength which has to be considered is 600 N.

The yield strength of OFHC copper at a deformation of 0.2 % is 139.13 N/mm^2 before brazing and afterward it is decreasing to 25.45 N/mm^2, as shown in Fig. 4.8. The cavity has a minimum cross section area of 383 mm^2, which corresponds to a yield strength (OFHC copper) of 9754 N. The minimum cross section of the launcher is 2356 mm^2 with a maximum yield strength of 59965 N (OFHC). The maximum acceptable load is 325 kg for the cavity and 1998 kg for the launcher considering a safety factor of 3. As a result, the OFHC copper can be used for the launcher and the cavity. However, it has to be mentioned that the test results are based on only one heat cycle. However, during the gyrotron operation the OFHC is getting softer.

In addition, the tensile test of Glidcop Al-15 [82] has shown that the yield strength with a deformation of 0.2 % is before the brazing Rp0.2 = 306.45 N/mm^2.

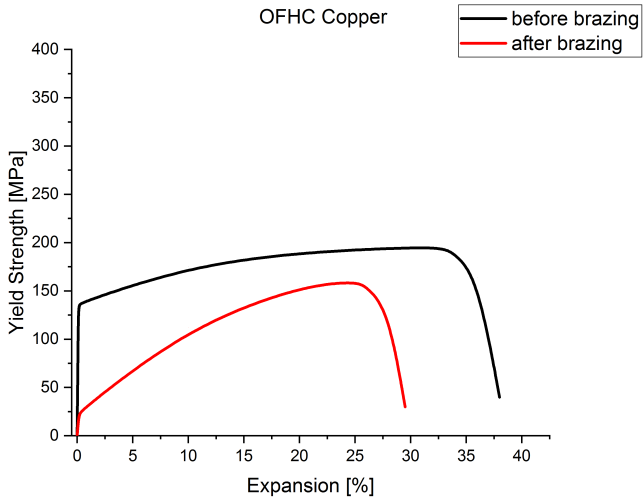

Figure 4.8: Results of a tensile test before and after the brazing of OFHC copper (performed at KIT).

After the brazing process a yield strength of Rp0.2 = 296.09 N/mm^2 remains, as shown in Fig. 4.9. The corresponding acceptable loads, under consideration of a safety factor of 3, are 3780 kg for the cavity and 23252 kg for the launcher. As a result, the yield strength is well below the maximum allowable yield strength for both components.
As a summary it can be mentioned, that OFHC copper is losing 82 % of its yield strength during the brazing process (one heating cycle). The yield strength is further decreasing under gyrotron operation. Compared to this, Glidcop loses only 3.5 % of its strength (Rp0.2), which is due to the Al_2O_3 content. Compared to OFHC copper, Glidcop is easier to machine due to the harder material texture. Due to the investigations of the yield strength, it is proposed to use Glidcop for the cavity. Glidcop is much harder and is more resistant against fatigue which occurs during the operation cycles. The launcher is made of OFHC. Due to the lower loading of 0.4 kW/cm^2 and the thicker launcher wall of 10 mm the use of OFHC is sufficient, which is also by factor 10 cheaper.

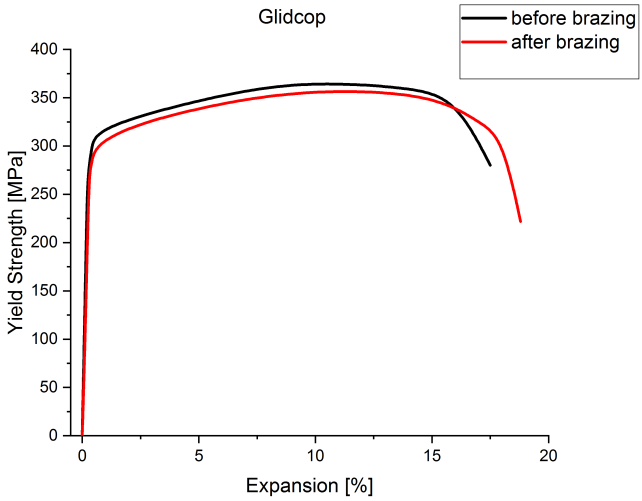

Figure 4.9: Results of a tensile test before and after the brazing of Glidcop Al-15 [23] (performed at KIT).

4.4 Summary

Successful brazing and welding is a necessary requirement for the in-house manufacturing of cost-efficient modular long-pulse gyrotron components. Therefore, in this chapter an advanced welding and brazing procedure for high power vacuum tubes was presented. The fundamental investigations in this work have shown that the nickel-base super alloy braze is a suitable brazing material for in-house manufacturing of vacuum compatible gyrotron components. For the first time, a brazing procedure based on a nickel-base super alloy braze was successfully established for in-house manufacturing. In addition, the systematic analysis of grinding patterns of different brazing configurations have significantly improved the brazing process and consequently the quality of the in-house manufactured gyrotron components. Furthermore, that braze offers the possibility of an easy handling without the necessity of a component assembly under vacuum conditions or the use of soldering flux for the reduction of oxide layers. In addition, the KIT in-house brazing costs were reduced to only 2 % of the original costs if compared to standard process used at KIT. This allows the manufacturing and test of several advanced and optimized gyrotron components.
The knowledge know-how, which has been gained in this work, opens the path for an in-house manufacturing of modular, cost-efficient and water cooled long-pulse gyrotron components.

5 Cooling technologies for highly loaded gyrotron components

The potential of the coaxial-cavity gyrotron technology has been already shown in short-pulse operation, see Rzesnicki et al. [25]. With the reduced voltage depression and mode competition, significantly higher RF power levels and higher order modes can be reached compared to conventional hollow cavity gyrotrons. In order to show that the coaxial-cavity gyrotron is a DEMO relevant approach, the successful operation in steady-state has to be shown. Following, this operation regime will be called long-pulse operation. To run the gyrotron at long-pulse operation, the beam-tunnel, the cavity, the launcher, the mirrors, the chemical vapor deposited (CVD) diamond RF output window [83] and the collector have to be equipped with an active cooling system. In addition, the cathode and body of the MIG has to be equipped with a cooling system for the long-pulse operation. The fundamental project requirement is to keep the modularity of the demountable gyrotron. For the first time, an independent cooling system is implemented for each single component. The advantage of the independent cooling setup is the monitoring of the internal losses of each gyrotron component. One of the main challenges in the development and manufacturing of the new long-pulse gyrotron is the interpretation of the cooling system and the handling of the power loading in the cavity of maximum 2.5 kW/cm^2.

For the long-pulse gyrotron development a two-step approach is considered. For the first step, the coaxial cavity gyrotron was designed for a maximum pulse length up to 100 ms. This step requires an active cooling system of the cavity, beam-tunnel and launcher as well as advanced MIGs with better cooling conditions. The aim of this first phase is the verification of the new gyrotron setup and the operation in the partly neutralized (60 - 70 %) electron beam regime. In phase two, the CVD diamond disc is equipped with a water cooling system for a pulse length of up to 1 s. In addition, a CW compatible collector with sweeping coils is necessary. The objective of phase 2 is the operation in

steady state conditions and the verification of a CW compatible design. The cooling necessity is summarized in Table 5.1. The pulse length estimations are based on the successfully tested W7-X and ITER CW test results and scaled-up by the help of the COMSOL code to the coaxial-cavity gyrotron.

5.1 Cooling approach for long-pulse operation

In the following section, the cooling designs of the gyrotron components up to a pulse length of 150 ms are presented. In addition, a thermomechanical analysis is done to identify critical regimes of thermal treatments. Unique is the consideration of the physical and thermal analysis, as well as the realization which are presented in this work.

5.1.1 Design of the launcher structure for long-pulse operation

As stated already in Section 2.1, the launcher, as shown in Fig. 5.1, is a circular waveguide antenna, which is together with the mirror system responsible for the conversion of the main $TE_{34,19}$-mode into the fundamental Gaussian mode of the RF output beam [84]. The mode conversion is determined by the perturbations at the inner waveguide wall.

At the top of the launcher the maximum thermal loading is 0.4 kW/cm^2.

Table 5.1: Necessary water cooling systems for the gyrotron subcomponent with respect to the pulse length.

Pulse Length	Necessary Water Cooled Components
$\leq$ 100 ms	Cavity
	Launcher
	Beam-Tunnel
$>$ 100 ms	CVD Diamond Disc
	CW Compatible Collector Cooling

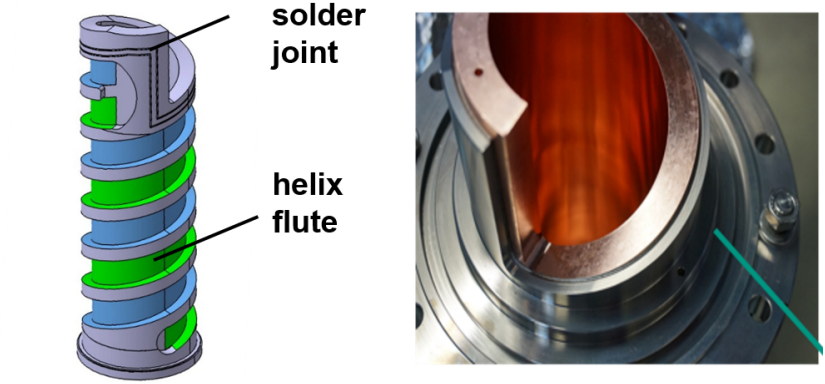

Figure 5.1: Design and manufactured launcher with the helix shaped water channel [23].

To avoid overheating in long-pulse operation, an efficient cooling is required. Because the launcher top part protrudes into the mirror box and is surrounded by vacuum, it is proposed in Ruess et al. [23] that the water inlet and outlet are fixed at the bottom of the launcher. To make the cooling of the launcher possible, an advanced helix structure is implemented. Due to the complexity, the channels were milled with a 5-axis milling cutter. Subsequently, the helix channels were caulked by a stainless steel coat, which was fitted from the outside and vacuum tight brazed [23]. The implementation of a below is necessary because the coat and launcher have different operating temperatures and therefore thermal strains have to be compensated. The manufactured launcher shows an excellent reflective surface quality. The tolerances are in the range of below ±6 µm. The launcher is made from OFHC copper [23].
The cold launcher performance has been successfully verified at KIT. A detailed description of the test procedure is given in Ruess et al. [85]. The simulated radiation pattern in Fig. 5.2(a) was calculated with the full wave 3D vector analysis code SURF 3D [86]. Fig. 5.2(b) shows the radiated pattern which was sampled with a rectangular waveguide antenna at a distance of 10 cm from the launcher [23]. By comparison of the amplitudes it can be clearly seen that the measurement results correspond well with the simulation results.

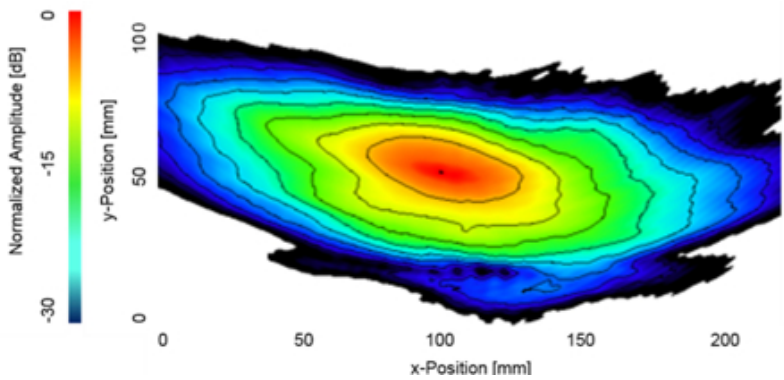

(a) Simulated radiation pattern.

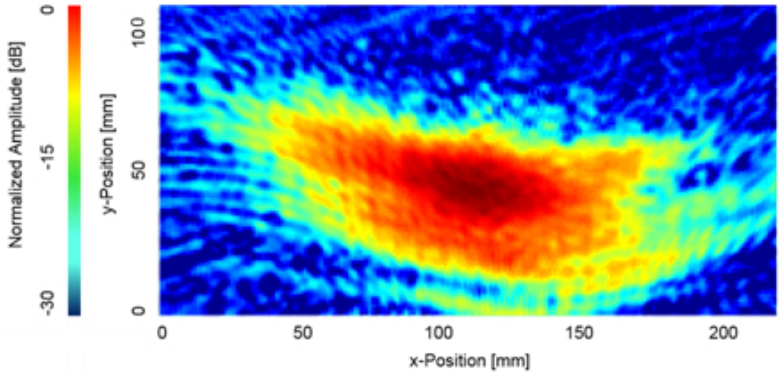

(b) Measured radiation pattern.

Figure 5.2: Simulated (a) and measured (b) radiation patterns of the water cooled long-pulse launcher [23].

5.1.2 Design of a cavity capable to operate at long-pulses

The cavity is also part of the modular approach. This opens the way for the two-stage expansion. In the first step, a conventional annular gap cooling, up to a pulse length of 100 ms, is developed and implemented. In the second step, the annular gap cooling will be replaced by an advanced minichannel cooling approach, which allows the operation in CW operation.

In the gyrotron cavity (as shown in Fig. 5.3) a part of the perpendicular kinetic energy of the individual electrons of the electron beam is transferred to the electromagnetic field. The inner structure marked in orange in Fig. 5.3 consists of a down-taper, a mid-section and an up-taper. Compared to the short-pulse cavity, the cavity up-taper is extended in z-direction (as shown in Fig. 5.4) so that the center of the mid-section is in the nominal position (maximum of magnetic field density). Based on the simulation results a transmission of 99.94 % of the $TE_{34,19}$-mode and a very low undesired mode conversion [23] can be expected. The simulations were performed with a scattering matrix resonator code [87]. Compared to the short-pulse gyrotron, the cavity center in the long-pulse pre-prototype gyrotron is positioned at the maximum magnetic field strength. Therefore, an increase in output power and efficiency can be expected with the new long-pulse gyrotron.

The simulated RF power loss in the outer cavity wall is about 35 kW at nominal 2 MW gyrotron operation, with a maximum thermal wall loading of 2.0 kW/cm^2 in a narrow region at the cavity center [23]. The temperature

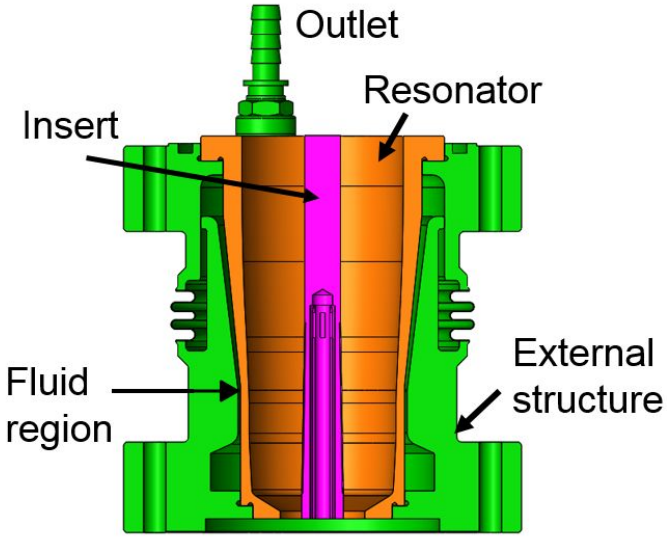

Figure 5.3: Physical design of the pre-prototype cavity [23, 88].

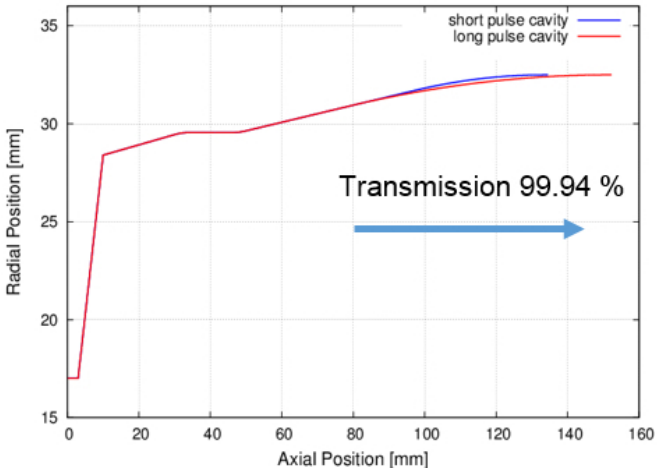

Figure 5.4: Comparison of the short pulse cavity (blue) and the long-pulse cavity (red) [23].

distribution leads to a very high temperature gradient at the cavity wall. As a result, thermal stresses, thermal expansions and deformations occur [89]. Depending on the deformations, the gyrotron operating frequency is shifted and the quality factor of the coaxial-cavity is changing. In order to keep the thermal expansion at low level it is mandatory to implement an advanced and effective cooling system. Compared to the launcher cooling system the implementation of a helix shaped water channel is not necessary [23]. Therefore, an advanced annular gap cooling could be installed with a significantly higher flow rate, which results in an increasing heat transfer coefficient. The different operating temperatures of the inner cavity Fig. 5.3 (orange part) and the external structure (coat) requires also the implementation of a bellows [23].
The temperature limitation of the cavity is 250 °C, in order to reduce fatigue and increase the lifetime of the cavity [23]. Based on the temperature limitations, the multiphysics software COMSOL predicts in S.Ruess et al. [23] and A. Bertinetti et al. [88] a maximum pulse length of approximately 150 ms, as shown in Fig. 5.5. The steady state operation is reached after 600 ms. In continuous wave operation the temperature will reach 360 °C, which is above the maximum acceptable temperature. Due to the radial expansion the operating frequency is decreasing and fatigue is created. Therefore, that approach

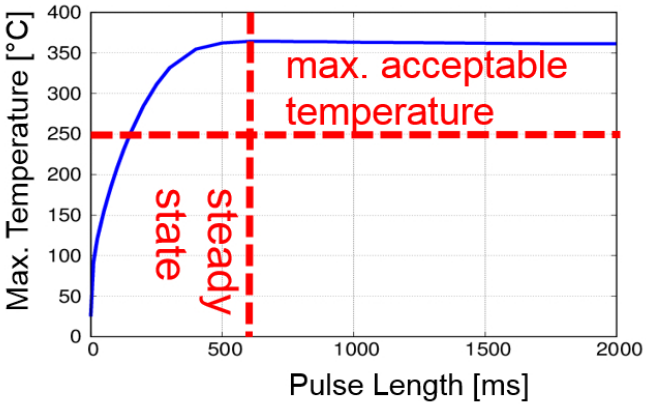

Figure 5.5: Maximum temperature at the cavity center versus the pulse length [23, 88].

is not suitable for phase 2. In Fig. 5.6 the polar temperature plot shows an inhomogeneous temperature distribution of $\Delta T = 44$ °C [23, 88] in steady state operation, which causes a significant unsymmetrical thermal expansion. The displacement in radial direction is 0.04 mm and 0.05 mm in axial direction, respectively (as shown in Fig. 5.7).
This inhomogeneity can be reduced using multiple in- and outlets. However, the mechanical complexity is increasing. For operation above 150 ms an optimized water approach is necessary and will be discussed in Section 5.2.

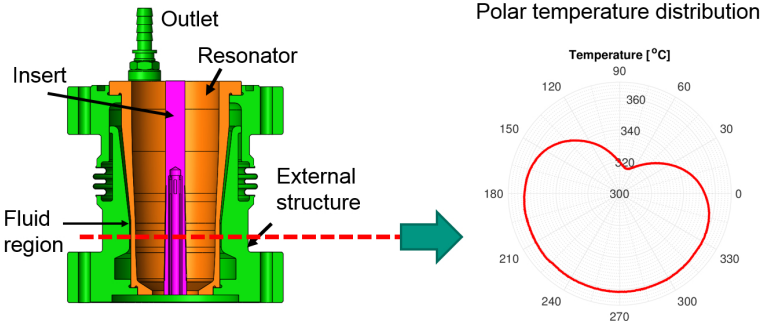

Figure 5.6: Geometrical design and polar temperature distribution at the cavity center [23, 88].

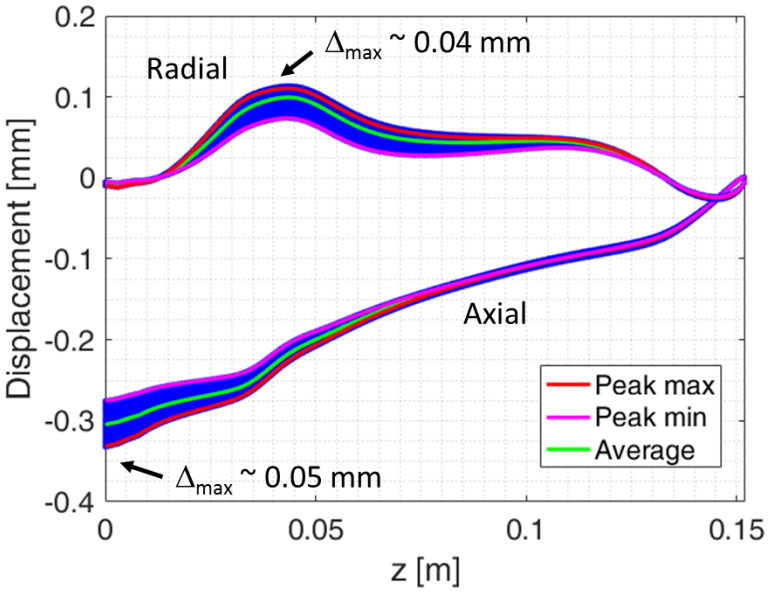

Figure 5.7: Displacement of the cavity in axial and radial direction [23, 88].

5.1.3 Design of a beam-tunnel structure capable to operate at long-pulses

The beam-tunnel (as shown in Fig. 5.8) is the region were the electron beam is adiabatically compressed by the externally applied magnetic field. Passing the beam-tunnel the electron beam radius is decreasing and the pitch factor is increasing due to the increasing magnetic flux density. It has been shown that in the beam-tunnel parasitic modes can be excited, as stated in Kumar et al. [90] and Tigelis et al. [91]. Even at low power levels the parasitic modes can increase the spread of the electron beam due to an unwanted interaction and the accordance of the resonance conditions at corresponding beam-tunnel positions. Therefore, it can be concluded that the unwanted oscillations are strongly dependent on the geometry. In today's gyrotrons, there are three types of different beam-tunnel configurations:

1. A full dielectric conical SiC beam-tunnel, where the parasitic mode is absorbed, see Pedrozzi et al. [92];
2. A full metallic beam-tunnel with irregular wall geometry, where the parasitic mode is compressed, see Malygin et al. [93];
3. Alternating rings of metal and lossy dielectric are used to suppress and absorb these parasitic oscillations, see Tigelis et al. [91] and Rzesnicki [94].

For the beam-tunnel of the long-pulse pre-prototype gyrotron the already at KIT patented third approach is followed. The beam-tunnel of the modular pre-prototype consists of stacked copper and ceramic rings (ROBAX) [23], which will be implemented only in short-pulse operation. The ROBAX rings

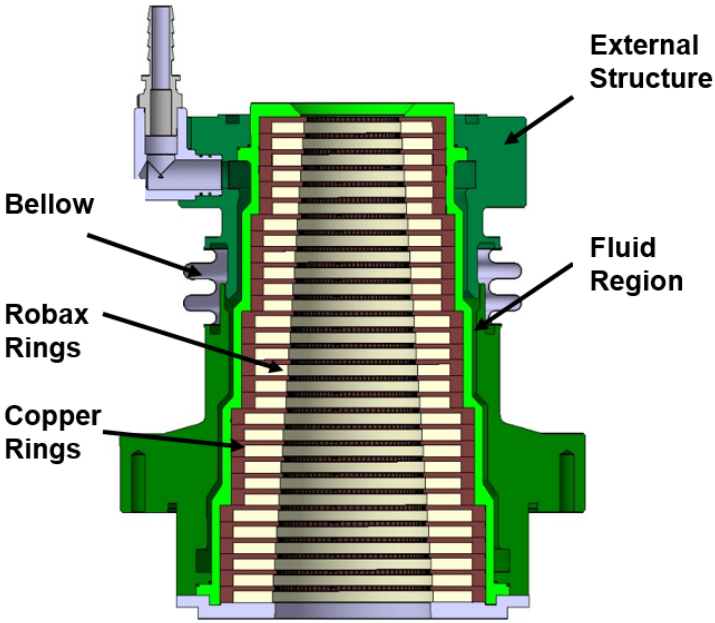

Figure 5.8: Physical design of the long-pulse pre-prototype beam-tunnel [95].

have a measured ϵ_r of approximately 5.7 and a loss tangent of 0.058. However, it has to be mentioned, that for a serial CW gyrotron ROBAX is an unsuitable material. The copper rings have on the inner side corrugations to break the azimuthal symmetry, for the suppression of the $TE_{0,n}$-backward waves. In case of an unwanted oscillation in the beam-tunnel the estimated maximum thermal loading is 10 kW [23]. Fig. 5.9 shows the construction of the beam-tunnel including the water cooling system. A jacket is brazed to the outside of the beam-tunnel. Together with the outer jacket it forms an annular gap cooling [23]. In the current design of the modular pre-prototype the copper rings are not brazed to the water jacket, which is mandatory for a pulse length above 150 ms due to the necessity of an improved cooling behavior of the ceramic and copper rings.

Figure 5.9: Stacked beam-tunnel, with corrugated copper and ceramic rings [96].

5.1.4 Advanced water-cooled mirror box design

The mirror box of the long-pulse pre-prototype gyrotron is shown in Fig. 5.10. In the physical design, the mirror box is already equipped with a water cooled diamond disc and water cooled mirrors and can therefore operate up to a pulse length of 1 second. Below the mirror box, the launcher is fixed, while at the top the collector is connected with a Helicoflex sealing [23, 97]. The Helicoflex is a type of flexible and elastic metal O-ring gasket. In addition, at the relief window a waveguide is connected which guide a part of the RF stray radiation to the measurement setup, where the transient response and frequency behavior can be investigated. At the coaxial-cavity modular pre-prototype gyrotron the mirror box is at body potential and has to be isolated from the grounded superconducting magnet [94]. Therefore, a GFK isolation is mounted between the mirror box and the magnet. The flow and return of the water cooling system for the beam-tunnel, the cavity and the launcher are connected at the bottom plate of the mirror box. Isolation between the water pipes and mirror box are needless due to of the use of deionized water.

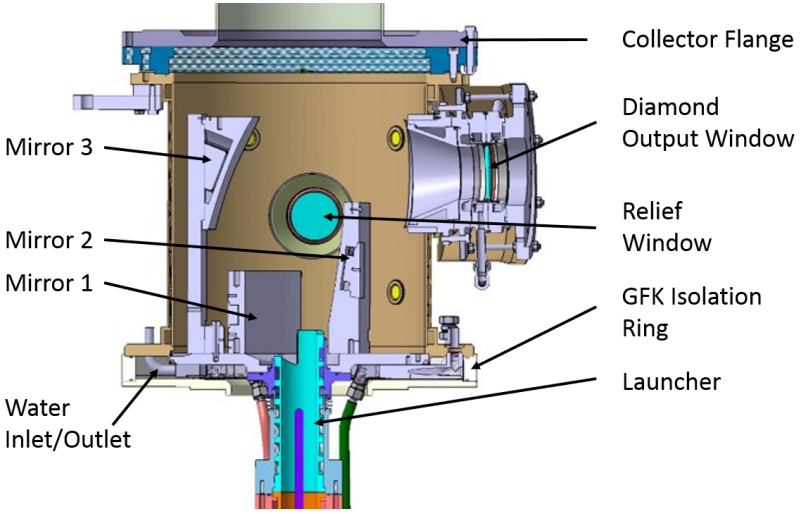

Figure 5.10: Design of the long pulse preprototype gyrotron, prepared for the operation in long-pulse.

To build-up an economical pre-prototype long-pulse pre-prototype, the quasi-optical system, consisting of the mirror box and mirror 1 to 3, are reused from the refurbished industrial coaxial-cavity 2 MW 170 GHz gyrotron prototype [21, 98]. However, strong modifications at the CVD window housing, the top flange and at the absorber ceramic are necessary to meet the requirement of the modular approach. Due to the operation at long-pulse regime, it is necessary to bake-out the pre-prototype gyrotron above the maximum reachable temperature. In case of the pre-prototype gyrotron the maximum temperature of 250 °C is dominated at the cavity outer wall [23]. Therefore, the selected bake-out temperature is 300 °C [23]. This requires that the water channels and connections are heat-resistant up to the maximum bake-out temperature. Therefore, metallic sealed cooling components are developed and added to the construction [23]. The metallic sealing has been successfully tested up to a water pressure of 8 bar [23].
The stray radiation in the mirror box is estimated to 5 % of the overall RF-power. The stray radiation is related to misalignment and manufacturing tolerances of the launcher and the mirrors and to diffraction losses. In order to reduce the remaining stray radiation, a relief window was added to the mirror box. In addition, to reduce the temperature of the mirror box, the stainless-steel housing is covered with copper and the whole mirror box coat and ground is cooled by an installed cooling system.

5.2 High efficient cooling systems for future continuous-wave operation

In the coaxial-cavity long-pulse gyrotron, presented in Section 5.1 an annular gap cooling is considered. With this cooling approach, the cavity is reaching after 150 ms the maximum temperature of 250 °C. To exceed the limitations and to ensure CW operation, new cooling concepts have to be elaborated. Therefore, pioneering cooling systems with significantly higher cooling capabilities will be presented. The focus of the cooling system is:

- The development of a cooling approach with a higher heat transfer coefficient compared to current systems.
- A cooling system with a high reliability and user-friendly handling.

5.2.1 Minichannel cooling system

In today's CW fusion gyrotrons manufactured by Thales, the Raschig Ring cooling is implemented for the cooling of the cavity. In order to handle even higher wall loading in future fusion gyrotrons, advanced cooling approaches are necessary. A very promising approach is the minichannel cooling system, presented in Bertinetti et al. [88]. The main advantages of the minichannel cooling approach compared to the annular gap cooling is the possibility of higher water speed in the channels and therefore a more turbulent behavior and a corresponding higher heat transfer coefficient [99]. In addition, the distance between the water flow and the thermally loaded surface can be significantly reduced. Numerical simulations, as shown in Fig. 5.11 and Fig. 5.12 predict a maximum cavity surface temperature of 210 °C in steady state operation, which is below the maximum allowable temperature of 250 °C. The temperature difference of ΔT=13 °C is smaller compared to the annular gap cooling (ΔT = 44 °C) presented already in Section 5.1.2. The boundary conditions for the simulations are an inlet flow rate of 3.7 m^3/h, inlet pressure of 8 bar and an inlet temperature of 40 °C. Numerical investigations have shown, that the best trade-off between minimum surface temperature and sufficient mechanical strength of the gap-surface distance is 0.85 mm with a channel diameter of 1.2 mm and a channel length of 35 mm for each of the 60 channels [88]. The risk of the minichannel cooling is the blockage of individual channels and the generation of possible steam explosion. Here, damages in form of

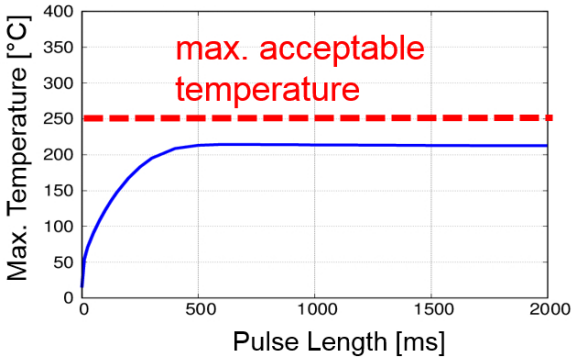

Figure 5.11: Temperature distribution versus the pulse length with mini-channel cooling.

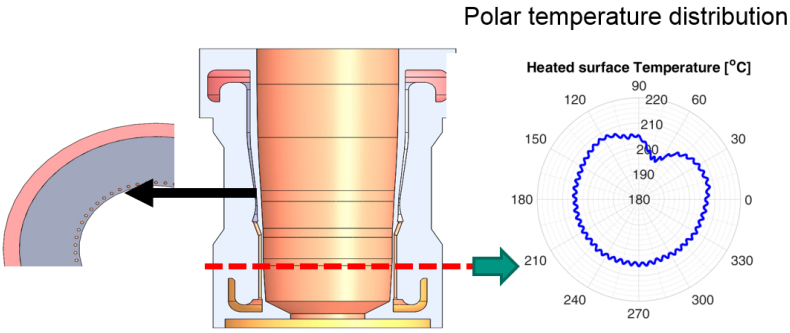

Figure 5.12: Design of the minichannel cooling approach with the simulated polar temperature distribution [23, 88].

deformations and cavitation may occur.

With the implementation of the minichannel cooling approach the temperature can be reduced by 42 % compared to annular gap cooling and 15 % compared to the Raschig Ring cooling system. In addition, tests have shown that the manufacturing of the channels can be made with sink erosion. This cost-efficient manufacturing process is even compatible with Glidcop.

Experimental verification of the minichannel cooling approach with a mock-up device

Currently, there is no experience with the handling of the mini-channel cooling system in Thales gyrotrons. Therefore, a test mock-up (as shown in Fig. 5.13) got built to verify the simulated results with the experimental data. In Fig. 5.14 a cross-section of the mock-up is shown. The inner contour of the mock-up matches the physical design of the long-pulse cavity. In the approach it was waved to implement half round channels to simplify the manufacturing process. The copper part (gray colored in Fig. 5.14) exists of 2 parts. During the assembly, the outer copper component with the drilled channels is heated up and placed over the inner tube. After cooling down of the outer copper component a press-fit is guaranteed. The burner, as shown in Fig. 5.15, is used as a heating source. The acetylene and oxygen mixture of gas has a total thermal

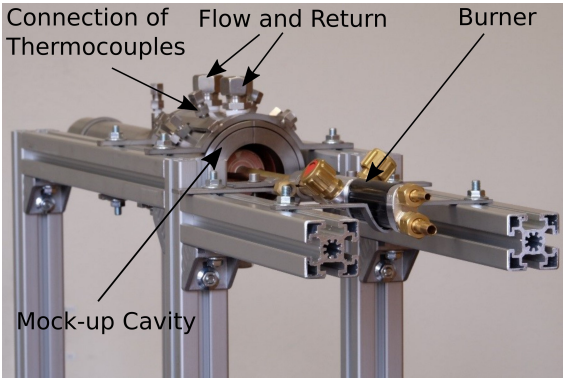

Figure 5.13: Experimental setup for the verification of the minichannel cooling system.

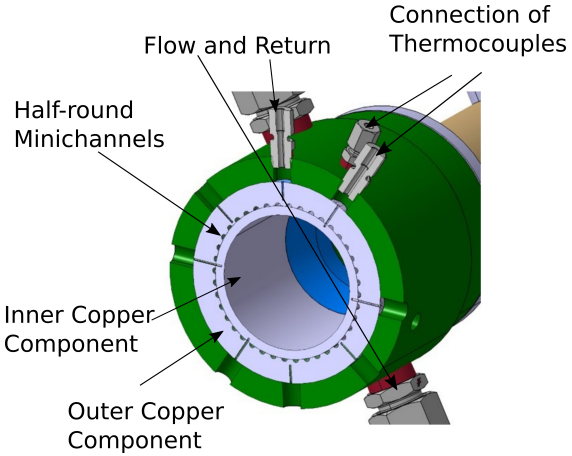

Figure 5.14: Mock-up of the minichannel cooling approach.

power of 36 kW. The flames of the burner are directed radially outward in order to have a thermal distribution, which corresponds in first approximation to the thermal distribution in the real gyrotron cavity. The heat transfer from the burner into the cavity is unknown and has to be calorimetrically determined in the experiment. Therefore, azimuthally 16 thermoelements of type K are allocated in order to measure the surface temperature in the cavity as well as

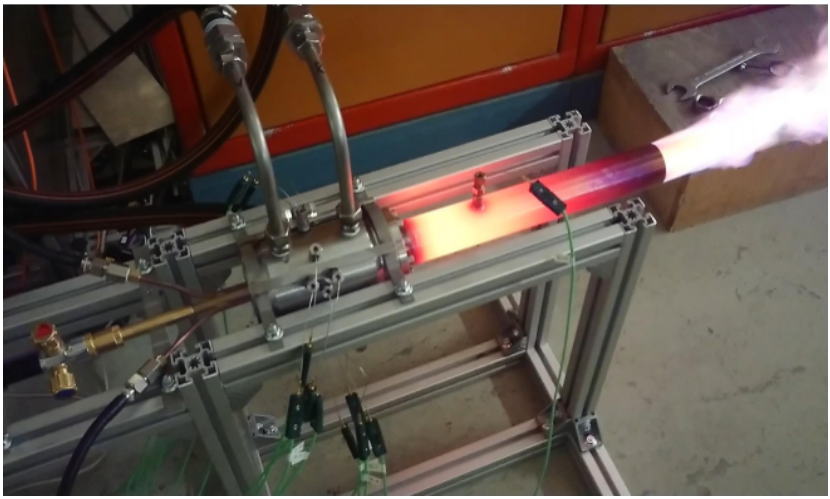

Figure 5.15: Minichannel mock-up in operation.

the inlet and outlet coolant temperature. The position of the thermoelements are selected so that the azimuthal temperature distribution, the temperature at the inner cavity surface, the temperature behind the channels (considered in radial direction), and the distribution in z-direction can be investigated. The azimuthal arrangement of the thermoelements offers in addition the possibility to predict the alignment of the burner in the cavity.

After the assembly of the minichannel mock-up device and installation of the automatically temperature measurement system and safety precautions, the mock-up has been experimentally investigated, as shown in Fig. 5.15. The surface temperature as well as the flow and return temperature of the water coolant are presented in Fig. 5.16. The temperature in the cavity surface is rapidly increasing and remains in a steady state temperature of 50 °C. In the time frame between 160 s and 200 s the power of the burner was increased to the nominal value. Accordingly, the temperature is increasing to 70 °C in steady state operation. During the experiment the temperature of the return flow is increasing up to 41 °C in steady state operation (up to 300 s) with a constant flow temperature of 18.1 °C. The slow response of the return flow temperature is related to the low flow rate of 2.2 l/min and the long water pipes

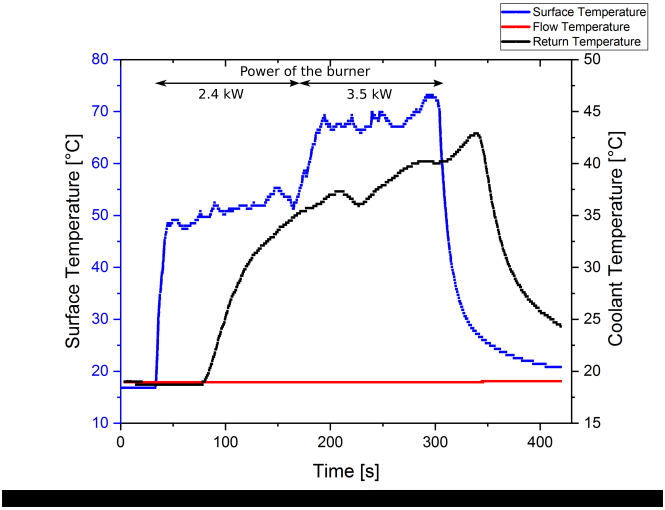

Figure 5.16: Temporal temperature profile of the surface as well as the flow and return temperature of the water coolant.

as well as the large diameter of the already existing pumping equipment. The absorbed thermal energy of the cavity can be calculated by:

$$Q = \dot{m} \cdot c_p \cdot \Delta T \tag{5.1}$$

With the flow rate $\dot{m}$, the heat capacity c_p and the temperature hub ΔT. The calculated absorbed power is 3.5 kW. Compared to the corresponding nominal power of the burner with 36 kW, the absorption in the cavity is 9.8 %. The low absorption is related to the small surface of the cavity and the high gas speed which is related to the stack-effect. It is proposed to replace the burner with an ohmic heater. Here, the losses can be directly measured.
In order to verify the simulation model and boundary conditions, the mock-up device was simulated with the CFD simulation tool ANSYS. For this simulation, as shown in Fig. 5.17, the input parameters like the absorbed power in the cavity as well as the flow rate are determined in the experiment. The simulated maximum temperature is 73.94 °C and matches the measured experimental temperature of 70 °C, presented in Fig. 5.16. It has to be mentioned that the

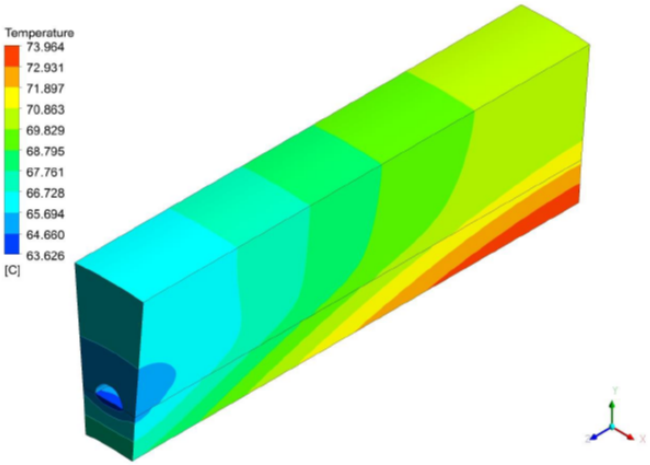

Figure 5.17: 3D CFD simulation results of a 20 deg section of the mock-up with a total water flow of 2.2 l/min and total absorbed power of 3.542 kW.

assumptions in simulation are successfully approved, which opens the path for a reliable interpretation of future gyrotron cooling systems.

5.2.2 Future spray cooling system

The overall motivation of the spray cooling system is a 10 times higher heat transfer coefficient [100] compared to concepts based on natural or faced convection (e.g. Minichannel cooling). Mudawar published already in [101], that with boiling phenomena a heat transfer coefficient of 100 W K/cm^2 and beyond can be achieved. In addition, Mudawar published also in [101] a spray cooling systems where the dissipated heat flux exceed 1000 W K/cm^2.

Reiners [102] speaks of spray cooling if the water exposure Vs is smaller than 3 kg/m^2 s^{-1} and the cooling liquid is present in fine droplets. The fluid is forced through a small nozzle that shatters it into fine droplets which then collide with the hot surface [102]. Based on Mueller [103], the simplest constructions are single-material full-cone nozzles that work on the principle of water jet disintegration. They are used when the liquid can be supplied under pressure, a sufficient amount of liquid per nozzle is available and no special

requirements and the drop size spectrum are made. The full-cone nozzle, used in this work, is designed to impart a swirl to the inflowing liquid in the inlet, resulting in an accurate circular radiation with a defined jet angle and uniform liquid distribution. In the axial nozzle, which is used in this work, the swirl is generated by a built-in swirler within the nozzle.

At small water exposures with the spray cooling system of Vs $\approx$ 0.1 kg/m^2 s^1, higher heat transfer coefficients were already measured compared with the stable film evaporation, as shown in Fig. 5.18. The high heat transfer characteristic can be explained by the latent heat of evaporation and additional high single phase convection effects due to the continuous impact of drop-lets. Kim is mentioning in [105] that this approach also allows a uniform temperature distribution of large surfaces. The heat transfer coefficient of the spray cooling system is strongly dependent on the water exposure as well as on the characteristic of the droplets (droplets density and velocity). The transition area between the spray cooling and film evaporation cooling is between V = 0.12 and 0.18 kg/m^2 s^{-1}.

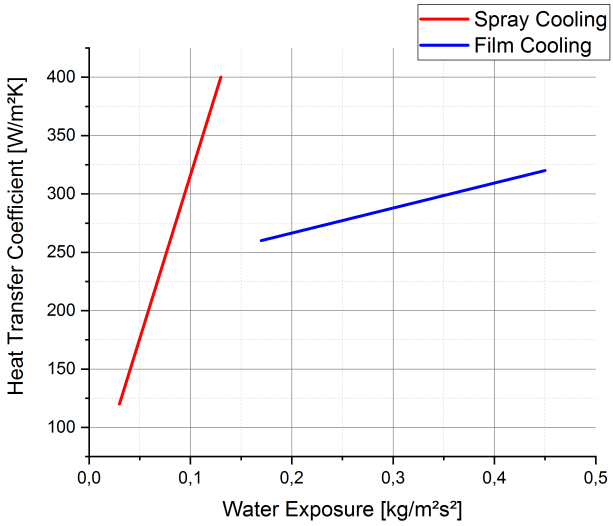

Figure 5.18: Heat transfer coefficient in dependency of the water exposure density [102].

A typical spray cooling curve is presented in Fig. 5.19 [104]. In the first regime at low wall temperatures, the curve is linear and convective effects dominate the heat transfer. The curve slope is increasing as the wall temperature is high enough that a phase change can occur. In Mudawar et al. [106] the effect of nozzle-to-surface distance on the critical heat flux using full cone sprays was investigated. Experimentally it was found out, that the nozzle-to-surface distance influences the cooling performance drastically. The maximum critical heat flux was achieved, if the spray impact area just inscribes the square surface of the hot plate [106]. The influence of flow rate, droplet size, droplet flux and droplet velocity on critical heat flux and heat transfer coefficient of a water spray cooling system were studied in Chen et al. [107]. They observed, that the droplet velocity has the most dominant effect on the heat transfer followed by the droplet flux. Experimentally the droplet velocity was increased from 4.64 m/s to 24.1 ms/1 and the diameter and droplet flux were kept nearly constant by using different nozzles (see [107]). The result was a critical heat flux increase by nearly 50 % and heat transfer coefficient by approximately

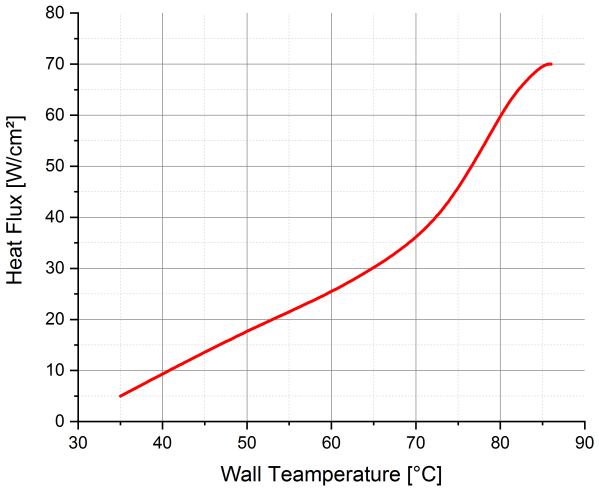

Figure 5.19: Heat flux coefficient versus the wall temperature [104].

40 %, respectively. In addition, Puschmann published in his work [108] that the droplet diameter has a negligible influence on the heat transfer characteristics. For a given droplet flux it is concluded that a dilute spray with fast droplets is more effective than a dense spray with low droplet velocities [107]. In addition, Xie et al. [109] presented that the heat transfer can be increased by increasing the surface roughness. If the surface roughness is larger than the liquid film thickness a two-phase effect occurs at the tips of the grooves, even at lower wall temperatures compared to smooth surfaces. The dependency of the heat transfer coefficent and liquid film thickness with respect to the surface roughness as well as the spray angle were investigated by Martinez-Galvan et al. [110–112].

Experimental Test of Advanced Spray Cooling Approach

In order to validate the theory, for the first time, a cavity mock-up was designed and manufactured for the spray cooling system as shown in Fig. 5.20. The cavity design of the spray cooling system matches the design of the cavity implemented in the minichannel cooling. The cavity is cooled by water bubbles, which are generated in the 5 nozzles. The used axial full cone nozzles are especially characterized by an extremely uniform liquid distribution over the entire circular area. The spray angle is 90 deg with a maximum throughput of 0.5 L/min at 3 bar. As shown in Fig. 5.21, 5 nozzles are installed in the cavity enveloping Plexiglas coat in which each nuzzle has its water connection to the water distributor. Therefore, the huge benefit of the spray cooling system is, that all channels can be monitored separately and a malfunction can be observed easily. This is one of the main advantages compared to Minichannel, Raschig ring and hyper vapotron cooling systems which is increasing significantly the operational security. The water flow and pressure is generated by a water pump with a maximum pressure of 3.5 bar. The water steam is going into the heat exchanger and is condensing there, while the condensate in the Plexiglas chamber is leaving it at the bottom and flows back to the reservoir.

As already mentioned, the mock-up is using 5 nozzles with a flow rate of 0.5 l/min each and 2.5 l/min in total, respectively. The evaporation heat ΔQ can be calculated by [113]:

$$\Delta Q = \Delta U + p\Delta V = \Delta H_v \tag{5.2}$$

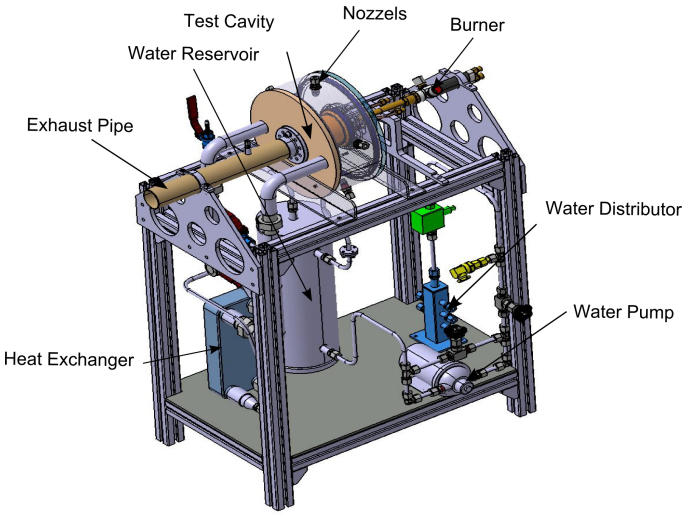

Figure 5.20: Complete mock-up of the spray cooling system.

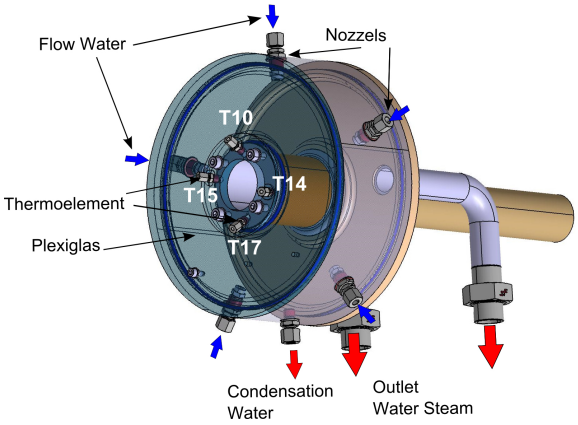

Figure 5.21: Configuration of the test cavity equipped with spray cooling. The inlet is highlighted in blue, the condensation water and water steam in red.

Which is also called enthalpy of vaporization. Under the assumption of a complete water evaporation of the 2.5 l/min the maximum possible diverted power of this mock-up is 94.04 kW at a pressure of 1013 mbar. However, the maximum absorbed power in the mock-up cavity is 3.543 kW which was already calorimetrically investigated in subsection 5.2.1. The evaporated amount of water with a heat power of 3.543 kW is 0.1 L/min. In Fig. 5.22 the temperature and flow rate are shown. It can be seen that the surface temperature is constant with a flow rate in the range between 0.4 to 1.4 L/min. The reason for the constant temperature is, that more than 0.1 L/min is available and the whole cooled cavity surface is wetted. At a flow rate of 0.35 L/min the temperature is significantly increasing, which is related to the fact that the cavity is no longer cooled. The reason is that the nozzles are not optimized for such a low flow rate and therefore the outer wall of the cavity is not covered completely with water. These areas are called hot-spots.

The difference between spray cooling and water film cooling can be seen in Fig. 5.23. During operation (e.g. with a flow rate of 0.6 l/min) the water which is not evaporating is accumulating at the bottom of the cavity. Therefore, a water film is generating at the bottom and evaporation does not occur. As a result, the thermocouple T14 (as shown in Fig. 5.23), which is located

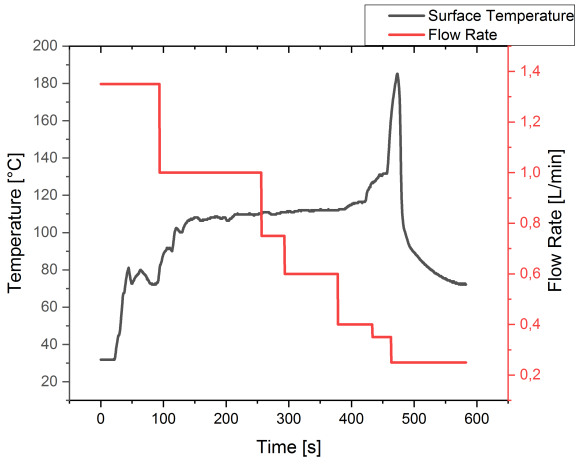

Figure 5.22: Temperature profile of the cavity surface for different flow rates.

at the bottom, shows the highest temperature which is related to the higher heat transfer coefficient. Compared to the experimental investigation with the minichannel cooling system, it can be concluded, that for the same heat extraction of 3.542 kW the innovative spray cooling systems needs 82 % less amount of coolant. This advantage is related to the enthalpy of evaporation of 2257 kJ/kg at 1013 mbar. In addition, the cooling properties can be further improved, by reducing the pressure in the cooling chamber below atmospheric pressure as shown in Fig. 5.24. With a reduction of the pressure to 0.03 bar the evaporation enthalpy is increasing to 2444.6 kJ/kg with an evaporation temperature of 24.1 °C which is 8.3 % higher compared to operation at ambient pressure. Operation at 0.03 bar with evaporated water is possible with an industrially available vacuum-water-ring pump. The correlation between pressure and evaporation enthalpy has in first approximation a linear behavior below 0.3 bar. Below 0.3 bar the evaporation enthalpy is exponentially increasing and exceeds an enthalpy of 2485.06 kJ/kg at 0.01 bar.

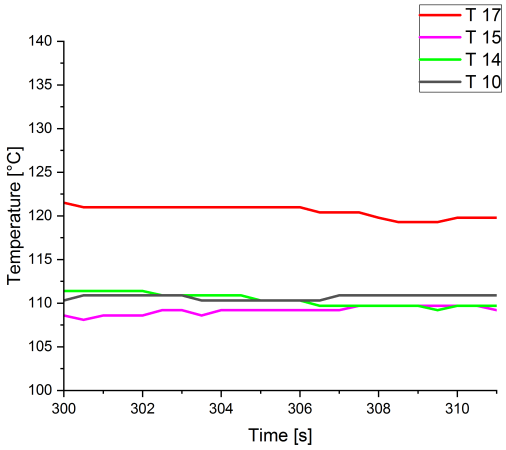

Figure 5.23: Temperature distribution of 4 thermocouples, which are azimuthally positioned with an angular distance of 90 deg.

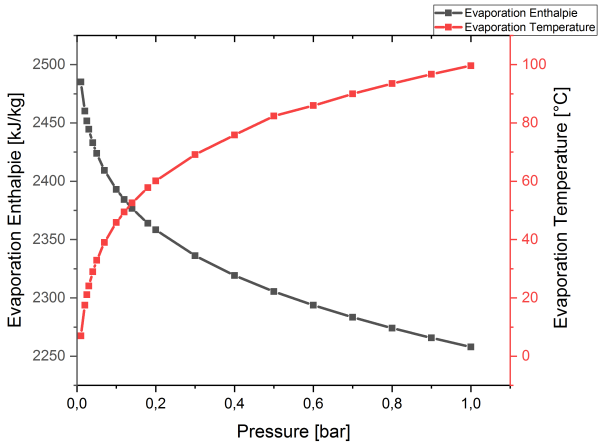

Figure 5.24: Evaporation enthalpy and temperature versus the pressure in the cooling chamber.

5.3 Cooling proposal for future DEMO gyrotrons

The high loading in the main gyrotron components is critical to handle. In the Subsections 5.2.1 and 5.2.2 advanced cooling methods are proposed. In addition, the large cooling potential of both approaches has been experimentally demonstrated. Based on the experimental results, manufacturing experience and the conditions in the gyrotron the installation of a spray cooling system in the collector would be a significant improvement. Currently, the collector is cooled with the hyper vapotron cooling method. Here, the droplets on the surface are generated by the turbulent flow at the grooves. This approach is very sensitive to the operating cooling parameters like groove size, flow rate and coolant speed. The advantage of the Spray Cooling compared to the Hyper Vapotron cooling approach is that the droplets are generated in the nozzles. Therefore, a droplet flow to the collector surface can be guaranteed. With the installation of homogeneous distributed thermocouples the temperature at the collector surface can be monitored. This monitoring opens the path for a control loop. Based on the surface temperature, the water flow through the nozzles can be adjusted to optimize the spray cooling conditions and the amount of evaporated water. A minichannel cooling in the collector is not

recommended due to the very high pressure drop in the 1.5 m long channel. The implementation of a spray cooling approach in the cavity is more complex due to the space consuming installation under the assumption of a radial injection. First investigations has shown that a compact tangential spraying into the cooling chamber is possible without a loss of performance. However, further investigations have to be performed. In addition, the spray cooling has the significant advantage that the pressure of all inlets can be monitored by a pressure sensor in all water supplies. Therefore, a constipation can be easily monitored and an error message will be shown. In the minichannel cooling, a possible constipation, due to erosion, cannot be detected. As a result, the water is boiling and damages at the cavity can occur. Therefore, for industrial gyrotron were the reliability plays an important role, the spray cooling approach is a promising solution. In addition, the surface temperature can be significantly reduced and fatigue in the gyrotron components can be minimized.

5.4 Summary

To achieve the goal of long-pulse operation with a modular gyrotron, a new cooling approach is needed. For this reason, a cooling concept was presented for the first time in this work, which allows each individual component to be cooled separately. This unique advantage opens the path for monitoring the losses of each gyrotron component separately. In addition, due to the modularity, each cooled gyrotron component can be exchanged by new advanced components. Numerical simulations predict a maximum pulse length of 150 ms for the annular gap cooling configuration. However, to reach the 1 s pulse length high efficient cooling systems are required. The numerical simulations and experimental measurements have shown that this goal can be achieved by the advanced Minichannel cooling for the cavity and a Spray cooling system for the collector. The spray cooling presented here is unique in its use in the field of vacuum electronics. Experimental investigations have shown a 10 times higher heat conductivity compared to minichannel cooling approaches. Therefore, the spray cooling, presented in this work, is a pioneering technology for highly loaded gyrotron components implemented in high power fusion gyrotrons.

6 Preparations for an efficient gyrotron operation at long-pulses

During the manufacturing process, the components are contaminated with coolants and lubricants. Furthermore, copper reacts with oxygen and forms an oxide layer on the surface during the assembly of the gyrotron. These impurities have a significant impact on the vacuum condition and the performance of the gyrotron. Therefore, it is mandatory to clean the gyrotron in advance, which is done by bake-out. This procedure, presented following, was specially developed for the modular long-pulse gyrotron to avoid leakages and thermal stresses during the heating phase [93].
Furthermore, for an efficient interaction, the cavity, insert and MIG have to be well aligned to the magnetic field. Theoretical investigations have shown, that the insert misalignment should be smaller than 100 µm [41]. Therefore, in the following section a special focus is given to the alignment procedure of the insert.

6.1 Assembly of the new coaxial-cavity long-pulse gyrotron

For the long-pulse modular pre-prototype gyrotron an innovative new construction, as shown in Fig. 6.1, has been developed. This new construction is of a modular type without the use of a shaft which offers the possibility to be accessible from the outside. Compared to the current fusion gyrotrons the beam-tunnel, cavity and launcher can be installed directly from below to the mirror box, which is related to the renouncement of the shaft. Here, a fast replacement of the components can be ensured without to open the collector. A further advantage of the accessible components is the possibility of the direct component access and measurement of the position and alignment as well

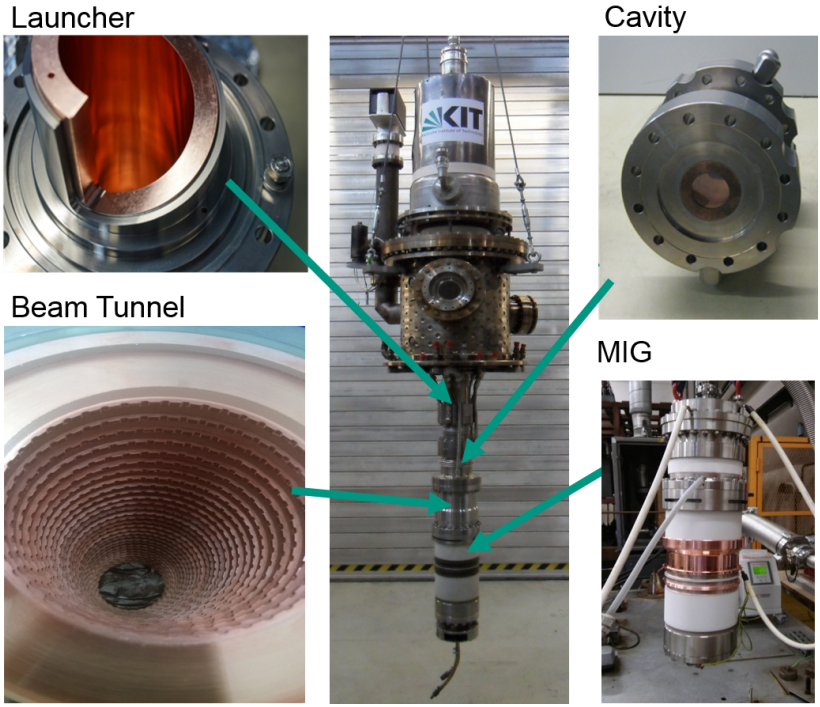

Figure 6.1: Assembled coaxial-cavity long-pulse gyrotron equipped with the old pre-prototype short-pulse Magnetron Injection Gun.

as the outer surface temperature. In addition, with this unique approach, no thermal isolation between the beam-tunnel, cavity and launcher with the shaft exists. Therefore, a more efficient and faster bake-out is feasible because the heat can propagate directly to the gyrotron components.

6.2 Proper conditioning for long-pulse operation up to 100 ms

Impurities and oxide layers have a significant impact on the vacuum level and the gyrotron performance. Therefore, the gyrotron was baked-out in the in-house oven up to 300 °C [114], which is clearly above the maximum operational temperature of 250 °C. The whole gyrotron including the sealing and flanges have been constructed for a bake-out temperature up to 400 °C , which is the maximum temperature for the CF copper sealing for a guaranteed leakage rate $\leq 10^{-9}$ mbar l/s. Especially the brazed connections with the nickel-base super alloy braze are successfully long term tested and verified up to a temperature of 500 °C.
The vacuum pumps of the oven are positioned outside and connected by flexible corrugated hoses to the gyrotron. From the outside, 12 thermocouples are connected additionally to the gyrotron in order to log the temperature [114]. The bake-out was monitored by a control system to which a defined process has been deposited [114]. The bake-out procedure is divided in three major phases, which were optimized in frame of this work. In the first phase, the temperature of the pre-prototype gyrotron is increased slowly up to the nominal bake out temperature of 300 °C [114]. The temperature have to be slowly increased in order to raise up the temperature of the gyrotron homogeneously and avoid stresses and leakages. For the pre-prototype gyrotron, 7 days were spent for the first phase [114]. In the second phase, the temperature of the gyrotron was kept constant at the nominal bake-out temperature for another 7 days [114]. Subsequently, in the third phase, the heater in the oven was switched off and the temperature was slowly ramped down to avoid stresses in the components due to different thermal expansions and the use of different materials [114].
In the control system of the oven several interlocks are installed. The goal is to detect and prevent unwanted events. The most frequently occurring event is the increasing vacuum pressure during the heating-up process (phase 1). If the vacuum pressure in the gyrotron exceeds more than p1 = $1.0\text{x}10^{-6}$ mbar the oven keeps the temperature constant until the pressure is less than p2 = $5.0\text{x}10^{-7}$ mbar [93, 114], highlighted in Fig. 6.2 with event 1. If the vacuum pressure has reached the value p2, the oven continues to heat. If the pressure is exceeding the pressure level p3 = $5.0\text{x}10^{-5}$ mbar the oven stops immediately its operation and shuts down the temperature in a controlled manner [93] (marked in Fig. 6.2 with event 2).

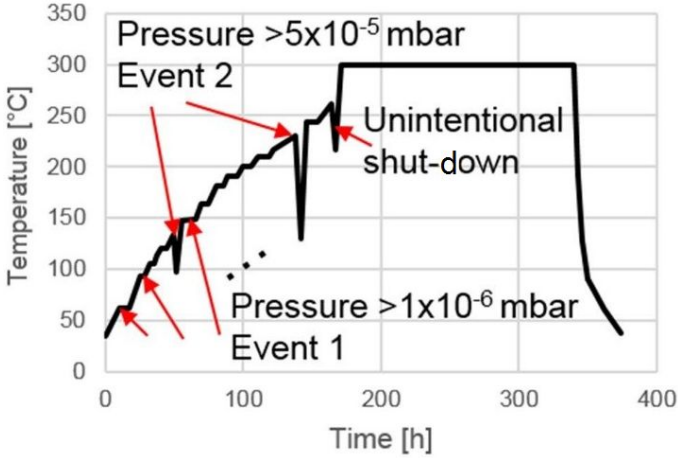

Figure 6.2: Temperature profile of the bake-out procedure of the coaxial-cavity long-pulse gyrotron.

Due to the bake-out process the tube vacuum pressure can be improved from $2.0x10^{-7}$ mbar down to $1x10^{-8}$ mbar at room temperature, which is the lower achievable limit of the vacuum turbo pump. However, it has to be mentioned that at 300 °C the pressure was only $8x10^{-7}$mbar at the vacuum pump. The reason is the installation of an annealed copper ring as a sealing between the collector and mirror box. This sealing is sufficient for short pulse operation, however, during the bake-out the sealing is getting softer and small holes are created. Therefore, the long-pulse modular pre-prototype could not be baked-out as required for long-pulse operation. The measurement of the vacuum pressure during the bake-out shows clearly, that for an efficient bake-out the gyrotron has to be sealed with a proper Helicoflex sealing. As a result, without the Helicoflex sealing the maximum expected pulse length is 10 ms. Based on this understanding, the temperature profile was optimized by inserting two temperature breakpoints at 100 °C and 250 °C for an improved temperature distribution.

After the bake-out procedure of the pre-prototype gyrotron, the gyrotron was installed in the test stand and the conditioning process was performed. This first conditioning process included mainly the conditioning of the MIG. Herein the filament current was step wise increased up to a maximum vacuum level of

10^{-6} mbar. After the regeneration of the vacuum conditions the process was repeated up to the nominal filament current of 19 A. In the second conditioning step the voltage stand-off was improved by the generation of provoked arcs inside the MIG region. Here a cleaning effect is generated, which is related to the evaporation of the unwanted oxide layer at the stainless steel and copper components, mainly at the insert, the cathode and the anode. This conditioning step is performed with a cold emitter. Discharges in the MIG regions were observed above 65 kV with a maximum vacuum level of $5\text{x}10^{-5}$ mbar in the long-pulse coaxial-cavity gyrotron. In the third conditioning step a combination of the first and second step is executed. In this conditioning procedure the beam current is increased step wise by increasing the filament current. Initially the starting beam current is smaller than $I < 0.01$ A with an acceleration voltage of smaller than $U < 1$ kV and a pulse length of 300 µs. The pulses were repeated several times with the same beam parameters in order to improve the vacuum conditions. When the maximum vacuum level during the pulse was improved below $5\text{x}10^{-7}$ mbar the beam parameters were increased step wise. The procedure was finalized when the nominal beam parameters ($U = 90$ kV, $I_b = 75$ A) were achieved. During the pulses the magnetic field configuration was changed to collect the electron beam at the collector at different positions. As a result, a large area of the collector is conditioned and cleaned from the unwanted copper oxide layer. Due to the losses of the RF beam at the cavity, the launcher and the three mirrors, the temperature is locally increasing and an additional conditioning takes place.

6.3 Alignment of the mechanical axis of the modular pre-prototype

For an efficient gyrotron operation an exact alignment of the mechanical gyrotron axis is necessary. I.e. the axis of the MIG, the axis of the resonator and the axis of the insert regarding the axis of the magnetic field. The orientation of the magnetic field determines the drift of the hollow electron beam [4]. Therefore, the alignment of the axis of the electron beam relative to the axis of the magnetic field has to be satisfied to guarantee a concentric electron beam regarding the axis at the cavity and insert. Measurements have shown, that the maximum radial concentricity deviation of half the electron beam width ($\approx \lambda/8 \approx 0.2$ mm) can be tolerated, see Samartsev et al. [115] and Rzes-

nicki [94]. The requirements refer to the position of the electron beam relative to the insert and cavity wall. Due to the very high tolerance requirements it is very important to measure the accuracy of the mentioned gyrotron components at the nominal operation condition, and, if necessary to correct them. The measurement of the electron beam position relative to the insert and cavity wall can be done by the help of the already installed dipole coils (installed in the superconducting magnet). These coils offer the possibility to shift the electron beam in the XY-plane. With a positive coil current I_x the hollow electron beam can be moved in positive x-direction, while with a negative coil current -I_x the beam can be moved in negative x-direction, which is shown in Fig. 6.3. The movement in y-direction can be performed with I_y similarly. At a certain lateral deflection some electrons hit the insert and an insert current can be measured. For a perfect homogeneous and aligned hollow electron beam and insert, the insert current versus the dipole current has a U-shaped distribution, with a mirror plane at I_x or I_y at 0 A. A realistic measurement is shown in Fig. 6.4. The shift of the mirror plane in the measurement result shows, that the insert is not aligned. The insert in x-direction is 0.036 mm displaced, while the displacement in y-direction is 0.032 mm. The relation between dipole current and the electron beam shift is given in Rzesnicki [94]:

$$\Delta R_{beam} = 0.012 \text{ mm/A} \cdot I_{x,y} \tag{6.1}$$

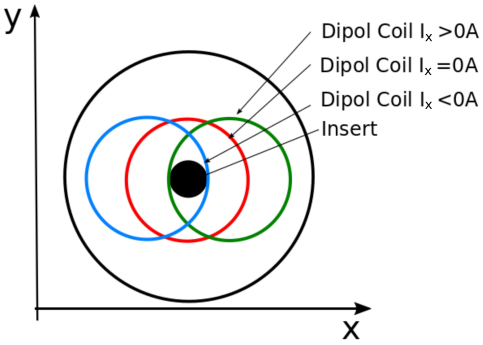

Figure 6.3: Electron beam position for 3 different dipole coil currents

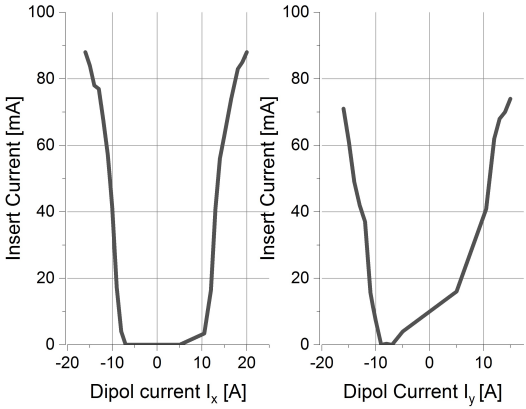

Figure 6.4: Measurement of the insert current at different excitations of the dipol currents in x- and y- direction.

The mentioned misalignment of the insert is negligible and therefore a stable gyrotron operation can be expected. Based on the measurement it can be seen, that the insert can be aligned within a range of ± 30 µm. By the current distribution at the insert, the homogeneity of the electron beam can be determined. A perfectly homogeneous electron beam without the emission of secondary electrons has a U-shaped insert current versus the dipole current distribution. In the flat top region, the insert current should be zero. In addition, the edges on both sides should be steep. This measurement method is a unique advantage as it is exclusively found in coaxial-cavity gyrotrons. A comprehensive overview of this process is given in Rzesnicki [94].
After the alignment of the insert axis regarding the beam axis, the electron beam have to be aligned to the axis of the cavity. In the coaxial-cavity short-pulse pre-prototype the installation of an adjustment probe at the cavity was used to align the cavity [94]. In this work it was waived to use such a probe in order to suppress unwanted oscillations in the cable of the probe. However, the alignment of the cavity can be sufficiently accurate determined by measuring the excitation circle, as shown in Fig. 6.5. This procedure was already performed in Ioannidis et al. [116]. In this measurement the electron beam is shifted with the dipole coils till the boundary where the nominal $TE_{34,19}$ mode is lost. This procedure is repeated several times for

different dipole current configurations as shown in Fig. 6.5. Finally, a circle is fitted through the measurement points and the center is defined as the optimum operation point which is for the current case I_x = -7.95 A and I_y = -5.15 A. This rough estimation of the optimized operation point is very quick but effective. In addition, this measurement of the coaxial-cavity short-pulse pre-prototype MIG will later be used to compare the emission homogeneity with the advanced conventional coaxial-cavity MIG with coated emitter rims.

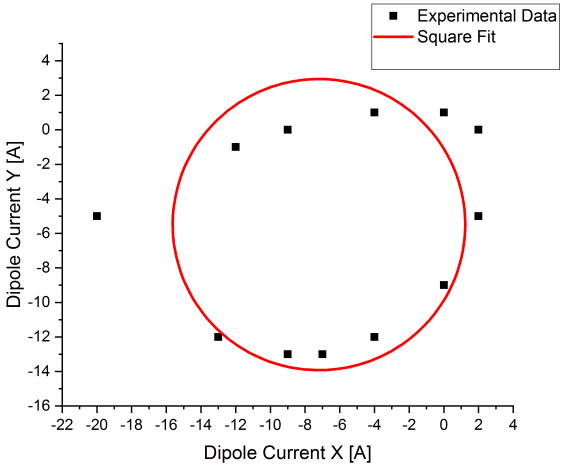

Figure 6.5: Excitation circle of the gyrotron at nominal operating parameters in order to check the alignment of the gyrotron.

6.4 Summary

The proper conditioning of a high power fusion gyrotron is essential for a reliable operation. Therefore, in this chapter, a bake-out process for the long-pulse gyrotron was developed and applied. This process was complicated by the use of 14 flanges, the use of different gaskets (Helico Flex, CF and self-made wire gaskets) and mainly the large diameter of the mirror box gasket. This problem could be solved by the use of an advance control system and temperature profile.

7 Experimental verification of the long-pulse coaxial-cavity gyrotron

In the previous chapters, the necessary long-pulse relevant development, manufacturing and assembly steps are presented. Therefore, the behavior and performance of the advanced long-pulse coaxial-cavity pre-prototype gyrotron will be demonstrated below with two different MIGs. As a first step, the new coaxial-cavity long-pulse gyrotron will be verified with the well-known short-pulse MIG. Here, the exclusive performance of the long-pulse gyrotron can be investigated and compared with the existing short-pulse gyrotron performance. In a second step, the advanced conventional MIG with coated emitter rims will be installed to increase the power and efficiency of the gyrotron.

7.1 Gyrotron performance capabilities with the existing short-pulse magnetron injection gun

The 2 MW 170 GHz long-pulse coaxial-cavity gyrotron has been verified and compared with the existing performance results of the 2 MW 170 GHz short-pulse coaxial-cavity pre-prototype. For a better comparison, it was decided to use the composition of the new long-pulse gyrotron with the already existing Magnetron Injection Gun of the pre-prototype short-pulse gyrotron. This approach allows a better comparison between the old short-pulse gyrotron and the new long-pulse gyrotron in short-pulse operation. Furthermore, this approach prevents possible performance uncertainty of a new MIG. The goal of the first experimental investigation is the verification of the new coaxial-cavity design approach and the comparison with the numerical investigations. In addition, the experiment at nominal operation will show the reliability and quality of the new developed joint connections.

Experimental setup

In Fig. 7.1 the coaxial-cavity long-pulse gyrotron is shown in the superconducting magnet including the installation of the calorimeter which is used for the RF power measurement. For frequency measurements the RF signal is captured from the stray radiation at the relief window and guided with a waveguide to the measurement system. Furthermore, the gyrotron is isolated with a GFK ring between the cold magnet and the mirror-box. In addition, for higher voltage stand-off and cooling capabilities the magnet bore hole was filled with high voltage isolation oil. On top of the gyrotron two ion getter pumps are installed for continuous vacuum pumping. The usual long-pulse ion getter pump position at the mirror box is not applicable due to the too large dimensions and the resulting incompatibility with the furnace. In this set up the collector and cavity are cooled by deionized water.

Experimental operating parameters

In all the experiments the gyrotron was operated in non-depressed collector mode. Therefore, the collector, mirror box, launcher, beam tunnel, cavity and anode were connected to ground, while the cathode is on -90 kV at nominal operation. The magnetic field in the cavity is 6.76 T. The shift of the electron beam, which was determined in Section 6.3, was considered and compensated by the dipole coils. The filament current is 18 A at a nominal beam current of 75 A. The initial vacuum pressure is 10^{-8} mbar at the position of the ion getter pumps.

Experimental measurement results

In the experiment, the nominal $TE_{34,19}$ mode was successfully excited at 169.855 GHz, which was measured with the real-time spectrum analyzer. The measurements show that the gyrotron is operating stable at a single frequency. At an acceleration voltage of 85 kV a mode switch from the nominal $TE_{34,19}$ mode to the neighboring $TE_{33,19}$ mode at 167.788 GHz takes place. The maximum measured RF output power at the nominal mode is 2.1 MW with an electronic efficiency of 33 %. K. Avramidis et al. have shown in [117] and Fig. 7.2, that an excellent agreement between the experimental results and the

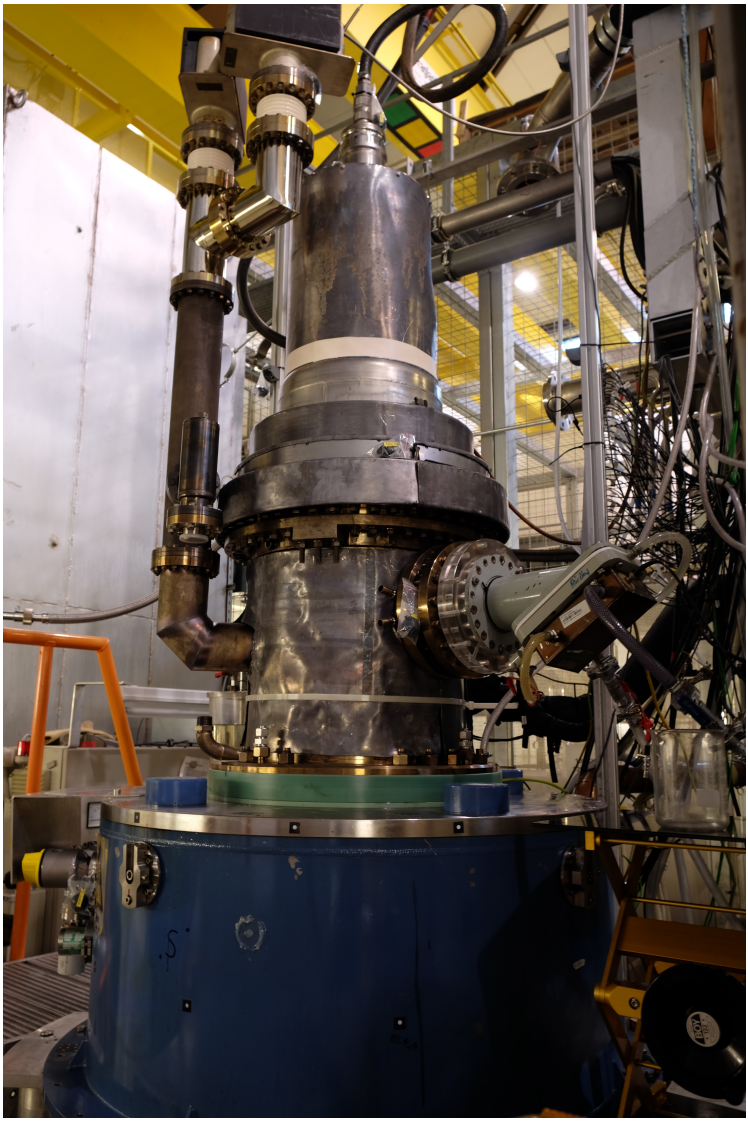

Figure 7.1: The coaxial-cavity pre-prototype long-pulse gyrotron in the superconducting magnet with the calorimeter for the RF power measurement.

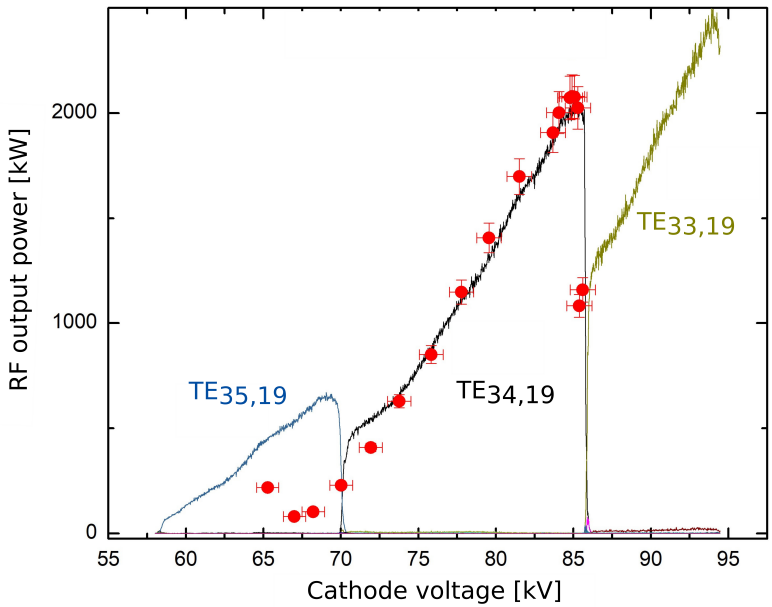

Figure 7.2: Experimental start up scenario of the new coaxial long-pulse gyrotron (red marks) in comparison with the simulations. A loss of 5 % in the cavity is considered in the simulation [117].

numerical simulations can be observed. Especially, in higher voltage regimes above 76 kV the simulation results and experimental measurements fits well for the $TE_{34,19}$ mode. However, a significant deviation can be observed for the $TE_{35,19}$ mode. This can be addressed to a discrepancy of 10 mT between the expected magnetic field and simulated field in the cavity region by considering the uncertainties in the coil current, remanence of the coil materials and misalignment of the gyrotron in the SCM. It has to be mentioned, that the magnetic field was calibrated by using an calibrated Hall sensor. Nevertheless, the simulations confirms the predictable behavior of the coaxial-cavity long-pulse gyrotron. These numerical simulation were performed with the KIT in-house code EURIDICE [118] under the consideration of a realistic start up scenario with linear raising acceleration voltage, as it happens in the experiment. For this process the electron beam parameters have been calculated with the elec-

tron trajectory code ARIADNE in the range between 45 kV and 95 kV.
It can be summarized, that with the optimization of the gyrotron key-components and technologies the efficiency could be increased from 30 % up to 33 %. In addition, an excellent agreement between experimental and numerical results could be achieved. Furthermore, with the advanced long-pulse gyrotron the low frequency oscillations could be suppressed by the renunciation of the alignment probes in the cavity.

7.2 Experimental results with the optimized conventional magnetron injection gun

In the second verification step, the advanced conventional MIG, presented in Section 3.1 and published by I. Gr. Pagonakis et al. [63], has been installed in order to extent the pulse length. With the installation of the advanced conventional MIG a significant more symmetric electron beam could be demonstrated without the generation of trapped electrons. As a result, a gyrotron output power of >2.0 MW with an overall efficiency of 50 % could be achieved.

Alignment and conditioning of the gyrotron

For an operation at high output power levels and efficiencies, the procedure of the gyrotron conditioning, alignment of the insert and measurement of the electron beam homogeneity, as described in Section 6.3, have to be repeated. The insert alignment measurements, presented in Fig. 7.3, have shown an insert misalignment of 36 μm in the x-plane and 32 μm in the y-plane, which is below the maximum misalignment of 100 μm [41]. Compared to the symmetry analysis of the old short-pulse MIG (Fig. 6.4), the measured insert current emitted from the new emitter, presented in Fig. 7.3, indicates a significantly more expected electron emission behavior. Especially in the flat top region, the insert current is close to 0 mA. With increasing absolute amount of the dipole current a very steep flank of the insert current can be observed, which is also an indication for an electron beam of high quality and without an electron emission from the rims. These measurements were performed at a beam current of 0.3 A and a cathode voltage of 3.7 kV. The quality of the electron beam as well as the homogeneity of the electron beam can be additionally determined by

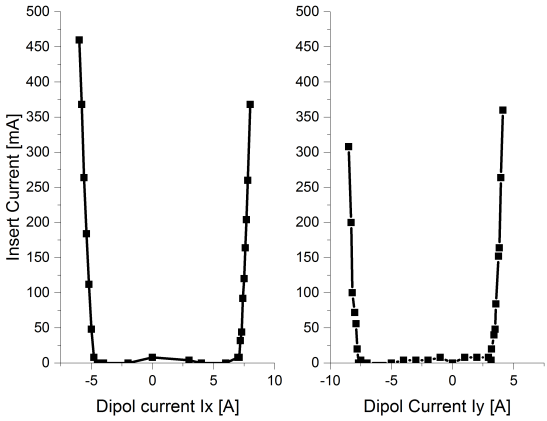

Figure 7.3: Investigations of the insert alignment and homogeneity of the electron beam.

the measurement of the Current-Voltage characteristic (CVC) [45], as shown in Fig. 7.4. This measurement was performed with a filament current of 18 A and shows a sharp transition between space charge limited operation and temperature limited operation at a voltage of 6.7 kV and a beam current of 8.67 A. The transition point is very sharp, which is an indication for a homogeneous electron beam of high quality [45].

Triode start-up scenario

In Fig. 7.5 the main measurement parameters, cathode and body voltage as well as the beam and body current are presented during a test pulse. The cathode voltage is ramped-up to the nominal operation voltage in 100 µs. At the beginning of the cathode ramp-up the anode has already reached the desired value. This start up process is necessary to prevent reflected electrons during the ramp up due to a high pitch factor of the emitted electrons. It can be seen that the pulse with a pulse length of 13 ms was successful without arcing and discharges. However, it can be observed that during the pulse the beam current decreases by ΔI_b = 12 A, which is 21 % of the total beam current. Further investigations have shown, that this effect is depending on the filament current

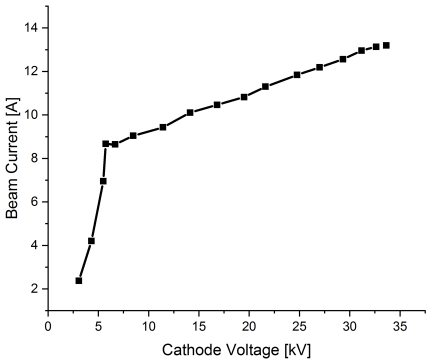

Figure 7.4: Current Voltage characteristics (CVC) of the new Coaxial Magnetron Injection Gun.

and the corresponding emitter surface temperature. However, this issue can not be addressed to the cooling caused by emission. This effect happens in the frame of several seconds [93]. The explanation of such an effect is very difficult because the emitter technology is a confidential. However, one of the

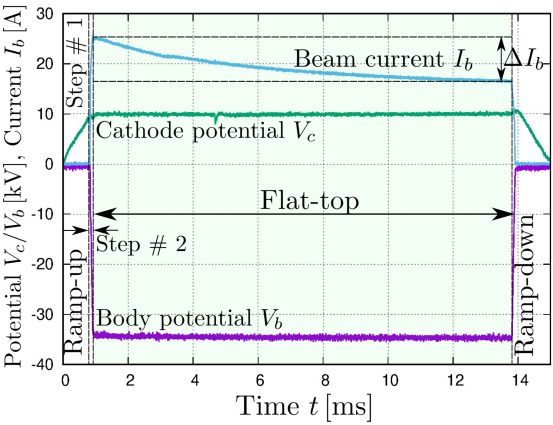

Figure 7.5: Cathode and body voltage, beam current and body current during a pulse [63].

most promising reason could be the voltage induced desorption in the emitter. Here, a lot of BaO is leaving the emitter at the beginning of the pulse and BaO cannot flow back to the surface so fast. As a result, the density of BaO is significantly reducing during the time, which leads to a reduction of the beam current. Based on discussions, this effect is increasing with increasing temperature of the emitter surface, which can be validated by the experimental investigation.

Advanced start-up scenario

However, the decrease in the beam current can be significantly reduced by increasing the ramp-up time of the cathode. In Fig. 7.6 an optimized ramp-up scheme is presented, which is reducing the current drop from 12 A down to 2 A. In this ramp-up scenario the cathode is reaching the nominal voltage after 3 ms. The advantage of the slow ramp is that the current drop can be significantly reduced, which is also an indication for a voltage induced desorption. It has to be mentioned that in with the advanced start-up scenario a very stable operation for the nominal $TE_{34,19}$ mode could be achieved.

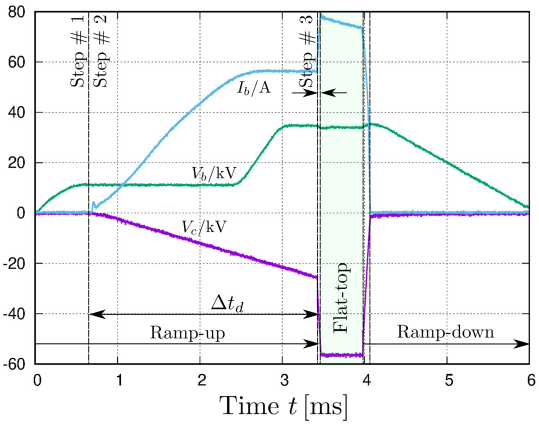

Figure 7.6: Modified ramp-up scenario for a reduced beam current drop [63].

Investigations of the electron beam radius versus the body current

A very strong correlation between the beam radius and the body current has been observed during the experimental campaign. As shown in Fig. 7.7 the body current is increasing with increasing radius of the electron beam in the cavity. With a beam radius of 10.4 mm and a body voltage (depression voltage) of 22 kV the body current exceeds the maximum limit of 200 mA. The reason for the very high body current is the very close distance between the electron beam and the ceramic shielding of the collector. The simulated distance of 22 mm should be sufficient, however, due to stray magnetic fields, the distance in the experiment is less. This issue can be solved by pushing the electron beam with an additional collector coil in positive z-direction. The set-up of the collector coil can be seen in Fig. 7.8.

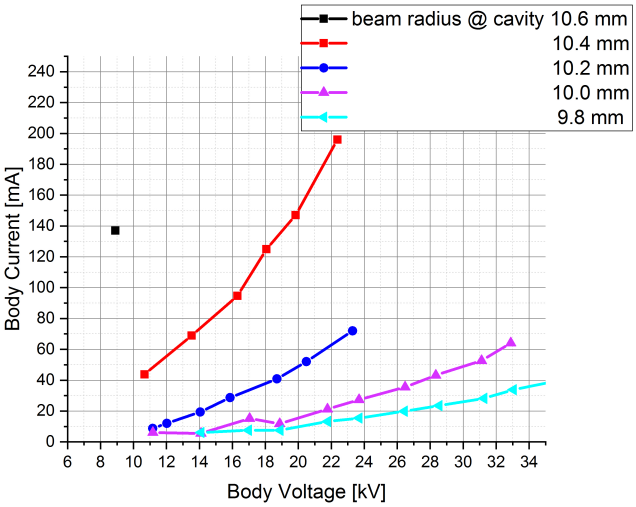

Figure 7.7: Correlation between the body current and the radius of the electron beam in the cavity.

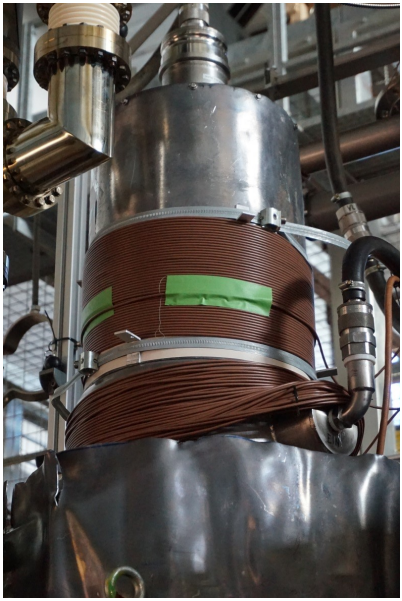

Figure 7.8: Additional collector coil for solving the limitation of the high body current.

Investigations of the collector sweeping

With the implementation of an additional collector coil, the electron beam is moving upwards [119]. Also, the measurement of the body current indicates a significant improvement. During operation without the collector coil, the body current exceeds a value of 150 mA, as shown in Fig. 7.9 and is reducing with increasing collector coil current. At 25 A of coil current the body current is 35 mA. The coil temperature at 25 A reaches in CW operation a maximum temperature of 35 °C, which is below the maximum allowable temperature of the cable.

Experimental verification at nominal beam parameters

After solving the issue with the significant beam drop and body current, the beam parameters could be increased to the nominal parameters (acceleration

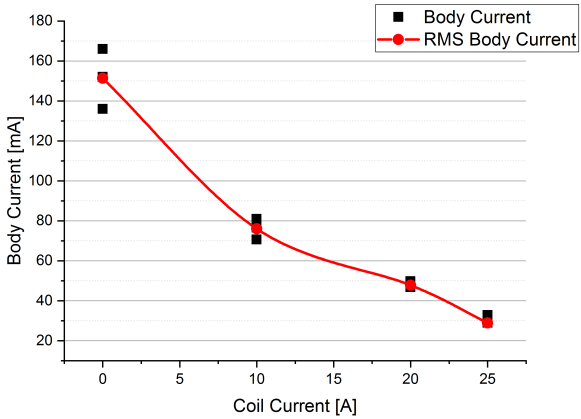

Figure 7.9: Reduction of the body current can be achieved with increasing collector coil current.

voltage of 90 kV and beam current 75 A). A typical start up scenario of the coaxial cavity-long pulse gyrotron with the advanced conventional MIG with coated emitter edges is shown in Fig. 7.10. The power and efficiency is increasing with increasing acceleration voltage. For all the measurement points, the depression voltage is 34 kV with a beam current in the range between 75.35 A and 76.59 A. In this measurement, the beam radius is 10.15 mm with a magnetic field angle at the emitter of - 2 deg. The maximum output power of 2.0 MW was achieved with an acceleration voltage of 90.43 kV and a beam current of 75.35 A. It has to be figured out, that the presented RF output power is only the power in the flat top region (compare Fig. 7.6). The experimentally measured RF power is determined in two steps. In a first pulse, the RF power of the whole pulse is measured. In a second pulse, the RF power is only measured in the ramp-up phase. The subtraction of both pulses delivers the RF power in the flat top region. Due to the decreasing beam current during a pulse, the measured power is an average power. If the beam current would be constant in the flat top region, a significantly higher average power and efficiency can be expected. The position of the gyrotron in the bore hole of the superconducting magnet has been further improved. A maximum output power in depressed operation of 2.2 MW with an efficiency in the 2 MW

gyrotron class of 50 % has been achieved. This excellent operational point has been obtained with a magnetic field density in the cavity of 6.86 T, a cathode voltage of V_c = - 55.27 kV, a body voltage of V_b = 34.26 kV and a beam current of I_b = 74.1 A. The measured pulse length was 0.374 ms. The body current was I_{body} = 106.4 mA. The magnetic field angle at the emitter was -2 deg with an electron beam radius in the cavity of 10.00 mm. Furthermore, it has to be highlighted that the low frequency oscillations, which occurred in the short-pulse coaxial-cavity gyrotron, could be successfully suppressed.

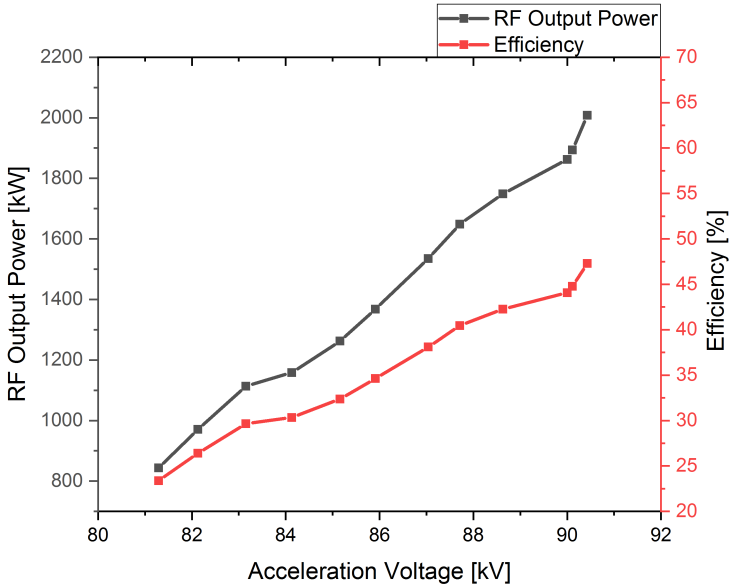

Figure 7.10: Start-up scenario of the coaxial-cavity long pulse gyrotron equipped with the advanced conventional MIG. The body voltage is 34.1 kV, the average beam current is 76 A.

7.3 Summary

First experimental results of the long-pulse gyrotron were presented in this chapter. In a first run the coaxial-cavity long-pulse gyrotron was experimentally verified with the pre-prototype short-pulse coaxial-cavity Magnetron Injection Gun. The experimental results, performed in frame of this work, have shown the excellent performance and world leading capability of the gyrotron with an output power of 2.2 MW at 169.89 GHz. The measured interaction efficiency in non-depressed operation is 33 %, which is 4 % higher compared to the short-pulse coaxial-cavity gyrotron. The experimental results match the analytically simulated predictions. Furthermore, the new conventional MIG with coated emitter rims was experimentally tested in frame of this work. With an advanced start-up scenario an output power >2.0 MW with a total gyrotron efficiency of 50 % in depressed operation could be achieved.

8 Conclusion

8.1 Summary

The available KIT 2 MW 170 GHz short-pulse coaxial-cavity gyrotron has been upgraded to a DEMO relevant coaxial-cavity design up to a pulse length of 150 ms. This coaxial-cavity long-pulse gyrotron has been designed, in-house manufactured and tested in frame of this work. In the current configuration, this gyrotron establishes a new state-of-the-art in the field of multi-MW fusion gyrotrons.

As a first step, two advanced Magnetron Injection Guns were developed, which satisfy the gun design criteria for a stable gyrotron operation. First, a conventional MIG with coated emitter edges was designed and manufactured by Thales. By implementing an emitter with coated edges, the sensitivity regarding manufacturing tolerances and thermal expansions could be significantly reduced. In addition, an advanced DEMO relevant diode configuration for this cathode was proposed in this work. For the first time, a diode design was presented which satisfies all the gun design criteria at all. Furthermore, investigations have shown that the conventional MIG design is strongly limited for an operation at higher power levels. Therefore, an innovative inverse Magnetron Injection Gun has been developed for the 2 MW 170 GHz coaxial-cavity gyrotron. The inverse approach, proposed in this work, offers the possibility for an implementation of a 16.8 % larger emitter by keeping the same outer MIG diameter. Even more, due to the preferable cooling conditions, the cathode temperature of thermally loaded regions could be reduced by a factor of 5 compared to conventional MIGs. Considering the fundamental beam parameters, an excellent beam quality has been achieved in numerical simulation. Electron trapping mechanisms can be successfully suppressed with the unique inverse MIG design.

In addition to the compact inverse MIG proposed for the 2 MW 170 GHz coaxial-cavity long pulse gyrotron, a systematic study was performed in this

work in order to determine the minimum possible MIG dimensions under the consideration of realistic magnetic field profiles and current densities. With this design, the diameter of the gyrotron can be reduced by 25 %, which allows to use a smaller warm bore hole of the superconducting magnet and thus reduces significantly the costs.
A main cost driver in the manufacturing of a long-pulse gyrotron is the brazing and welding of vacuum compatible joints. Therefore, a cost-efficient and KIT internally negotiable joining procedure was developed. The nickel-base super alloy braze has significant advantages over the standard copper-gold and silver braze. The main advantage is the easier handling without the use of reducing gases during the preparation of the components for brazing. Even more, the use of a nickel-base super alloy braze reduces significantly the handling time and costs by 98 % with a success rate of 100 %.
For long-pulse operation all gyrotron sub-components were equipped with efficient cooling systems to increase the RF pulse length. All the components are equipped with a separate cooling system, which offers the possibility to monitor the losses of each component. Thermomechanical studies and Computational Fluid Dynamic investigations (CFD) were performed to identify critical thermally loaded hot spots. Based on the simulation results, the optimum material combination was determined and implemented in the advanced long-pulse gyrotron. Up to a pulse-length of 150 ms the components can be cooled by an annular gap cooling. Thermomechanical simulations have shown, that the maximum permissible temperature of 250 °C is exceeded after 150 ms. In order to increase the pulse-length, an advanced minichannel cooling system has been developed. The minichannel cooling approach offers the possibility to operate the gyrotron at CW operation with a maximum surface temperature of 210 °C. Furthermore, the temperature could be reduced by 15 % compared to the Raschig-ring cooling approach, which is used in today's Thales fusion gyrotrons. Furthermore, for the very first time, an advanced spray cooling system was design and experimentally verified using a mock-up for the cooling of extremely high loaded gyrotron components like cavity and collector. The cooling shows excellent performance properties with a theoretical heat transfer coefficient, which is ten times higher compared to the minichanel cooling approach. The enormous cooling potential and advantages of the exploitation of the high evaporation enthalpy could be approved in the experiment. This cooling method is the key for a future fusion multi-MW gyrotron with the possibility of operation at lower order and more stable modes.
An extended study of the first experimental results is presented in Chapter 7.

In a first run the coaxial-cavity long-pulse gyrotron was experimentally verified with the pre-prototype short-pulse coaxial-cavity Magnetron Injection Gun. The experimental results have shown the excellent performance and world leading capability of the gyrotron with an output power of 2.2 MW at 169.89 GHz. The measured interaction efficiency in non-depressed operation is 33 %, which is 4 % higher compared to the short-pulse coaxial-cavity gyrotron. The experimental results match the analytically simulated predictions.

8.2 Outlook

All topics contained in the work have potential for further development and improvements. In the following, only the obvious hardware optimizations for the coaxial-cavity long-pulse gyrotron, the advanced Magnetron Injection Gun as well as the advanced cooling systems will be discussed.

Coaxial-Cavity Long-Pulse Gyrotron

In its current version, the coaxial-cavity long-pulse gyrotron has been operated with a pulse length up to 15 ms at reduced beam parameters. At pulses up to 2 ms the gyrotron shows excellent performance. However, the tube outgasing is getting stronger with increasing pulse length. Therefore, it is proposed to bake-out the gyrotron again in the oven at 300°C. The bake-out time should be chosen in such a way, that the vacuum pressure is below 10^{-9} mbar at the bake-out temperature of 300 °C. Therefore, it is necessary to replace all the sealing's by Helicoflex or CF-sealing.
A further limitation for longer pulses is the body current of 80 mA to the ceramic shielding of the collector at nominal beam parameters. Therefore, the installation of a defined collector coil is mandatory to push the electron beam in the collector upwards in order to decrease the body current. At the same time, the position of the collector should be moved downwards in order to increase the spacing between the electron beam and the collector ceramic shielding. For this, the thickness of the adapter between collector and mirror box must be reduced by 10 mm.

Advanced Magnetron Injection Guns

The Inverse Magnetron Injection Gun was theoretically deeply investigated and then manufactured. The gained knowledge know-how is fundamental for future Magnetron Injection Guns. A significant improvement of the inverse Magnetron Injection Gun would be an alignment system of the emitter from the outside. This can be easily implemented due to the outside laying cathode. By reason of delivery delays the inverse MIG could not be tested in this frame. Therefore, the inverse MIG should be tested in the coaxial-cavity long-pulse gyrotron at the nominal operating parameters.
The conventional Magnetron Injection Gun with coated emitter edges is currently operating in triode configuration. For a precise statement about the emitter condition the conventional MIG should be tested in diode configuration, which was already proposed. In this connection, the current characteristic can be further investigated without the unknown behavior of triode MIGs. As already mentioned, the most promising reason for the significant current drop is the voltage induced disruption of BaO at the emitter. This assumption could be underlined by an SEM (Scanning Electron Microscope) measurement of the content of BaO at the emitter surface and the neighboring regions.

Advanced Cooling Systems

In this work, the enormous potential of minichannel and spray cooling have been shown. However, further systematic studies should be performed to optimize the designs. The absorbed power in both mock-up device is currently 10 % of that of a real cavity. The absorption can be significantly improved by increasing the cavity surface. This can be done by the implementation of fins made of copper. Measurement of the gradient in the mock-ups was a very difficult task, because the thermal conductivity is high and therefore the heat transfer coefficient of the cooling approaches could not be investigated. The replacement of the copper cavity with a cavity made of stainless steel would make the determination of the heat transfer coefficient possible due to the lower thermal conductivity and the higher radial temperature gradient in the cavity wall. The experimental test with the spray cooling were performed at ambient pressure. The evaporation enthalpy can be increased if the pressure in the cooling chamber is reduced to 33 mbar, which can be achieved with an industrial water-ring-pump. Here, a further cooling gain of 8 % can be achieved.

A Appendix

A.1 Magnetic mirroring

The mirror effect is a very important effect, which has to be taken into account during the development of a MIG. The mirror effect is responsible for the generation of trapped electrons and the resulting halo electrons of the beam. In addition to the discussions in Sec. 3.2.2 the mathematical derivation will be presented following. The derivation is based on [120].

Gyrating particles (e.g. electrons, ions) compose an electric current with a magnetic dipole moment:

$$\mu = \frac{1/2mv_{\perp}^2}{B} \tag{A.1}$$

The dipole moment μ is constant, if B varies locally or temporally (1st adiabatic invariant). If the magnetic flux density B varies, the perpendicular velocity $v_{\perp}$ varies and keeps the dipole moment constant. Due to the conservation of energy the parallel velocity component $v_{\parallel}$ also changes. Considering a B-field in z-direction with varying magnitude and axis symmetry, $B_{\Theta} = 0$ and d/d_{Θ}=0, it can be assumed as cylindrical symmetric. Therefore, it can be written as $B = B_r\widehat{r} + B_z\widehat{r}$. B_r can be obtained from $\nabla\cdot$ B = 0. In cylindrical polar coordinates [120]:

$$\frac{1}{3}\frac{\partial}{\partial r}(rB_r) + \frac{\partial B_z}{\partial z} = 0 \Rightarrow \frac{\partial}{\partial r}(rB_r) = -r\frac{\partial B_z}{\partial z} \tag{A.2}$$

If $\partial B_z/\partial z$ is given at r=0 and does not vary with r, then [120]

$$rB_r = -\int_0^r r\frac{\partial B_z}{\partial z}dr \approx -\frac{1}{2}r^2\left(\frac{\partial B_z}{\partial z}\right)_{r=0} \tag{A.3}$$

$$B_r = -\frac{1}{2} r \left(\frac{\partial B_z}{\partial z} \right)_{r=0} \tag{A.4}$$

The field component B_z has a contribution to the Lorentz force [120].

$$F_r = q \left(v_\Theta B_z - v_z B_\Theta \right) \tag{A.5}$$

$$F_\Theta = q \left(-v_r B_z - v_z B_\Theta \right) \tag{A.6}$$

$$F_z = q \left(v_r B_\Theta - v_\Theta B_r \right) \tag{A.7}$$

With B_Θ=0, two terms vanish.

$$F_z = -q v_\Theta B_r = \frac{q v_\Theta B_r}{2} \frac{\partial B_z}{\partial z} \tag{A.8}$$

Averaging over one gyro orbit, and using $v_\Theta = \pm v_\perp$ and $r = r_L$ [120].

$$F_z = \pm \frac{1}{2} \frac{q v_\perp r_L}{\omega_c} \frac{\partial B_z}{\partial z} \tag{A.9}$$

This force is the so called mirror force, in which -/+ indicates the direction of the field in opposite direction regarding the particle charge. It is normally written [120]:

$$F_z = \pm \frac{1}{2} q \frac{v_\perp^2}{\omega_c} \frac{\partial B_z}{\partial z} \tag{A.10}$$

Or as an alternative

$$F_z = -\mu \frac{\partial B_z}{\partial z} \tag{A.11}$$

with $\mu = \frac{1/2 m v_\perp^2}{B}$ magnetic moment. In the 3-dimensional case, it can be written as [120]:

$$f_\perp = -\mu \frac{dB}{ds} = -\mu \nabla_\parallel B \tag{A.12}$$

where $F_{\parallel}$ the mirror force is parallel to B and ds is a line element along B.

If a charged particle moves into a nonuniform magnetic field, the Larmor radius is changing. However, the magnetic moment μ remains invariant. In order to prove this, the component of equation of motion along the magnetic field is [120]:

$$m\frac{dv_{\parallel}}{dt} = -\mu\frac{dB}{ds} \tag{A.13}$$

Multiplying with $v_{\parallel}$:

$$mv_{\parallel}\frac{dv_{\parallel}}{dt} = -\mu v_{\parallel}\frac{dB}{ds} \tag{A.14}$$

$$\frac{d}{dt}\left(\frac{1}{2}mv_{\parallel}^2\right) = \frac{ds}{dt}\frac{dB}{ds} = -\mu\frac{dB}{dt} \tag{A.15}$$

The energy conservation has to be fulfilled, so

$$\frac{d}{dt}\left(\frac{1}{2}mv_{\parallel}^2 + \frac{1}{2}mv_{\perp}^2\right) = 0 \tag{A.16}$$

with $\mu = \frac{1/2mv_{\perp}^2}{B}$

$$\frac{d}{dt}\left(\frac{1}{2}mv_{\parallel}^2+\right) = 0 \tag{A.17}$$

$$-\mu\frac{dB}{dt} + \frac{d}{dt}(\mu B) = 0 \tag{A.18}$$

$$-\mu\frac{dB}{dt} + \mu\frac{dB}{dt} + B\frac{d\mu}{dt} = 0 \tag{A.19}$$

$$B\frac{d\mu}{dt} = 0 \tag{A.20}$$

While B is not equal to 0, that means,

$$\frac{d\mu}{dt} = 0 \tag{A.21}$$

The result is, that the magnetic moment is constant in time (invariant) and describes the first adiabatic invariant of the particle orbit [120]. If a particle travels from a weak into an increasing magnetic field B. Accordingly, the transverse velocity $v_\perp$ is increasing in order to keep the magnetic moment constant. Due to energy conservation, the parallel velocity component $v_\parallel$ is decreasing. For significantly increase of B the parallel velocity eventually goes to 0 and the particle is reflected back to weaker field regions. This effect is called mirror effect and is also present in Magnetron Injection Guns. Due to the fact that the magnetic moment is constant, it is essential for two different positions

$$\mu(1) - \mu(2) = 0 \tag{A.22}$$

The larmor radius is following defined:

$$r_L = \frac{v_{\perp_e}}{qB} \tag{A.23}$$

with

q : elementary electron charge

m_e Electron mass

It can be written as

$$\frac{r_{L,1}^2 q^2 B_1}{2m_e} - \frac{r_{L,2}^2 q^2 B_2}{2m_e} = 0 \tag{A.24}$$

$$r_{L,1}^2 B_1 = r_{L,2}^2 B_2 \tag{A.25}$$

It describes the correlation of the larmor radius and the magnetic field strength. The Larmorradius in can be replaced by the electron beam radius r_b. The obtained relation is established as the so called Busch-Theorem.This correlations is an important tool for the design of a Magnetron Injection Gun.

Bibliography

[1] Max-Planck-Institut für Plasmaphysik, "Was ist Kernfusion?" 2018. [Online]. Available: https://www.ipp.mpg.de/ippcms/de/pr/fusion21

[2] A. Einstein, "Über die vom Relativitätsprinzip geforderte Trägheit der Energie," *Ann. Phys. (Berlin, Ger.)*, vol. 328, no. 7, pp. 371–384, 1907. [Online]. Available: https://onlinelibrary.wiley.com/doi/abs/10.1002/andp.19073280713

[3] J. Shultis and R. Faw, *Fundamentals of Nuclear Science and Engineering*, third edition ed. Taylor & Francis, 2017.

[4] M. V. Kartikeyan, E. Borie, and M. K. A. Thumm, *Gyrotrons: High Power Microwave and Millimeter Wave Technology*, ser. Advanced Texts in Physics. Berlin and Heidelberg: Springer, 2004. [Online]. Available: http://dx.doi.org/10.1007/978-3-662-07637-8

[5] V. Erckmann, P. Brand, H. Braune, G. Dammertz, G. Gantenbein, W. Kasparek, H. P. Laqua, G. Michel, and M. Thumm, "The 10 MW, CW ECRH system for W7-X: status and first integrated tests," *AIP Conf. Proc.*, vol. 787, no. 1, pp. 371–378, 2005. [Online]. Available: https://doi.org/10.1063/1.2098260

[6] T. Omori, M. A. Henderson, F. Albajar, S. Alberti, U. Baruah, T. S. Bigelow, B. Beckett, R. Bertizzolo, T. Bonicelli, A. Bruschi, J. B. Caughman, R. Chavan, S. Cirant, A. Collazos, D. Cox, C. Darbos, M. R. de Baar, G. Denisov, D. Farina, F. Gandini, T. Gassmann, T. P. Goodman, R. Heidinger, J. P. Hogge, S. Illy, O. Jean, J. Jin, K. Kajiwara, W. Kasparek, A. Kasugai, S. Kern, N. Kobayashi, H. Kumric, J. D. Landis, A. Moro, C. Nazare, Y. Oda, I. Pagonakis, B. Piosczyk, P. Platania, B. Plaum, E. Poli, L. Porte, D. Purohit, G. Ramponi, S. L. Rao, D. A. Rasmussen, D. Ronden, T. Rzesnicki, G. Saibene, K. Sakamoto, F. Sanchez, T. Scherer, M. A. Shapiro, C. Sozzi, P. Spaeh, D. Strauss, O. Sauter, K. Takahashi, R. J. Temkin, M. Thumm, M. Q. Tran, V. S. Udintsev, and H. Zohm,

"Overview of the ITER EC H&CD system and its capabilities," *Fusion Eng. Des.*, vol. 86, no. 6-8, pp. 951–954, 2011. [Online]. Available: https://doi.org/10.1016/j.fusengdes.2011.02.040

[7] H. Zohm, C. Angioni, E. Fable, G. Federici, G. Gantenbein, T. Hartmann, K. Lackner, E. Poli, L. Porte, O. Sauter, G. Tardini, D. Ward, and M. Wischmeier, "On the physics guidelines for a tokamak DEMO," *Nucl. Fusion*, vol. 53, no. 7, p. 073019, 2013. [Online]. Available: https://doi.org/10.1088%2F0029-5515%2F53%2F7%2F073019

[8] EUROfusion, "The demonstration power plant: Demo," 2018. [Online]. Available: https://www.euro-fusion.org/programme/demo/

[9] G. Federici, R. Kemp, D. Ward, C. Bachmann, T. Franke, S. Gonzalez, C. Lowry, M. Gadomska, J. Harman, B. Meszaros, C. Morlock, F. Romanelli, and R. Wenninger, "Overview of EU DEMO design and R&D activities," *Fusion Eng. Des.*, vol. 89, no. 7-8, pp. 882–889, 2014. [Online]. Available: https://doi.org/10.1016/j.fusengdes.2014.01.070

[10] J. Jelonnek, G. Aiello, S. Alberti, K. Avramidis, F. Braunmueller, A. Bruschi, J. Chelis, J. Franck, T. Franke, G. Gantenbein, S. Garavaglia, G. Granucci, G. Grossetti, S. Illy, Z. C. Ioannidis, J. Jin, P. Kalaria, G. P. Latsas, I. Pagonakis, T. Rzesnicki, S. Ruess, T. Scherer, M. Schmid, D. Strauss, C. Wu, I. Tigelis, M. Thumm, and M. Q. Tran, "Design considerations for future DEMO gyrotrons: A review on related gyrotron activities within EUROfusion," *Fusion Eng. Des.*, vol. 123, pp. 241–246, 2017. [Online]. Available: https://doi.org/10.1016/j.fusengdes.2017.01.047

[11] T. Franke, K. Avramidis, J. Jelonnek, G. Granucci, M. Kalsey, J.-M. Noterdaeme, A. Simonin, P. Sonato, and M. Q. Tran, "On the present status of the EU DEMO H&CD systems, technology, functions and mix," in *IEEE 26th Symposium on Fusion Engineering (SOFE)*, 2015, pp. 1–6. [Online]. Available: https://doi.org/10.1109/SOFE.2015.7482410

[12] T. Franke, E. Barbato, A. Cardinali, S. Ceccuzzi, R. Cesario, D. V. Eester, E. Lerche, M.-L. Mayoral, F. Mirizzi, M. Nightingale, J.-M. Noterdaeme, E. Poli, A. A. Tuccillo, R. Wenninger, and H. Zohm, "RF H&CD systems for DEMO - challenges and opportunities," ser. AIP Conf. Proc. American Institute of Physics, 2014, pp. 207–210. [Online]. Available: https://doi.org/10.1063/1.4864524

[13] G. Federici, C. Bachmann, L. Barucca, W. Biel, L. Boccaccini, R. Brown, C. Bustreo, S. Ciattaglia, F. Cismondi, M. Coleman, V. Corato, C. Day, E. Diegele, U. Fischer, T. Franke, C. Gliss, A. Ibarra, R. Kembleton, A. Loving, F. Maviglia, B. Meszaros, G. Pintsuk, N. Taylor, M. Tran, C. Vorpahl, R. Wenninger, and J. You, "DEMO design activity in Europe: Progress and updates," *Fusion Eng. Des.*, vol. 136, pp. 729 – 741, 2018, special Issue: Proceedings of the 13th International Symposium on Fusion Nuclear Technology (ISFNT-13). [Online]. Available: https://doi.org/10.1016/j.fusengdes.2018.04.001

[14] P. Kalaria, "Feasibility and operational limits for a 236 GHz hollow-cavity gyrotron for DEMO," Dissertation, Karlsruher Institut für Technologie (KIT), Karlsruhe, 2018. [Online]. Available: http://nbn-resolving.de/urn:nbn:de:0072-735815

[15] G. Dammertz, S. Alberti, D. Bariou, P. Brand, H. Braune, V. Erckmann, G. Gantenbein, E. Giguet, R. Heidinger, J. P. Hogge, W. Kasparek, H. P. Laqua, C. Liévin, W. Leonhardt, G. Michel, G. Müller, G. Neffe, B. Piosczyk, M. Schmid, and M. Thumm, "140 GHz high-power gyrotron development for the stellarator W7-X," *Fusion Eng. Des.*, vol. 74, no. 1-4, pp. 217–221, 2005. [Online]. Available: https://doi.org/10.1016/j.fusengdes.2005.06.067

[16] M. Thumm, S. Alberti, A. Arnold, P. Brand, H. Braune, G. Dammertz, V. Erckmann, G. Gantenbein, E. Giguet, R. Heidinger, J.-P. Hogge, S. Illy, W. Kasparek, H. P. Laqua, F. Legrand, W. Leonhardt, C. Lievin, G. Michel, G. Neffe, B. Piosczyk, M. Schmid, K. Schworer, and M. Q. Tran, "EU megawatt-class 140-GHz CW gyrotron," *IEEE Trans. Plasma Sci.*, vol. 35, no. 2, pp. 143–153, 2007. [Online]. Available: https://doi.org/10.1109/TPS.2007.892144

[17] M. Thumm, G. Denisov, K. Sakamoto, and M. Tran, "High-power gyrotrons for electron cyclotron heating and current drive," *Nucl. Fusion*, vol. 59, no. 7, p. 073001, 2019. [Online]. Available: https://doi.org/10.1088%2F1741-4326%2Fab2005

[18] Z. C. Ioannidis, T. Rzesnicki, K. Avramidis, G. Gantenbein, S. Illy, J. Jin, T. Kobarg, I. G. Pagonakis, M. Schmid, M. Thumm, J. Jelonnek, V. Hermann, Y. Rozier, F. Legrand, S. Alberti, F. Braunmueller, J.-P. Hogge, C. Schlatter, J. Genoud, M. Q. Tran, W. Kasparek, C. Lechte, J. L. Vomvoridis, J. Chelis, G. P. Latsas, A. Zisis, I. G. Tigelis, A. Bruschi, W. Bin, M. Lontano, F. Albajar, T. Bonicelli, and P.-E.

Frigot, “First CW experiments with the EU ITER 1 MW, 170 GHz industrial prototype gyrotron,” in *18th IEEE International Vacuum Electronics Conference (IVEC)*, 2017, pp. 1–2. [Online]. Available: https://doi.org/10.1109/IVEC.2017.8289742

[19] M. Thumm, “Progress on gyrotrons for ITER and future thermonuclear fusion reactors,” *IEEE Trans. Plasma Sci.*, vol. 39, no. 4, pp. 971–979, 2011. [Online]. Available: https://doi.org/10.1109/TPS.2010.2095042

[20] G. Federici, G. Giruzzi, C. Lowry, R. Kemp, D. Ward, R. Wenninger, and H. Zohm, “EU DEMO design and R&D studies,” in *IEEE 25th Symposium on Fusion Engineering (SOFE)*, 2013, pp. 1–8. [Online]. Available: https://doi.org/10.1109/SOFE.2013.6635288

[21] S. Kern, J.-P. Hogge, S. Alberti, K. Avramides, G. Gantenbein, S. Illy, J. Jelonnek, J. Jin, F. Li, I. G. Pagonakis, B. Piosczyk, T. Rzesnicki, M. K. Thumm, I. Tigelis, and M. Q. Tran, “Experimental results and recent developments on the EU 2 MW 170 GHz coaxial cavity gyrotron for ITER,” *EPJ Web Conf.*, vol. 32, no. 2, p. 04009, 2012. [Online]. Available: https://doi.org/10.1051/epjconf/20123204009

[22] T. Rzesnicki, G. Gantenbein, S. Illy, J. Jelonnek, J. Jin, I. G. Pagonakis, B. Piosczyk, A. Schlaich, and M. Thumm, “2 MW, 170 GHz coaxial-cavity short-pulse gyrotron - investigations on electron beam instabilities and parasitic oscillations,” in *38th International Conference on Infrared, Millimeter, and Terahertz Waves (IRMMW-THz)*, 2013, pp. 1–2. [Online]. Available: https://doi.org/10.1109/IRMMW-THz.2013.6665751

[23] S. Ruess, K. A. Avramidis, M. Fuchs, G. Gantenbein, Z. Ioannidis, S. Illy, J. Jin, P. C. Kalaria, T. Kobarg, I. G. Pagonakis, T. Ruess, T. Rzesnicki, M. Schmid, M. Thumm, J. Weggen, A. Zein, and J. Jelonnek, “KIT coaxial gyrotron development: from ITER toward DEMO,” *INT J MICROW WIREL T.*, vol. 10, no. 5-6, pp. 547–555, 2018. [Online]. Available: https://doi.org/10.1017/S1759078718000144

[24] B. Piosczyk, A. Arnold, G. Dammertz, O. Dumbrajs, M. Kuntze, and M. K. Thumm, “Coaxial cavity gyrotron- recent experimental results,” *IEEE Trans. Plasma Sci.*, vol. 30, no. 3, pp. 819–827, June 2002. [Online]. Available: https://doi.org/10.1109/TPS.2002.801557

[25] T. Rzesnicki, B. Piosczyk, S. Kern, S. Illy, A. S. A. Jin, J.and Samartsev, and M. Thumm, “2.2-MW record power of the 170-GHz European

preprototype coaxial-cavity gyrotron for ITER," *IEEE Trans. Plasma Sci.*, vol. 38, no. 6, pp. 1141–1149, 2010. [Online]. Available: https://doi.org/10.1109/TPS.2010.2040842

[26] G. Gantenbein, K. Avramidis, J. Franck, S. Illy, Z. C. Ioannidis, J. Jin, J. Jelonnek, P. Kalaria, I. G. Pagonakis, S. Ruess, T. Rzesnicki, M. Thumm, and C. Wu, "Recent trends in fusion gyrotron development at KIT," *EPJ Web Conf.*, vol. 157, p. 03017, 2017. [Online]. Available: https://doi.org/10.1051/epjconf/201715703017

[27] I. G. Pagonakis, S. Illy, T. Rzesnicki, B. Piosczyk, K. Avramidis, M. Thumm, G. Gantenbein, J. Jelonnek, J.-P. Hogge, and S. Alberti, "A gun design criterion to limit the effects of the electron beam halo in gyrotrons," in *IEEE International Conference on Plasma Science (ICOPS)*, 2013, p. 1. [Online]. Available: https://doi.org/10.1109/PLASMA.2013.6635123

[28] T. Idehara, H. Tsuchiya, O. Watanabe, L. Agusu, and S. Mitsudo, "The first experiment of a THz gyrotron with a pulse magnet," *Int. J. Infrared Millimeter Waves*, vol. 27, no. 3, pp. 319–331, Mar 2006. [Online]. Available: https://doi.org/10.1007/s10762-006-9084-9

[29] A. S. Gilmour, *Klystrons, traveling wave tubes, magnetrons, crossed-field amplifiers, and gyrotrons*, ser. Artech House microwave library. Norwood, MA: Artech House, 2011.

[30] J. Flamm, "Diffraction and scattering in launchers of quasi-optical mode converters for gyrotrons," Ph.D. dissertation, Karlsruher Institut für Technologie (KIT), Karlsruhe, 2012. [Online]. Available: https://doi.org/10.5445/KSP/1000026613

[31] J. Jin, G. Gantenbein, J. Jelonnek, T. Rzesnicki, and M. Thumm, "Development of mode conversion waveguides at KIT," *EPJ Web Conf.*, vol. 87, p. 04003, 03 2015. [Online]. Available: https://doi.org/10.1051/epjconf/20158704003

[32] J. Jin, M. Thumm, B. Piosczyk, S. Kern, T. Rzesnicki, and J. Flamm, "A new method for the design of quasi-optical launchers for high power gyrotrons," in *IEEE International Conference on Plasma Science - Abstracts*, 2009, pp. 1–1. [Online]. Available: https://doi.org/10.1109/PLASMA.2009.5227327

[33] N. S. Ginzburg and G. S. Nusinovich, "On the nonlinear theory of a relativistic gyrotron," *Radiophysics and Quantum Electronics*,

vol. 22, no. 6, pp. 522–528, Jun 1979. [Online]. Available: https://doi.org/10.1007/BF01081232

[34] R. Oak, *Development Program for a 200 KW, CW, 110 GHz Gyrotron*. Oak Ridge National Laboratory, September 1979.

[35] J. Jelonnek, "Untersuchung des lastverhaltens von gyrotrons," Dissertation, TU Hamburg-Harburg, 2000.

[36] M. Beringer, "Design studies towards a 4 mw 170 ghz coaxial-cavity gyrotron," Dissertation, Karlsruher Institut für Technologie (KIT), Karlsruhe, 2011. [Online]. Available: http://dx.doi.org/10.5445/KSP/1000022514

[37] H. Jory, S. Evans, K. Felch, J. Shively, and S. Spang, "Gyrotron oscillators for fusion heating," in *Heating in Toroidal Plasmas 1982*. Pergamon, 1982, pp. 1073 – 1078. [Online]. Available: https://doi.org/10.1016/B978-1-4832-8428-6.50126-0

[38] J. Pagonakis and J. L. Vomvoridis, "The self-consistent 3D trajectory electrostatic code ARIADNE for gyrotron beam tunnel simulation," in *29th International Conference on Infrared and Millimeter Waves JT with the 12th International Conference on Terahertz Electronics*, 2004, pp. 657–658. [Online]. Available: https://doi.org/10.1109/ICIMW.2004.1422262

[39] C. Edgecombe, *Gyrotron oscillators*. London: Taylor & Francis, 1993.

[40] S. Kern, "Numerische Simulation der Gyrotron- Wechselwirkung in koaxialen Resonatoren," Ph.D. dissertation, Forschungszentrum Karlsruhe, 1996. [Online]. Available: https://doi.org/10.5445/IR/55396

[41] J. Franck, "Systematic study of key components for a coaxial-cavity gyrotron for DEMO," Dissertation, Karlsruher Institut für Technologie (KIT), Karlsruhe, 2017. [Online]. Available: https://doi.org/10.5445/KSP/1000068000

[42] A. Schlaich, "Time-dependent spectrum analysis of high power gyrotrons," Dissertation, Karlsruher Institut für Technologie (KIT), 2015. [Online]. Available: http://dx.doi.org/10.5445/KSP/1000046919

[43] A. Schlaich, C. Wu, I. Pagonakis, K. Avramidis, S. Illy, G. Gantenbein, J. Jelonnek, and M. Thumm, "Frequency-based investigation of charge neutralization processes and thermal cavity expansion in gyrotrons," *J. Infrared, Millimeter, Terahertz Waves*, vol. 36, 06 2015. [Online]. Available: https://doi.org/10.1007/s10762-015-0177-1

[44] I. G. Pagonakis, J. P. Hogge, S. Alberti, K. A. Avramides, and B. Piosczyk, "Preliminary numerical study of the beam neutralization effect in the EU 170 GHz, 2 MW coaxial gyrotron," in *IEEE 35th International Conference on Plasma Science*, 2008, pp. 1–1. [Online]. Available: https://doi.org/10.1109/PLASMA.2008.4590838

[45] J. Zhang, "Influence of emitter surface roughness and emission inhomogeneity on efficiency and stability of high power fusion gyrotrons," Dissertation, Karlsruher Institut für Technologie (KIT), Karlsruhe, 2016. [Online]. Available: http://dx.doi.org/10.5445/KSP/1000058566

[46] J. Bretting, Ed., *Technische Röhren: Grundlagen, Funktionen, Anwendung*. Heidelberg: Hüthig, 1991.

[47] J. Eichmeier, *Moderne Vakuumelektronik: Grundlagen, Bauelemente, Technologie*. Berlin u.a.: Springer, 1981.

[48] V. N. Manuilov and S. A. Polushkina, "Behavior of helical electron beams in gyrotrons with high pitch factors," *Radiophys. Quantum Electron.*, vol. 52, no. 10, pp. 714–721, Oct 2009. [Online]. Available: https://doi.org/10.1007/s11141-010-9179-y

[49] S. E. Tsimring, *Electron beams and microwave vacuum electronics*, ser. Wiley series in microwave and optical engineering. Hoboken, NJ [u.a.]: Wiley-Interscience, 2007.

[50] V. E. Zapevalov, A. N. Kuftin, and V. K. Lygin, "Numerical simulation and experimental study of an electron-optical system of a megawatt gyrotron with step frequency tuning in the range 100-170 GHz," *Radiophys. Quantum Electron.*, vol. 50, no. 9, pp. 702–712, 2007. [Online]. Available: https://doi.org/10.1007/s11141-007-0061-5

[51] L. Groening, C. Xiao, and M. Chung, "Extension of busch's theorem to particle beams," *Phys. Rev. Accel. Beams*, vol. 21, no. 1, 2018. [Online]. Available: https://doi.org/10.1103/PhysRevAccelBeams.21.014201

[52] A. Kumar, U. Singh, N. Kumar, N.and Kumar, V. Vyas, and A. K. Sinha, "Design of a triode magnetron injection gun for a 1-MW 170-GHz gyrotron," *IEEE Trans. Plasma Sci.*, vol. 40, no. 9, pp. 2126–2132, 2012. [Online]. Available: https://doi.org/10.1109/TPS.2012.2205710

[53] K. Kajiwara, A. Oda, Y.and Kasugai, K. Takahashi, and K. Sakamoto, "Development of dual-frequency gyrotron with triode magnetron

injection gun," *Appl. Phys. Express*, vol. 4, no. 12, p. 126001, 2011. [Online]. Available: https://doi.org/10.1143/APEX.4.126001

[54] J. C. Rode, M. H. Beringer, S. Illy, S. Kern, B. Piosczyk, and M. Thumm, "Diode and triode type magnetron injection guns for a 4 MW 170 GHz coaxial-cavity gyrotron," in *21st Joint Russian-German Workshop on ECRH and Gyrotrons (STC-Meeting), Greifswald, Germany, May 2009*, 2009.

[55] S. Ruess, I. G. Pagonakis, G. Gantenbein, S. Illy, T. Kobarg, T. Rzesnicki, M. Thumm, J. Weggen, and J. Jelonnek, "An inverse magnetron injection gun for the KIT 2-MW coaxial-cavity gyrotron," *IEEE Trans. Electron Devices*, vol. 63, no. 5, pp. 2104–2109, 2016. [Online]. Available: https://doi.org/10.1109/TED.2016.2540298

[56] V. K. Lygin, V. N. Manuilov, A. N. Kuftin, A. B. Pavelyev, and B. Piosczyk, "Inverse magnetron injection gun for a coaxial 1.5 MW, 140 GHz gyrotron," *Int. J. Electron.*, vol. 79, no. 2, pp. 227–235, 1995. [Online]. Available: https://doi.org/10.1080/00207219508926264

[57] J. Eichmeier and M. Thumm, *Vacuum Electronics: Components and Devices*. Springer-Verlag Berlin Heidelberg, 2008. [Online]. Available: http://site.ebrary.com/lib/alltitles/docDetail.action?docID=10223473

[58] G. Gärtner, "Historical development and future trends of vacuum electronics," *J. Vac. Sci. Technol., B: Nanotechnol. Microelectron.: Mater., Process., Meas., Phenom.*, vol. 30, no. 6, p. 060801, 2012. [Online]. Available: https://doi.org/10.1116/1.4747705

[59] A. S. Gilmour, "A review of: Microwave tubes," *Int. J. Electron.*, vol. 65, no. 3, pp. 733–734, 1988. [Online]. Available: https://doi.org/10.1080/00207218808945271

[60] M. C. Green, H. B. Skinner, and R. A. Tuck, "Osmium-tungsten alloys and their relevance to improved m-type cathodes," *Appl. Surf. Sci.*, vol. 8, no. 1-2, pp. 13–35, 1981. [Online]. Available: https://doi.org/10.1016/0378-5963(81)90004-0

[61] J. A. Becker, "Phenomena in oxide coated filaments," *Phys. Rev.*, vol. 34, no. 10, pp. 1323–1351, 1929. [Online]. Available: https://doi.org/10.1103/PhysRev.34.1323

[62] I. Pagonakis, B. Piosczyk, J. Zhang, S. Illy, T. Rzesnicki, J.-P. Hogge, K. Avramidis, G. Gantenbein, M. Thumm, and J. Jelonnek,

"Electron trapping mechanisms in magnetron injection guns," *PHYS PLASMAS*, vol. 23, no. 2, p. 023105, 2016. [Online]. Available: https://doi.org/10.1063/1.4941705

[63] I. G. Pagonakis, K. Avramidis, G. Gantenbein, S. Illy, Z. Ioannidis, J. Jianbo, P. Kalaria, B. Piosczyk, S. Ruess, T. Ruess, T. Rzesnicki, M. Thumm, and J. Jelonnek, "Design and First Experiments of a Triode Magnetron Injection Gun for the KIT 2 MW 170 GHz Coaxial Cavity Gyrotron," *PHYS PLASMAS*, in press.

[64] Pagonakis, I., Alberti, S., Avramidis, K., Legrand, F., Gantenbein, G., Genoud, J., Hogge, J.-P., Illy, S., Ioannidis, Z., Kalaria, P., Piosczyk, B., Ruess, S., Ruess, T., Rzesnicki, T., Tran, M.-Q., Tran, T.-M., Thumm, M., Vomvoridis, I., and Jelonnek, J., "Overview on recent progress in magnetron injection gun theory and design for high power gyrotrons," *EPJ Web Conf.*, vol. 203, p. 04011, 2019. [Online]. Available: https://doi.org/10.1051/epjconf/201920304011

[65] I. G. Pagonakis, S. Illy, and M. Thumm, "Influence of emitter ring manufacturing tolerances on electron beam quality of high power gyrotrons," *PHYS PLASMAS*, vol. 23, no. 8, p. 083103, 2016. [Online]. Available: https://doi.org/10.1063/1.4959113

[66] R. Advani, J. P. Hogge, K. E. Kreischer, M. Pedrozzi, M. E. Read, J. R. Sirigiri, and R. J. Temkin, "Experimental investigation of a 140-GHz coaxial gyrotron oscillator," *IEEE Trans. Plasma Sci.*, vol. 29, no. 6, pp. 943–950, 2001. [Online]. Available: https://doi.org/10.1109/27.974983

[67] S. W. Doescher, "Infinite square-well potential with a moving wall," *AMER J PHYS*, vol. 37, 12 1969. [Online]. Available: https://doi.org/10.1119/1.1975291

[68] Multiphysics, "User guide," vol. Version 5.4, pp. 75–84, 2018.

[69] S. Ruess, X. Zeng, G. Gantenbein, S. Illy, I. G. Pagonakis, M. Rzesnicki, T.and Thumm, and J. Jelonnek, "Choice of material composition for a high-performance inverted magnetron injection gun," in *16th IEEE International Vacuum Electronics Conference (IVEC)*, 2016, pp. 1–2.

[70] S. Ruess, S. Gantenbein, G.and Illy, T. Kobarg, I. G. Pagonakis, T. Rzesnicki, M. Thumm, J. Weggen, and J. Jelonnek, "Tolerance studies on an inverse magnetron injection gun for a 2-MW 170-GHz coaxial-cavity gyrotron," *IEEE Trans. Electron Devices*,

vol. 64, no. 9, pp. 3870–3876, 2017. [Online]. Available: https://doi.org/10.1109/TED.2017.2723160

[71] S. Ruess, G. Gantenbein, S. Illy, I. G. Pagonakis, T. Rzesnicki, M. Thumm, J. Weggen, and J. Jelonnek, "Towards an 2 MW long-pulse coaxial-cavity gyrotron: Progress on the advanced KIT inverse magnetron injection gun," in *18th IEEE International Vacuum Electronics Conference (IVEC)*, 2017, pp. 1–2. [Online]. Available: https://doi.org/10.1109/IVEC.2017.8289746

[72] T. Ruess, K. A. Avramidis, G. Gantenbein, S. Illy, Z. Ioannidis, P. Kalaria, M. Obermaier, I. G. Pagonakis, S. Ruess, T. Rzesnicki, M. Thumm, and J. Jelonnek, "Considerations on the selection of operating modes for future coaxial-cavity gyrotrons for DEMO," in *11th German Microwave Conference (GeMiC)*, 2018, pp. 283–286. [Online]. Available: https://doi.org/10.23919/GEMIC.2018.8335085

[73] P. C. Kalaria, M. George, S. Illy, K. A. Avramidis, G. Gantenbein, S. Ruess, M. Thumm, and J. Jelonnek, "Multiphysics modeling of insert cooling system for a 170-GHz, 2-MW long-pulse coaxial-cavity gyrotron," *IEEE Trans. Electron Devices*, vol. 66, no. 9, pp. 4008–4015, 2019. [Online]. Available: https://doi.org/10.1109/TED.2019.2928222

[74] G. Dammertz, "Vacuum requirements in high power microwave tubes," *Vacuum*, vol. 46, no. 8-10, pp. 785–788, 1995. [Online]. Available: https://doi.org/10.1016/0042-207X(95)00039-9

[75] H. Schultz, *Electron beam welding*. Cambridge: Woodhead Publishing Ltd, 1994. [Online]. Available: http://search.ebscohost.com/login.aspx?direct=true&scope=site&db=nlebk&db=nlabk&AN=688962

[76] U. Dilthey, *Schweißtechnische Fertigungsverfahren 1:Schweiß- und Schneidtechnologien*, 3rd ed., ser. VDI-Buch, 2006. [Online]. Available: http://dx.doi.org/10.1007/3-540-33154-9

[77] K. Matthes and W. Schneider, *Schweißtechnik: Schweißen von metallischen Konstruktionswerkstoffen*, 6th ed. Hanser, 2016.

[78] J. Kowalewski and J. Szczurek, "Issues in vacuum brazing," in *3rd International Brazing Soldering Conference*, ASM Inernational, Ed., San Antonio, Texas USA, 2006.

[79] M. M. Schwartz, *Brazing*, 2nd ed. Materials Park: ASM International, 2004.

[80] Saxonia, "Technical datasheet braze Tec D 897.1," 2018. [Online]. Available: http://www.saxonia-tm.de/Brazetec/de/datenblaetter/TD_BrazeTec_D_897.1_DE.pdf

[81] Wrought Materials, "Data sheet oxyge-free copper," 1968. [Online]. Available: http://copperalliance.org.uk/uploads/2018/03/data-sheet-a4-cu-of.pdf

[82] Höganäs, "Data sheet Glidcop Al-15," 2013. [Online]. Available: https://www.hoganas.com/globalassets/download-media/sharepoint/brochures-and-datasheets---all-documents/glidcop_al-15.pdf

[83] T. A. Scherer, R. Heidinger, A. Meier, D. Strauss, K. Takahashi, K. Kajiwara, and K. Sakamoto, "Experimental and theoretical thermal analysis of CVD diamond window units for the ITER upper launcher," in *33rd International Conference on Infrared, Millimeter and Terahertz Waves*, 2008, pp. 1–2. [Online]. Available: https://doi.org/10.1109/ICIMW.2008.4665660

[84] J. Jin, M. Thumm, B. Piosczyk, S. Kern, J. Flamm, and T. Rzesnicki, "Novel numerical method for the analysis and synthesis of the fields in highly oversized waveguide mode converters," *IEEE Trans. Microwave Theory Tech.*, vol. 57, no. 7, pp. 1661–1668, 2009. [Online]. Available: https://doi.org/10.1109/TMTT.2009.2021878

[85] T. Ruess, K. A. Avramidis, G. Gantenbein, Z. Ioannidis, S. Illy, F.-C. Lutz, A. Marek, S. Ruess, T. Rzesnicki, M. Thumm, D. Wagner, J. Weggen, and J. Jelonnek, "Computer-controlled test system for the excitation of very high-order modes in highly oversized waveguides," *J. Infrared, Millimeter, Terahertz Waves*, vol. 40, no. 3, pp. 257–268, 2019. [Online]. Available: https://doi.org/10.1007/s10762-018-0566-3

[86] J. Neilson, "Surf3d and TOL: computer codes for design and analysis of high-perfonnance QO launchers in gyrotrons," in *29th International Conference on Infrared and Millimeter Waves JT with the 12th International Conference on Terahertz Electronics*, 2004, pp. 667–668. [Online]. Available: https://doi.org/10.1109/ICIMW.2004.1422267

[87] D. Wagner, M. Thumm, G. Gantenbein, W. Kasparek, and T. Idehara, "Analysis of a complete gyrotron oscillator using the scattering matrix description," *Int. J. Infrared Millimeter Waves*,

vol. 19, no. 2, pp. 185–194, Feb 1998. [Online]. Available: https://doi.org/10.1023/A:1022515506809

[88] A. Bertinetti, F. Albajar, K. A. Avramidis, F. Cau, F. Cismondi, G. Gantenbein, J. Jelonnek, P. C. Kalaria, S. Ruess, T. Rzesnicki, L. Savoldi, and R. Zanino, "Analysis of an actively-cooled coaxial cavity in a 170 GHz 2 MW gyrotron using the multi-physics computational tool MUCCA," *Fusion Eng. Des.*, vol. 146, pp. 74 – 77, 2018. [Online]. Available: https://doi.org/10.1016/j.fusengdes.2018.11.033

[89] K. A. Avramidis, A. Bertinetti, F. Albajar, F. Cau, F. Cismondi, G. Gantenbein, S. Illy, Z. C. Ioannidis, J. Jelonnek, F. Legrand, I. G. Pagonakis, Y. Rozier, T. Rzesnicki, L. Savoldi, M. Thumm, and R. Zanino, "Numerical studies on the influence of cavity thermal expansion on the performance of a high-power gyrotron," *IEEE Trans. Electron Devices*, vol. 65, no. 6, pp. 2308–2315, June 2018. [Online]. Available: https://doi.org/10.1109/TED.2017.2782365

[90] N. Kumar, U. Singh, T. P. Singh, and A. K. Sinha, "Suppression criteria of parasitic mode oscillations in a gyrotron beam tunnel," *Phys Plasmas*, vol. 18, no. 2, p. 022507, 2011. [Online]. Available: https://doi.org/10.1063/1.3554648

[91] I. G. Tigelis, J. L. Vomvoridis, and S. Tzima, "High-frequency electromagnetic modes in a dielectric-ring loaded beam tunnel," *IEEE Trans. Plasma Sci.*, vol. 26, no. 3, pp. 922–930, 1998. [Online]. Available: https://doi.org/10.1109/27.700872

[92] M. Pedrozzi, S. Alberti, J. P. Hogge, M. Q. Tran, and T. M. Tran, "Electron beam instabilities in gyrotron beam tunnels," *PHYS PLASMAS*, vol. 5, no. 6, pp. 2421–2430, 1998. [Online]. Available: https://doi.org/10.1063/1.872918

[93] A. Malygin, "Design and experimental investigation of a second harmonic 20 kW class 28 GHz gyrotron for evaluation of new emitter technologies," Dissertation, Karlsruhe Institut of Technology (KIT), 2016. [Online]. Available: https://doi.org/10.5445/KSP/1000059748

[94] T. Rzesnicki, "Analyse eines neuartigen 1.5 MW, 170 GHz Prototyp-Gyrotrons mit koaxialem Resonator," Dissertation, Universität Karlsruhe, 2007.

[95] G. Gantenbein, G. Dammertz, J. Flamm, S. Illy, S. Kern, G. Latsas, B. Piosczyk, T. Rzesnicki, A. Samartsev, A. Schlaich, M. Thumm,

and I. Tigelis, “Experimental investigations and analysis of parasitic rf oscillations in high-power gyrotrons,” *IEEE Trans. Plasma Sci.*, vol. 38, no. 6, pp. 1168–1177, June 2010. [Online]. Available: https://doi.org/10.1109/TPS.2010.2041366

[96] M. Thumm, T. Rzesnicki, B. Piosczyk, J. Flamm, G. Gantenbein, S. Illy, J. Jin, S. Kern, A. Samartsev, and A. Schlaich, “2.2 MW record power of the 0.17 THz European pre-prototype coaxial-cavity gyrotron for ITER,” in *Proceedings on 2nd Shenzhen International Conference on Advanced Science and Technology (SICAST 2009), Shenzhen, China, November 15-20*, 2009. [Online]. Available: https://doi.org/10.11906/TST.001-020.2010.03.01

[97] I. Sakai, H. Ishimaru, and G. Horikoshi, “Sealing concept of elastic metal gasket Helicoflex,” *Vacuum*, vol. 32, pp. 33–37, 1982. [Online]. Available: https://doi.org/10.1016/S0042-207X(82)80193-0

[98] J.-P. Hogge, T. P. Goodman, S. Alberti, F. Albajar, K. A. Avramides, P. Benin, S. Bethuys, W. Bin, T. Bonicelli, A. Bruschi, S. Cirant, E. Droz, O. Dumbrajs, D. Fasel, F. Gandini, G. Gantenbein, S. Illy, S. Jawla, J. Jin, S. Kern, P. Lavanchy, C. Liévin, B. MarlÉtaz, P. Marmillod, A. Perez, B. Piosczyk, I. Pagonakis, L. Porte, T. Rzesnickl, U. Siravo, M. Thumm, and M. Q. Tran, “First experimental results from the European Union 2-MW coaxial cavity ITER gyrotron prototype,” *Fusion Sci. Technol.*, vol. 55, no. 2, pp. 204–212, 2009. [Online]. Available: https://doi.org/10.13182/FST09-A4072

[99] L. Savoldi, A. Bertinetti, G. F. Nallo, A. Zappatore, R. Zanino, F. Cau, F. Cismondi, and Y. Rozier, “CFD analysis of mini-channel cooling for a gyrotron cavity,” in *26th IEEE Symposium on Fusion Engineering (SOFE)*, 2015, pp. 1–5.

[100] R. Stieglitz, “Private discussion,” 2017.

[101] I. Mudawar, “Assessment of high-heat-flux thermal management schemes,” *IEEE Trans. Compon. Packag. Technol.*, vol. 24, no. 2, pp. 122–141, 2001. [Online]. Available: https://doi.org/10.1109/6144.926375

[102] U. Reiners, “Wärmeübertrag durch Spritzwasserkühlung heißer Oberflächen im Bereich der stabilen Filmverdampfung,” Dissertation, Technische Universität Clausthal, Clausthal, 1987.

[103] W. Müller, *Mechanische Verfahrenstechnik und ihre Gesetzmäßigkeiten*, 2nd ed., ser. Studium. De Gruyter Oldenburg, 2014.

[104] W.-L. Cheng, W.-W. Zhang, H. Chen, and L. Hu, "Spray cooling and flash evaporation cooling: The current development and application," *Renewable Sustainable Energy Rev.*, vol. 55, pp. 614–628, 2016. [Online]. Available: https://doi.org/10.1016/j.rser.2015.11.014

[105] J. Kim, "Spray cooling heat transfer: The state of the art," *Int. J. Heat Fluid Flow*, vol. 28, no. 4, pp. 753–767, 2007. [Online]. Available: https://doi.org/10.1016/j.ijheatfluidflow.2006.09.003

[106] I. Mudawar and K. A. Estes, "Optimizing and predicting CHF in spray cooling of a square surface," *J. Heat Transfer*, vol. 118, no. 3, p. 672, 1996. [Online]. Available: https://doi.org/10.1115/1.2822685

[107] R.-H. Chen, L. C. Chow, and J. E. Navedo, "Optimal spray characteristics in water spray cooling," *Int. J. Heat Mass Transfer*, vol. 47, no. 23, pp. 5095–5099, 2004. [Online]. Available: https://doi.org/10.1016/j.ijheatmasstransfer.2004.05.033

[108] F. Puschmann, "Experimentelle Untersuchung der Spraykühlung zur Qualitätsverbesserung durch definierte Einstellung des Wärmeübergangs," Dissertation, Otto-von-Guericke-Universität Magdeburg, 2003. [Online]. Available: http://dx.doi.org/10.25673/5101

[109] J. Xie, Y. Tan, F. Duan, K. Ranjith, T. Wong, K. Toh, K. Choo, and P. Chan, "Study of heat transfer enhancement for structured surfaces in spray cooling," *Appl. Therm. Eng.*, vol. 59, no. 1, pp. 464 – 472, 2013. [Online]. Available: https://doi.org/10.1016/j.applthermaleng.2013.05.047

[110] E. Martinez-Galvan, R. Anton, J. C. Ramos, and R. Khodabandeh, "Influence of surface roughness on a spray cooling system with r134a. part ii: Film thickness measurements," *Exp. Therm. Fluid Sci.*, vol. 48, pp. 73 – 80, 2013. [Online]. Available: https://doi.org/10.1016/j.expthermflusci.2013.02.010

[111] ——, "Influence of surface roughness on a spray cooling system with r134a. part i: Heat transfer measurements," *Exp. Therm. Fluid Sci.*, vol. 46, pp. 183 – 190, 2013. [Online]. Available: https://doi.org/10.1016/j.expthermflusci.2012.12.010

[112] ——, "Effect of the spray cone angle in the spray cooling with r134a," *Exp. Therm. Fluid Sci.*, vol. 50, pp. 127 – 138, 2013. [Online]. Available: https://doi.org/10.1016/j.expthermflusci.2013.05.012

[113] Y. Y. Hsieh and T. F. Lin, "Evaporation heat transfer and pressure drop of refrigerant r-410a flow in a vertical plate heat exchanger," *J HEAT TRANSFER*, vol. 125, 10 2003. [Online]. Available: https://doi.org/10.1115/1.1518498

[114] S. Ruess, K. A. Avramidis, G. Gantenbein, Z. Ioannidis, S. Illy, P. C. Kalaria, T. Kobarg, I. G. Pagonakis, T. Ruess, T. Rzesnicki, M. Thumm, J. Weggen, and J. Jelonnek, "KIT in-house manufacturing and first operation of a 170 GHz 2 MW longer-pulse coaxial-cavity pre-prototype gyrotron," in *11th German Microwave Conference (GeMiC)*, 2018, pp. 291–294. [Online]. Available: https://doi.org/10.23919/GEMIC.2018.8335087

[115] A. Samartsev, G. Dammertz, G. Gantenbein, J. Jelonnek, S. Illy, and M. Thumm, "Influence of annular beam displacement on the performance of a high-power gyrotron," *IEEE Trans. Plasma Sci.*, vol. 41, no. 4, pp. 872–878, 2013. [Online]. Available: https://doi.org/10.1109/TPS.2013.2248385

[116] Z. Ioannidis, K. Avramidis, G. Gantenbein, S. Illy, J. Jin, T. Kobarg, I. Pagonakis, T. Rzesnicki, M. Schmid, M. Thumm, J. Jelonnek, V. Hermann, Y. Rozier, W. Kasparek, C. Lechte, S. Alberti, F. BraunmÃ¼ller, J. Hogge, C. Schlatter, M. Tran, J. Vomvoridis, J. Chelis, G. Latsas, I. Tigelis, A. Bruschi, M. Lontano, F. Albajar, T. Bonicelli, and P. Frigot, "Recent experimental results with the 1 MW - 170 GHz industrial CW prototype gyrotron for ITER," Workshop on RF Heating Technology of Fusion Plasma (US-EU-JPN), Leinsweiler, September 21-23, 2016, 31.03.02; LK 01.

[117] K. A. Avramidis, G. Aiello, S. Alberti, P. T. BrÃ¼cker, A. Bruschi, I. Chelis, T. Franke, G. Gantenbein, S. Garavaglia, J. Genoud, M. George, G. Granucci, G. Grossetti, J.-P. Hogge, S. Illy, Z. C. Ioannidis, J. Jelonnek, J. Jin, P. C. Kalaria, G. P. Latsas, A. Marek, I. G. Pagonakis, D. V. Peponis, S. Ruess, T. Ruess, T. Rzesnicki, T. Scherer, M. Schmid, D. Strauss, M. Thumm, I. Tigelis, C. Wu, A. Zein, A. Zisis, and M. Q. Tran, "Overview of recent gyrotron R&D towards DEMO within EUROfusion work package heating and

current drive," *Nucl. Fusion*, vol. 59, no. 6, p. 066014, 2019. [Online]. Available: https://doi.org/10.1088/1741-4326/ab12f9

[118] K. A. Avramides, I. G. Pagonakis, C. T. Iatrou, and J. L. Vomvoridis, "EURIDICE: a code-package for gyrotron interaction simulations and cavity design," *EPJ Web Conf.*, vol. 32, p. 04016, 2012. [Online]. Available: https://doi.org/10.1051/epjconf/20123204016

[119] S. Illy, S. Kern, I. Pagonakis, and A. Vaccaro, "Collector loading of the 2-MW, 170-GHz gyrotron for ITER in case of beam power modulation," *IEEE Trans. Plasma Sci.*, vol. 41, pp. 2742–2747, 10 2013. [Online]. Available: https://doi.org/10.1109/TPS.2013.2262607

[120] P. Gallagher, "Introduction to plasma physics," University Lecture, 2017.

List of Figures

Own publications as sole or principal author

List of journal articles

1. S. Garavaglia, G. Aiello, S. Alberti, K. A. Avramidis, A. Bruschi, I. G. Chelis, J. Franck, G. Gantenbein, G. Granucci, G. Grossetti, K. Hizanidis, S. Illy, J. Jelonnek, P. Kalaria, G. Latsas, A. Moro, I. Gr. Pagonakis, D. V. Peponis, E. Poli, N. Rispoli, **S. Ruess**, T. Rzesnicki, T. Scherer, D. Strauss, M. Thumm, I. Tigelis, C. Tsironis, C. Wu, T. Franke, and M.-Q. Tran. EU DEMO EC System Preliminary Conceptual Design. *Fusion Eng. Des.*, 2018.
2. J. Jelonnek, G. Gantenbein, K. A. Avramidis, J. Franck, S. Illy, Z. Ioannidis, J. Jin, P. Kalaria, I. Pagonakis, **S. Ruess**, T. Rzesnicki, T. Scherer, M. Schmid, D. Strauss, C. Wu, and M. Thumm. Gyrotron Forschung und Entwicklung am KIT. *Vakuum in Forschung und Praxis*, 28(6):21-27, 2016.
3. **S. Ruess**, K. A. Avramidis, M. Fuchs, G. Gantenbein, Z. Ioannidis, S. Illy, J. Jin, P. C. Kalaria, T. Kobarg, I. Gr. Pagonakis, T. Ruess, T. Rzesnicki, M. Schmid, M. Thumm, J. Weggen, A. Zein, and J. Jelonnek. KIT Coaxial Gyrotron Development: From ITER toward DEMO. *INT J MICROW WIREL T.*, 10(5): 547-555, 2018.
4. **S. Ruess**, G. Gantenbein, S. Illy, T. Kobarg, I. Gr. Pagonakis, T. Rzesnicki, M. Thumm, J. Weggen, and J. Jelonnek. Tolerance Studies on an Inverse Magnetron Injection Gun for a 2-MW 170-GHz Coaxial-Cavity Gyrotron. *IEEE Trans. Electron Devices*, 64(9):3870-3876, 2017.
5. M. Thumm, K. A. Avramidis, J. Franck, G. Gantenbein, S. Illy, J. Jin, P. C. Kalaria, I. Gr. Pagonakis, **S. Ruess**, C. Wu, and J. Jelonnek. Design Studies and Analysis of Operational Limits of 0.24-THz Gyrotrons for DEMO. *IEEE Trans. Terahertz Sci. Technol.*, 11(1):20, 2017.

6. J. Zhang, S. Illy, I. Gr. Pagonakis, T. Rzesnicki, K. A. Avramidis, A. Malygin, **S. Ruess**, A. Samartsev, G. Dammertz, B. Piosczyk, G. Gantenbein, M. Thumm, and J. Jelonnek. Evaluation and Influence of Gyrotron Cathode Emission Inhomogeneity. *IEEE Trans. Electron Devices*, 64(3):1307-1314, 2017.

List of conference articles

1. G. Gantenbein,K. A. Avramidis, S. Illy, Z. Ioannidis, J. Jin, J. Jelonnek, P. C. Kalaria, I. Gr. Pagonakis, **S. Ruess**, T. Ruess, T. Rzesnicki, M. Thumm, and C. Wu. New trends of gyrotron development at KIT: An overview on recent investigations. *30th International Symposium on Fusion Technology (SOFT 2018)*, Giardini-Naxos, Italien, September, 2018.
2. G. Gantenbein, K. A. Avramidis, S. Illy, Z. C. Ioannidis, J. Jin, J. Jelonnek, P. C. Kalaria, I. Gr. Pagonakis, **S. Ruess**, T. Ruess, T. Rzesnicki, M. Thumm, and C. Wu. Overview of KIT activities on high power, high frequency gyrotron development and the role of the new fulgor teststand at KIT. *7th International Workshop on Far-Infrared Technologies (IW-FIRT 2019)*, Fukui, Japan, March, 2019.
3. S. Illy, M. George, P. C. Kalaria, K. A. Avramidis, G. Gantenbein, **S. Ruess**, M. Thumm, and J. Jelonnek. Thermo-Mechanical Analysis of the Insert Cooling System for a 170 GHz, 2 MW long-pulse Coaxial-Cavity Gyrotron. *In US-EU-Japan RF Heating Technology Workshop*, Shizuoka, Japan, September, 2018.
4. J. Jelonnek, G. Aiello, K. A. Avramidis, J. Franck, G. Gantenbein, G. Grossetti, S. Illy, Z. Ioannidis, J. Jin, P. C. Kalaria, I. Gr. Pagonakis, T. Rzesnicki, **S. Ruess**, T. Scherer, M. Schmid, D. Strauss, M. Thumm, and C. Wu. Towards 240 GHz High Power Fusion Gyrotrons - KIT Research Status. *In 6th International Workshop on Far-Infrared Technologies (IW-FIRT 2917) and 2nd International Symposium on Development of High Power Terahertz Science and Technology (DHP-TST 2017)*, Fukui, Japan, March, 2017.
5. J. Jelonnek, G. Aiello, K. Avramidis, G. Gantenbein, G. Grossetti, S. Illy, Z. C. Ioannidis, J. Jin, P. C. Kalaria, A. Marek, I. Gr. Pagonakis, T. Rzesnicki, **S. Ruess**, T. Ruess, T. Scherer, M. Schmid, D. Strauss, M. Thumm, F. Wilde, C. Wu, and A. Zein. 2018 Status on KIT Gyrotron Activities. *In*

30th Joint Russian-German Meeting on ECRH and Gyrotrons, IAP RAS, Nizhny Novgorod, RUS, June 17-24, 2018.

6. J. Jelonnek, G. Aiello, F. Albajar, S. Alberti, K. A. Avramidis, T. Bonicelli, A. Bruschi, J. Chelis, T. Franke, G. Gantenbein, S. Garavaglia, G. Granucci, G. Grossetti, J.-P. Hogge, S. Illy, Z. C. Ioannidis, J. Jin, P. C. Kalaria, H. P. Laqua, G. P. Latsas, I. Gr. Pagonakis, D. V. Peponis, T. Rzesnicki, **S. Ruess**, T. Ruess, P. Sanchez, T. Scherer, M. Schmid, D. Strauss, M. Thumm, I. Tigelis, M.-Q. Tran, F. Wilde, and C. Wu. 2018 Status of Gyrotron RD for W7-X, TCV, ITER and EU DEMO within Europe. *In US-EU-Japan RF Heating Technology Workshop*, Shizuoka, Japan, September, 2018.
7. J. Jelonnek, G. Aiello, F. Albajar, S. Alberti, K. A. Avramidis, A. Bertinetti, P. T. Brücker, A. Bruschi, I. Chelis, J. Dubray, F. Fanale, D. Fasel, T. Franke, G. Gantenbein, S. Garavaglia, J. Genoud, G. Granucci, J.-P. Hogge, S. Illy, Z. C. Ioannidis, J. Jin, H. Laqua, G. P. Latsas, A. Leggieri, F. Legrand, R. Marchesin, A. Marek, B. Marletaz, M. Obermaier, I. Gr. Pagonakis, D. V. Peponis, **S. Ruess**, T. Ruess, T. Rzesnicki, P. Sanchez, L. Savoldi, T. Scherer, D. Strauss, P. Thouvenin, M. Thumm, I. Tigelis, M.-Q. Tran, F. Wilde, C. Wu, and A. Zisis. From W7-X Towards ITER and Beyond: 2019 Status on EU Fusion Gyrotron Developments. *In 20th International Vacuum Electronics Conference (IVEC 2019)*, Busan, South Korea, April, 2019.
8. P. C. Kalaria, P. T. Brücker, **S. Ruess**, S. Illy, K. A. Avramidis, G. Gantenbein, M. Thumm, and J. Jelonnek. Design Studies of Mini-Channel Cavity Cooling for a 170 GHz, 2 MW Coaxial-Cavity Gyrotron. *In 20th International Vacuum Electronics Conference (IVEC 2019)*, Busan, South Korea, 28. April, 2019.
9. P. C. Kalaria, M. George, S. Illy, K. A. Avramidis, G. Gantenbein, **S. Ruess**, T. Rzesnicki, M. Thumm, and J. Jelonnek. Performance Analysis of an Insert Cooling System for long-pulse Operation of a Coaxial-Cavity Gyrotron. *In 19th International Vacuum Electronics Conference (IVEC 2018)*, Monterey, CA, USA, 2018.
10. P. C. Kalaria, M. George, S. Illy, K. A. Avramidis, G. Gantenbein, **S. Ruess**, M. Thumm, and J. Jelonnek. Numerical Investigation on the Influence of Insert Misalignment on the Insert Loading of a 170 GHz, 2 MW Coaxial-Cavity Gyrotron. *In 6th ITG International Vacuum Electronics Workshop*, Bad Honnef, Germany, September,2018.

11. M. Obermaier, K. A. Avramidis, G. Gantenbein, S. Illy, **S. Ruess**, T. Ruess, M. Thumm, and J. Jelonnek. Numerical Study of very High-Order Volume Modes as possible Alternatives to the TE34,19 Operating Mode of the KIT 2 MW 170 GHz Coaxial Cavity Gyrotron. *In 6th ITG International Vacuum Electronics Workshop*, Bad Honnef, Germany, September, 2018.
12. I. Gr. Pagonakis, K. A. Avramidis, G. Gantenbein, S. Illy, F. Legrand, **S. Ruess**, T. Ruess, T. Rzesnicki, M. Thumm, and J. Jelonnek. Magnetron Injection Gun for the 2 MW 170 GHz Modular Coaxial cavity Gyrotron. *In 43rd International Conference on Infrared, Millimeter and TerahertzWaves (IRMMW THz 2018)*, Nagoya, Japan, September, 2018.
13. I. Gr. Pagonakis, K. A. Avramidis, G. Gantenbein, S. Illy, F. Legrand, **S. Ruess**, T. Ruess, T. Rzesnicki, M. Thumm, and J. Jelonnek. Magnetron Injection Gun for the 2 MW 170 GHz Modular Coaxial Cavity Gyrotron. *In 43rd International Conference on Infrared, Millimeter and TerahertzWaves (IRMMW THz-2018)*, Nagoya, Japan, September, 2018.
14. T. Ruess, K. A. Avramidis, M. Fuchs, G. Gantenbein, S. Illy, Z. Ioannidis, F. C. Lutz, **S. Ruess**, T. Rzesnicki, M. Thumm, D. Wagner, J. Weggen, and J. Jelonnek. 2018 Status on the Measurements Capabilities for Fusion Gyrotrons at KIT. *In 30th Joint Russian-German Meeting on ECRH and Gyrotrons (2018)*, Gorodez, Russia, June, 2018.
15. T. Ruess, K. A. Avramidis, M. Fuchs, G. Gantenbein, S. Illy, F. C. Lutz, A. Marek, **S. Ruess**, T. Rzesnicki, M. Thumm, D. Wagner, J. Weggen, and J. Jelonnek. Towards fully Automated Systems for the Generation of very high order Modes in Oversized Waveguides. *In Terahertz and Microwave Radiation: Generation, Detection and Applications (TERA)*, Nizhny Novgorod, Russia, October, 2018.
16. T.Ruess, K. A. Avramidis, M. Fuchs, G. Gantenbein, S. Illy, **S. Ruess**, T. Rzesnicki, M. Thumm, D. Wagner, J. Weggen, and J. Jelonnek. An advanced highly Automated Test System for the Verification of quasi-optical Gyrotron Components. *In 6th ITG International Vacuum Electronics Workshop*, Bad Honnef, Germany, September,2018.
17. **S. Ruess**, K. Avramidis, G. Gantenbein, S. Illy, I. Gr. Pagonakis, T. Rzesnicki, M. Thumm, and J. Jelonnek. Proposal of an Inverse Magnetron Injection Gun for Future Hollow-Cylindrical-Cavity High Power Gyrotrons. *In 41th International Conference on Infrared, Millimeter and Terahertz Waves (IRMMW)*, Copenhagen, DK, 25 - 30 September, 2016.

18. **S. Ruess**, G. Aiello, G. Gantenbein, M. Gärtner, T. Rzesnicki, T. Scherer, D. Strauss, M. Thumm, J. Weggen, and J. Jelonnek. Application of CVD Diamond Discs in High Power Fusion Gyrotrons and Power Plants. *In DPG-Frühjahrstagung der Sektion Kondensierte Materie gemeinsam mit der EPS, Fachverband Kristalline Festkörper und deren Mikrostruktur*, Berlin, Germany, March 2018.
19. **S. Ruess**, K. A. Avramidis, G. Gantenbein, Z. Ioannidis, S. Illy, P. C. Kalaria, T. Kobarg, I. Gr. Pagonakis, T. Ruess, T. Rzesnicki, M. Thumm, J. Weggen, and J. Jelonnek. KIT In-House Manufacturing and First Operation of a 170 GHz 2 MW longer-pulse Coaxial-Cavity pre-prototype Gyrotron. *In 11th German Microwave Conference (GeMiC 2018)*, Freiburg, Germany, March, 2018.
20. **S. Ruess**, K. A. Avramidis, G. Gantenbein, Z. Ioannidis, S. Illy, P. C. Kalaria, T. Kobarg, I. Gr. Pagonakis, T. Ruess, T. Rzesnicki, M. Thumm, J. Weggen, and J. Jelonnek. Current Status of the KIT Coaxial-Cavity long-pulse Gyrotron and its Key Components. *In 30th Joint Russian-German Meeting on ECRH and Gyrotrons*, IAP RAS, Nizhny Novgorod, RUS, June , 2018.
21. T. Ruess, K. A. Avramidis, G. Gantenbein, S. Illy, Z. Ioannidis, P. Kalaria, M. Obermaier, I. Gr. Pagonakis, **S. Ruess**, T. Rzesnicki, M. Thumm, and J. Jelonnek. Considerations on the Selection of Operating Modes for Future Coaxial-Cavity Gyrotrons for DEMO. *In 11th German Microwave Conference (GeMiC 2018)*, Freiburg, Germany, 12th - 14th March 2018, pages 283-286. IEEE, Piscataway (NJ), 2018.
22. T. Rzesnicki, K. A. Avramidis, G. Gantenbein, S. Illy, Z. C. Ioannidis, J. Jin, I. Gr. Pagonakis, **S. Ruess**, T. Ruess, M. Schmid, M. Thumm, J. Weggen, A. Zein, and J. Jelonnek. Development and First Operation of the 170 GHz, 2 MW longer-pulse Coaxial-Cavity Modular Gyrotron Prototype at KIT. *In 43rd International Conference on Infrared, Millimeter and Terahertz Waves (IRMMW THz 2018)*, Nagoya, Japan, September, 2018.
23. T. Ruess, K. Avramidis, G. Gantenbein, Z. Ioannidis, S. Illy, J. Jin, F. C. Lutz, A. Marek, **S. Ruess**, T. Rzesnicki, M. Thumm, D. Wagner, J. Weggen, and J. Jelonnek. Automated Generation of high-order Modes for Tests of Quasi-Optical Systems of Gyrotrons for W7-X Stellarator. *In 12th German Microwave Conference (GeMiC 2019)*, Stuttgart, Germany, March, 2019.
24. T. Ruess, K. A. Avramidis, G. Gantenbein, S. Illy, F. Lutz, A. Marek, **S. Ruess**, T. Rzesnicki, M. Thumm, W. Dietmar, and J. Jelonnek. A computer-

controlled low-Power RF System to generate very High-Order Modes used in Future Fusion Gyrotrons. *In 7th International Workshop on Far-Infrared Technologies (IW-FIRT 2019)*, Fukui, Japan, March, 2019.

25. **S. Ruess**, G. Gantenbein, S. Illy, I. Gr. Pagonakis, T. Rzesnicki, M. Thumm, and J. Jelonnek. Ongoing Developments for the KIT 2-MW 170-GHz Coaxial Cavity Gyrotron. *In RF Heating Technology of Fusion Plasma (US-EU-JPN)*, Leinsweiler, Germany, September, 2016.
26. **S. Ruess**, G. Gantenbein, S. Illy, I. Gr. Pagonakis, T. Rzesnicki, M. Thumm, and J. Jelonnek. Key Components Development for the KIT 2-MW 170-GHz Coaxial-Cavity Longer-Pulse Modular Prototype Gyrotron. *In 6th International Workshop on Far-Infrared Technologies (IWFIRT 2917) and 2nd International Symposium on Development of High Power Terahertz Science and Technology (DHP-TST 2017)*, Fukui, Japan, March, 2017.
27. **S. Ruess**, G. Gantenbein, S. Illy, I. Gr. Pagonakis, T. Rzesnicki, M. Thumm, J. Weggen, and J.Jelonnek. Towards an 2 MW Long-Pulse Coaxial-Cavity Gyrotron: Progress on the Advanced KIT Inverse Magnetron Injection Gun. *In 18th International Vacuum Electronics Conference (IVEC 2017)*, London, GB, April,2017.
28. T. Rzesnicki, Z. C. Ioannidis, K. A. Avramidis, G. Gantenbein, S. Illy, J. Jin, T. Kobarg, I. G. Pagonakis, **S. Ruess**, M. Schmid, M. Thumm, J. Weggen, and J. Jelonnek. Status of Current Gyrotron Experimental Activities at KIT. *In Japan RF Heating Technology Workshop*, Shizuoka, Japan, September, 2018.
29. **S. Ruess**. An Optimized Inverse Magnetron Injection Gun for High-Power Future Fusion Gyrotrons. *In 6th KIT Fusion PhD Student Seminar*, Leinsweiler, Germany, June, 2016.
30. **S. Ruess**, X. Zeng, G. Gantenbein, S. Illy, I. Gr. Pagonakis, T. Rzesnicki, M. Thumm, and J. Jelonnek. Choice of Material Composition for a High-Performance Inverted Magnetron Injection Gun. *In 7th International Vacuum Electronics Conference (IVEC 2016)*, Monterey, CA, April, 2016.

Acknowledgment

The presented work was accomplished during my time as teaching assistant at the Institute of Radio Frequency Engineering and Electronics (IHE) and research assistant at the Institute for Pulsed Power and Microwave Technology (IHM) at the Karlsruhe Institute of Technology (KIT). First of all I want to express my deepest gratitude to Prof. Dr.-Ing. John Jelonnek for guiding my activity in the field of gyrotrons. His continuous support and precious feedback at every time led to the success. It was the unique combination of freedom and continuous support from his side which made this accomplishment possible.
Further I would like to thank Prof. Dr. Minh-Quang Tran for being my second reviewer, and the kind interest he has shown in my work. I would like to sincerely thank him for the wonderful support and the very educational discussions.
I would like to express my deep gratitude to Prof. Dr. rer. nat. Dr. h.c. Manfred Thumm for the guidance and the motivational words. It was always very pleasant and educational to work with him.
Since I had the honor to supervise the teaching at IHE/IHM, I would like to thank you for the trust you have placed in me. Be it the microwave measurement technology lectures with Dr.-Ing. Mario Pauli or the lecture high-power microwave technologies with Prof. Dr.-Ing. John Jelonnek, I always enjoyed it. It has always been a lot of fun for me to pass on the knowledge to the students.
A big thanks goes to Dr. Gerd Gantenbein, Dr. Stefan Illy, Dr. Tomasz Rzesnicki, Dr. Ioannis Gr. Pagonakis, Dr. Konstantinos Avramidis, Dr. Zisis Ioannidis and Dipl.-Ing. Martin Schmid for their great support, patience and the friendly working environment in the institute. I would also like to thank the secretariat of the institute, Mrs. Martina Huber and Mrs. Melanie Mai, for the great support and beneficial words during my time at IHM.
I would like to thank all former Ph.D colleagues at the IHM for the very good cooperation, the support and the wonderful holidays away from the everyday work environment.
Many thanks to Dipl.-Ing Jörg Weggen and Dipl.-Ing Thorsten Kobarg who designed all the components. This project would not have been possible with-

out their great ideas and perseverance. A big thank goes also to the workshop, particularly Kai Schäfer, Alexander Sivkovich, Davide Quattrocchi and Hans Brüsemeister who tirelessly and with the greatest precision manufactured the gyrotron components and were always on hand with help and advice. I would also like to thank the team in building 691, Dipl.-Ing Wolfgang Leonhardt, Daniel Mellein, Rouven Lang, Gabriel Marschall and Daniel Papenfuss for your tireless support and the fight against the escaping oil.
Furthermore, I express my appreciation to the various students whose work was performed within the frame of my thesis, starting with B.Sc. Philipp Brücker for developing the advanced minichannel cooling and spray cooling system. I am grateful to David Albert who designed all the cooling mock-ups and made them running.
I thank Dr. Zisis Ioannidis for being a very pleasant room-mate in my IHM office, and our stimulating discussions.
A big thanks goes to my parents for the loving upbringing, the great support during my studies. Thank you for the many hours on the soccer field and the thousands of kilometers you drove for me. Many thanks also to my brother for the great childhood we were allowed to spend and to the wonderful time together at IHM.
The biggest thanks go to my wife for the endless support day and night, for the always loving constructive words, and the great trust. Many thanks also to my children who show me every day what is really important in life.

Waldburg, February 2020
Sebastian Ruess